Dynamics & Charge Order

in a quarter-filled ladder system coupled to the lattice

Thomas C. Lang

Diploma thesis
to graduate with the academic title
Diplom-Ingenieur der Technischen Physik

under supervision of Ao. Univ.-Prof. Dr. Hans Gerd Evertz
Institute for Theoretical and Computational Physics
September 2005, Graz University of Technology

Abstract

We study the low energy excitations in the quarter-filled sodium vanadate ladder system α'-NaV_2O_5. With the techniques of Determinant Quantum Monte Carlo and Maximum Entropy the extended Hubbard Holstein model as an analogon for α'-NaV_2O_5 is treated in a nonperturbative and numerically exact way. We develop, to best of our knowledge, the first attempt of the implementation of the Lang-Firsov transformation in a Quantum Monte Carlo study of a spinfull many-electron Hubbard Holstein model. This basis transformation in principle enables us to sample low correlated phonon configurations. Unfortunately the extension to the many-electron model with spin degrees of freedom suffers from a severe minus-sign-problem. We are therefore forced to desist from including the coupling to the lattice. Nonetheless, we were able to compute unbiased unequal-time correlation function spectra for the extended Hubbard model. Ladder systems of the size 32×2 allow to minimize finite size effects and to obtain an improved momentum-resolution compared to exact diagonalization techniques.

Keywords: quarter-filled ladder, extended Hubbard Holstein model, Quantum Monte Carlo, Hubbard-Stratonovich transformation, α'-NaV_2O_5, Lang-Firsov transformation, Maximum Entropy, dynamic response functions

Kurzdarstellung

In dieser Arbeit studieren wir die niederenergetischen Anregungen des viertel-gefüllten Natrium-Vanadat Leitersystems α'-NaV_2O_5. Unter Anwendung der Determinanten Quanten Monte Carlo- und Maximum Entropy Methode wird das extended Hubbard Holstein Modell nicht-pertubativ und numerisch exakt behandelt. Wir entwickeln und implementieren erstmalig die Lang-Firsov Transformation für eine Quanten Monte Carlo Studie des Hubbard Holstein Vielteilchensystems mit Spinfreiheitsgraden. Mit Hilfe dieser Basis-Transformation ist es grundsätzlich möglich schwach korrelierte Phononen-Konfigurationen zu generieren. Die Erweiterung auf das Vielelektronenmodell mit Spinfreiheitsgraden unterliegt jedoch einem ausgeprägten Vorzeichenproblem und zwingt uns die Kopplung an Gitterfreiheitsgrade zu vernachlässigen. Wir berechnen die Spektren nicht-gleichzeitiger Korrelationsfunktionen für das extended Hubbard Modell für Systeme der Grösze 32×2. Verglichen zu den Möglichkeiten der Exakten Diagonalisierung weisen diese geringe Finite-Size Effekte und eine deutlich bessere Implusauflösung auf.

Schlüsselworte: viertelgefüllte Leiter, extended Hubbard Holstein Model, Quantum Monte Carlo, Hubbard-Stratonovich Transformation, α'-NaV_2O_5, Lang-Firsov Transformation, Maximum Entropy, dynamische Antwortfunktionen

Contents

1 Introduction

"Apart from the theories of superconductivity and plasma oscillations, the application of many-body theory to solids had, up to that time, led to nothing striking ...

But here we had something entirely different: the correlations might sometimes be determining the actual nature of the solid."

J. Hubbard reflecting about the work on his model
April 22, 1980, IBM Research Laboratory, San Jose, CA

Indeed, they do! Strong correlations in solids trigger phenomena from high temperature superconductivity to colossal magneto resistance. Even nowadays, decades after their experimental discovery, they puzzle theorists.

Condensed matter theory aims at the description and analysis of phenomena found in experiments. This includes the development of new efficient models, as well as methods and algorithms for analytical and numerical treatment. The combination of analytical framework and computational skills bears powerful tools for exploring physics. The goal of computing in physics is not only to benchmark analytic approaches, but also to develop an unbiased approach, capable of treating intermediate regions of parameter space.

The quantum theory for solids found its first application in the classification of crystals into metals and insulators as a function of the occupation of the electronic bands. Band theory led to a technically mature approximation, where electrons become quasiparticles which can be described under the influence of an effective potential originating from all other electrons. This effective one-particle problem results in corresponding energies taking continuous values on some distinct intervals, constituting the bands.

While electronic phenomena in crystals have been successfully described in many aspects, this approximation is no longer valid for compact electron configurations where the large Coulomb repulsion or strong attractive interactions become predominant over the

kinetic energy. De Boer and Verwey [1] reported that many properties of the transition-metal oxides are in total disagreement with these band structure calculations. Their partially occupied bands indicated a metallic behavior, but to the contrary, these materials are insulators. Mott and Peierls [2] argued that this might be the effect of the repulsive Coulomb interaction between electrons on the orbitals, which has not been taken into account in the calculations. Indeed they found that the repulsion opens a gap larger than the bare electron bandwidth. In this case the electronic band structure splits up into narrow bands, which leads to new effects giving rise to rich phase diagrams with various competing correlations.

A prominent example of such an effect, the charge order or the formation of an ordered pattern of ion charges in low dimensional quantum systems, has been known since the discovery in the Fe_3O_4 mangnetite in the early 40's [3]. Compounds with similar phenomena attract attention with the interest to find the driving force behind these transitions. They represent a challenge to theoretical physics due to the complex interplay of charge, spin, orbital and lattice degrees of freedom.

A particular interesting class of these compounds are the low dimensional vanadates, where active spins are confined to the vanadium sites. These materials are realized in a variety of different structures exhibiting many different electronic and magnetic properties. Despite their simple structure, solutions of models with realistic parameters are not yet available. Analytical methods like perturbation theory or mean field considerations provide reasonable approximations to those systems, but most of the time they cannot treat the large Coulomb repulsion effectively. Instead, numerical methods like Exact Diagonalization, Quantum Monte Carlo or Density Matrix Renormalization Group have proven to be reliable tools within condensed matter theory of strongly correlated systems.

This thesis aims at the description of the strongly correlated compound sodium vanadate and its simulation. At first we will give a brief overview of the properties and history of the strongly correlated α'-NaV_2O_5 which will be the particular topic here. The second chapter is dedicated to the model description appropriate to the compound's properties and the Lang-Firsov transformation, important for the improved numerical treatment of the model. Chapter 3 contains the numerical framework necessary for the simulation. The algorithm used as well as improved computational methods are introduced. In chapter 4 we deal with the basic theoretical elements of the operators of interest,the discussion of methods used for the analysis of the produced data and some theoretical background for their interpretation. We end with a summary and conclusion in chapter 6 followed by the appendices dealing with technical details and add-ons.

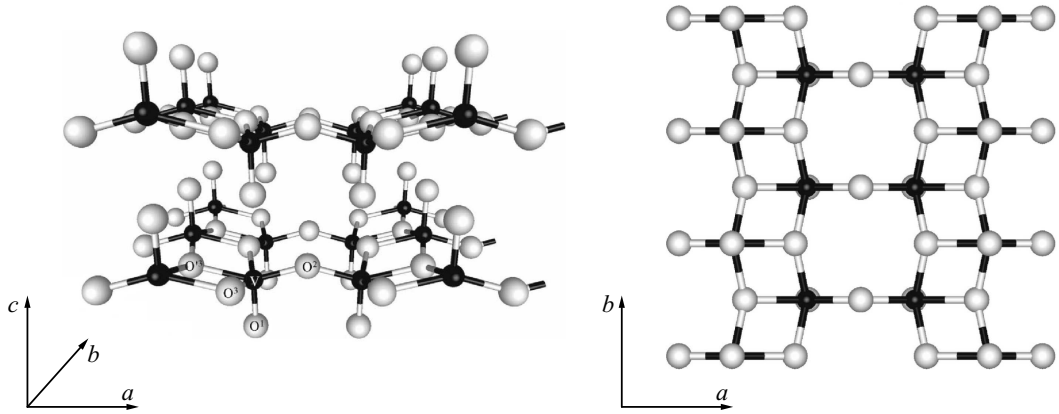

Fig. 1.1: Left: front-view of one ladder and two half ladders in two layers of α'-NaV_2O_5 built up by Vanadium atoms centered in O_5 pyramids. White balls indicate the positions of the oxygen atoms, black balls vanadium sites – the sodium doping is not indicated and would lie between the layers next to the pyramid's bottoms; right: top-view, the vanadium sites of two legs are not visible due to congruent lying oxygen atoms.

1.1 Sodium vanadate

α'-NaV_2O_5 [4] is an interesting example of a layered insulating compound. While the system can be described by an effective $S = 1/2$ anti-ferromagnetic Heisenberg-chain with coupling $J = 560$K for a wide temperature range, it undergoes a phase transition with the onset of charge order and a spin-Peierls-like spin gap formation. For this reason this compound has attracted attention since the report by Isobe and Ueda [5] in 1996. Charge order, a spin gap and therefore a drop-off of the magnetic susceptibility below 34K are the results of an interplay of on-site-, nearest-neighbor inter-site Coulomb repulsion and lattice dimerization. The system allows to investigate the homogeneous and the dimerized state of a quantum spin-ladder as a function of temperature and couplings.

Further experiments have shown that there may actually be two second order phase transitions close to each other[1]. The first one is accompanied by a logarithmic peak in the specific heat interpreted as a spin-Peierls-Ising transition causing charge ordering and super-exchange dimerization. The second one separated by ≈ 0.3K is of mean-field character and possibly a pure spin-Peierls transition triggered by increasing coupling constants due to charge ordering [6, 7, 8].

The α'-NaV_2O_5 compound is one of the five reported bronze phases of the $Na_xV_2O_5$

[1] In this context second order is used to describe a continuous transition.

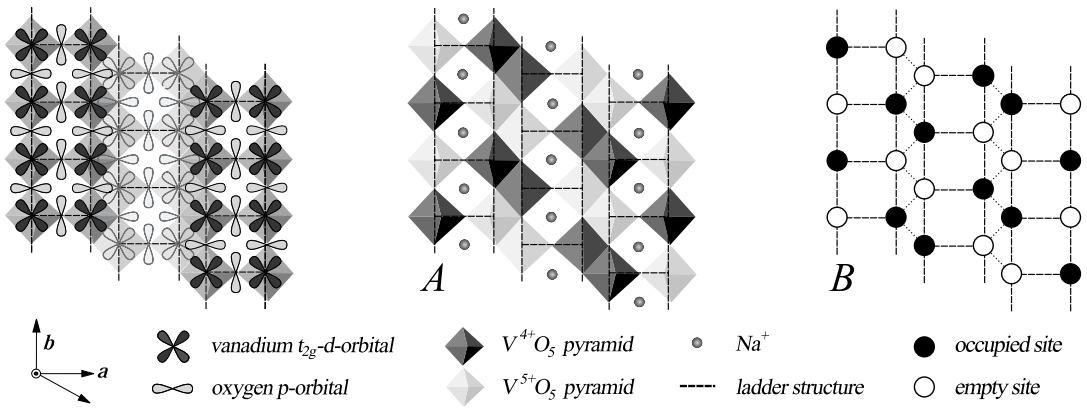

Fig. 1.2: Top view of each three ladders indicated by the dashed line Left: in-plane orbital alignment of the effective vanadium- and oxygen-sites according to [9]. Center: schematic crystal structure according to [5]. Right: site model with indicated charge order and inter-ladder coupling from [10]

system [4]. For different dopings these are $\alpha\,(0 < x \leq 0.02)$, $\beta\,(0.22 \leq x \leq 0.40)$, $\alpha'\,(0.70 \leq x \leq 1.00)$, $\eta\,(1.28 \leq x \leq 1.45)$, $\chi\,(1.68 \leq x \leq 1.82)$. Throughout this work we concentrate on the α'-phase and therefore we drop the identification of the phase. Its crystal structure consists of layers built up by VO_5 square pyramids illustrated in the model in Fig. 1.1. The crystallographic vanadium sites are located in the base-plane of the oxygen-pyramids. If the super-exchange via oxygen along the a- and b-axis are taken as the dominant exchange paths, the compound may be understood as an arrangement of weakly coupled two-leg ladders, described in more detail below.

The sodium atoms form chains lying between the VO_5 layers and act as charge reservoir. The coupling in c direction – responsible for the interaction between the layers – is very weak. Thus the properties of this compound are mainly determined by the VO_5 layers and their quasi one-dimensional ladders. Nevertheless, the coupling in c direction may be crucial for the successful description of some effects.

At room temperature first measurements indicated a non-centrosymmetric structure $Pmn2_1$[11, 12] . However, NMR-measurements [13] and X-ray diffraction, neutron scattering [14] show the centrosymmetric structure *Pmnm* with equivalent vanadium sites. This implies a formal valence of 4.5+ which comes as a surprise in view of the insulating properties. Horsch and Mack explained this behavior by showing that the molecular orbital state of one electron on a rung of two vanadium sites is the key element of the electronic structure [9]. Dagotto and others [15] explain the insulating properties via the combination with the strong local Coulomb-repulsion which confines the formal charges of the vanadium ions to 4+ and 5+. As formally only one electron (spin) per two vanadium sites is available the ladders are quarter-filled [16].

Below T_{SP} the sites become inequivalent and split into V^{4+}, V^{5+} oxidation states doubling the unit cell [17, 18]. Fig. 1.2 illustrates the VO_5 pyramids, the corresponding molecular orbits (left) and two charge order scenarios (A, B). The corresponding other two charge ordered states (A', B') are their antisymmetric counterparts. The structure of the low-temperature phase is still under discussion. The acentric $Fmm2$ point group is a proposal and is built up by alternating distorted and non-distorted charge-ordered chains. However, a corresponding $V^{4.5+}$-site is not observed in [13, 19]. Also theoretical investigations [20] propose $Fmm2$ as average space group as a result of stacking disorder. Recent experimental investigations by Ohwada and others [21] confirm this assumption. Following [20], the lattice parameters of the basic structure at 15K are $a = 11.294$Å, $b = 3.604$Å and $c = 4.755$Å. The super-lattice can be described by an F-centered orthorhombic (cubic, distorted) $2a \times 2b \times 4c$ super-cell.

A detailed representation of the structural and magnetic properties of the sodium vanadate is given by Lemmens et al [4].

1.2 General properties of ladder-systems

Inspite of their simple structure, ladder systems feature several reasons for theoretical interest. First of all, real ladder-materials do exist, mostly known in materials related to high temperature superconductors. A better understanding of the mechanisms and dynamics in ladder-materials may prove helpful for understanding the nature of high temperature superconductivity [22]. Ladder-like materials provide a good way to study the crossover from one- to two-dimensional systems, where the extensive knowledge about single chains can be of use.

The general ground state properties of spin-ladder systems can be summarized as follows. While even numbered legged ladders exhibit a spin-gap at half filling (one electron per site), the ground-state of odd numbered coupled chains is given by weakly coupled doublets forming a gapless phase [23]. For the 2-leg ladder it is assumed that its ground state is a close realization of the resonating valence bond state proposed by Anderson in the context of high-T_c superconductivity [24][2].

The qualitative behavior of two leg spin-ladders, can be understood in the rung-picture, advocated by Dagotto, Rice [23] and others. The rungs can be seen as the elements of a loose chain in the case of favored charge transfer perpendicular to the ladder. For example the behavior of the antiferromagnetic $S = 1/2$ Heisenberg ladder can be well reproduced by a antiferromagnetic $S = 1$ Heisenberg chain at some commensurate fillings.

[2] The resonating valence bond state is a linear superposition of spin singlet pairs spanning different ranges.

Spin-ladders seem to be very similar to chains in the thermo-dynamical limit at first sight and indeed, in many cases their magnetic behavior can be described by effective one-dimensional spin models. However, due to their different exchange topology, they exhibit strongly differing behavior from their one-dimensional counterparts in their electronic degrees of freedom.

These properties make ladder systems an interesting laboratory for studying the effects of various parameters in pairing-mechanisms and quantum-fluctuations.

Modeling the ladder system

2

The challenge is to design an appropriate model to simulate the physics of interest. Even though in the real compound the system is built up by a giant number of particles, models consisting of a limited number of degrees of freedom can be taken to reconstruct their distinct behavior. Despite of simplifications, most of the models cannot be evaluated analytically exactly, but preferably by perturbative approaches or numerical methods.

In this chapter we introduce the basic models, give a brief overview of their properties and the needed parameters for the model description of sodium vanadate. At the end we discuss the unitary Lang-Firsov transformation to prepare the Hamiltonian for improved numerical investigation.

2.1 Light transition-metal d-electron systems[1]

A common characteristic of many strongly-correlated compounds is the essential contribution of the transitional-metal $3d$ orbitals to the electronic properties. The physics of electronic transport and fundamental excitations takes place near the Fermi surface.

Collective modes and excitations can be only formed by unpaired electrons, thus one neglects fully occupied orbits. The bands in transition-metal compounds are mainly formed by the overlap of d-orbitals in the crystal. Because of the small radius of the wave function compared to the lattice constant this overlap is often realized via ligand oxygen p-orbitals resulting in effective transfer integrals for the electrons. The small overlap and the indirect *bridged* transfer leads to narrow bandwidths, thus rather isolated Wannier orbitals are a valid approximation. Because of the small spatial extent they retain much of their initial atomic properties such as the strong Coulomb repulsion between two electrons on the same ion. This unscreened short-ranged repulsion makes the correlations play a predominant role in the underlying physics.

[1] In this section we basically follow reference [25].

The $3d$ orbital has total angular momentum $L = 2$ and therefore fivefold degeneracy ($L_z = 2, \ldots, -2$) for each spin direction. This tenfold degeneracy is lifted through the strong influence of the crystal field leading to fourfold degenerate e_g and sixfold t_{2g} orbitals in cubic lattice structure. The latter degeneracy is lifted again through the adjacent oxygen orbitals in orthohombic crystals. Their tendency to negative valence results in larger amplitudes of the wave function away from the neighboring atoms and is represented by d_{xy}, d_{yz} and d_{zx} wave functions. The orbital structure is illustrated in Fig. 1.2.

Valence electrons in the sodium vanadate are restricted to narrow bandwidths in the twofold degenerate d_{xy} orbitals. They are therefore highly affected by local and inter-site Coulomb interactions but screened off from other influences. The p_x and p_y orbits of the closely located oxygen atoms are considered via effective exchange couplings and probably have not to be treated separately according to Horsch and Mach [9]. The system can therefore be simulated as a discrete lattice, where electrons are located on its sites.

2.2 Requirements on the model

For a given compound almost all electronic parameters such as hopping matrix elements and electron correlations but also lattice-force constants and electron-phonon couplings can be extracted from band-structure calculations.

The first-principles investigations by Spitaler et al [26] and Smolinski et al [16] underline the quasi-one-dimensional behavior of α'-NaV_2O_5: as a result of the strong anisotropy of the sodium vanadate crystal, its two-dimensional layers are approximately independent of each other. Within the plane the ladders are weakly coupled, thus we will restrict ourselves (and are still numerically restricted) to study the dynamics of a single ladder. Although the couplings in-plane and in-space are very weak, the distinct behavior of the compound may emerge from these couplings as long range order evolves in the ladders. These modes may renormalize the inter-ladder and following the inter-layer couplings in favor of an overall global behavior. Owing to the properties obtained by experiments, we expect from an appropriate model

- to involve itinerant charge carriers with spin and the coupling to phononic degrees of freedom as well as large Coulomb repulsion terms for local and nonlocal interactions in order to satisfy the d-orbital electronic properties;
- to exhibit a transition from a disordered to a charge-ordered state with decreasing temperature, or increasing coupling;

- to show an anti-ferromagnetic-Heisenberg-chain-like behavior in the high temperature regime;
- to exhibit a gap in the spin excitation spectrum in the low temperature phase;
- to be treatable in an unbiased, non-perturbative and numerically precise way with controllable errors.

As a fact of the first-principles investigations [26, 16] a Hubbard-like model including phonons should be appropriate to render the features of the α'-NaV_2O_5. The Hubbard model established itself as the most popular generic model for strong Coulomb interaction (and high temperature superconductivity). The interaction between lattice vibrations and electrons can be handled via the Holstein interaction.

2.3 Fermions on a lattice - the Hubbard model

The simplest model describing itinerant, interacting fermions with large Coulomb repulsion is the single band Hubbard model [27]. It describes unpaired electrons by the Hamiltonian in second quantization

$$H_{\mathrm{H}} = -\sum_{<ij>,\sigma} t_{ij}\left(c^{\dagger}_{i\sigma}c_{j\sigma} + c^{\dagger}_{j\sigma}c_{i\sigma}\right) + U\sum_{i} n_{i\uparrow}n_{i\downarrow}\ , \tag{2.1}$$

with $n_{i\sigma} = c^{\dagger}_{i\sigma}c_{j\sigma}$. The first term describes the kinetic contribution of the electrons which gain the energy t_{ij} (the transfer integrals) via hopping between lattice sites. The symbol $<ij>$ represents the nearest neighbor pairs and the fermionic operator $c^{\dagger}_{i\sigma}$ ($c_{i\sigma}$) creates (annihilates) an electron at site i with spin σ. The second term represents the local Coulomb interaction which contributes the amount U to the Hamiltonian in case two electrons with spins $\sigma, -\sigma$ are located at the same site i. In physical means this, e.g., gives account to the large Coulomb repulsion of two electrons in a single d-orbitals. In one dimension the model is exact solvable via the Bethe-Ansatz [28, 29] and does not show any quasi-particle excitations near the Fermi-surface. Its low energy physics is defined by collective modes namley spinons and holons (spin- and charge-fluctuations). The two- and higher dimensional Hubbard model is not (yet) exactly solved for infinite system sizes. Despite the simplicity of the Hubbard model it is not fully understood [30].

For negative values of the coupling ($U < 0$) one has the attractive Hubbard model. Physically, the local attraction can have its origin in the coupling to polarons or local phonons. For values of $U > 0$ the local interaction is repulsive. Then, as a consequence of virtual hopping of two anti-parallel spins, the model favors anti-ferromagnetic order.

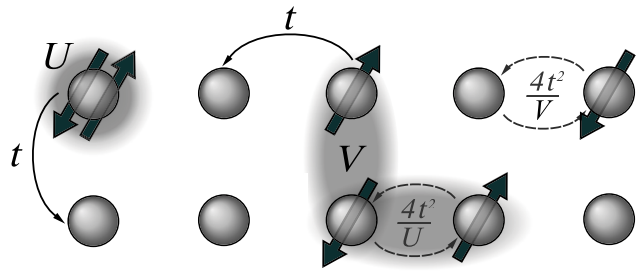

Fig. 2.1: The parameters of the (extended) Hubbard model in two dimension with the transfer integral t, on-site interaction U, inter-site coupling V and effective super-exchange coupling $J_{\mathrm{U}} = 4\,t^2/U$, $J_{\mathrm{V}} = 4\,t^2/V$ for on-site and inter-site constellations, respectively.

Although double occupation is charged with the amount U, hopping electrons contribute $-t_{ij}$ to the Hamiltonian. This so-called super-exchange can be expressed as effective coupling $J = 4\,t^2/U^2$ and is illustrated in Fig. 2.1. In the *tight-binding* (or *Fermi-gas*) *limit* $U = 0$ the Hamiltonian (2.1) describes free particles and becomes diagonal in k-space. The *atomic limit* ($t = 0$) – where no charge transfer exists – reduces the Hamiltonian to a single site problem, now diagonal in position space. The *infinite-U limit* is subject of the Nagaoka-problem, which is only exactly solvable in the cases of one dimension or a single hole in the half-filled band at arbitrary dimensions [31]. The classification of the phase-transition and phase-boundaries of the model are discussed by Watanabe and Imada [32].

Hubbard's simple model has lead to genuinely new results. But, unfortunately, it did not provide a solution to its original problem of localized versus itinerant behavior in metallic ferromagnets[3]. The Hubbard model is as fundamental to quantum systems as the Ising model to classical statistical physics. It characterizes the essentials of phenomena like filling- or bandwidth- controlled Mott-Metal-insulator transition, BCS-superconductivity, high temperature superconductivity, heavy fermions, fullerenes or liquid helium (or is assumed to do so) [30].

2.4 Extended Hubbard model

The denomination *extended* Hubbard model is used for a variety of different extensions to the pure Hubbard Hamiltonian. In our case, the latter is enhanced by an inter-site (nearest neighbor) Coulomb interaction term. Depending on the filling of the system

[2] derived from the large-U limit of the Hubbard model resulting in an effective t-J-model [31].

[3] Originally designed for the description of ferromagnetism, the Hubbard model does describe ferromagnetism, except only in some super-special cases of parameters and lattice types [30]

this repulsive interaction can be the dominating quantity. The Hamiltonian is given by

$$H_{\mathrm{EH}} = -\sum_{<ij>,\sigma} t_{ij}\left(c^{\dagger}_{i\sigma}c_{j\sigma} + c^{\dagger}_{j\sigma}c_{i\sigma}\right) + U\sum_{i} n_{i\uparrow}n_{i\downarrow} + V\sum_{<ij>} n_i n_j \ , \tag{2.2}$$

with $n_i = n_{i\uparrow} + n_{i\downarrow}$. The inter-site Coulomb repulsion term is the product of the nearest neighbor density operators n_i. The term will contribute to the Hamiltonian in case the sites i and j are each occupied by at least one electron.

1D properties

For the one-dimensional case at zero temperature and below half-filling the inter-site Coulomb repulsion leads to a quantum phase transition – a charge ordered state below a finite critical V_c. This type of extended Hubbard model exhibits phenomena like a charge- to spin-density-wave-transition (CDW, SDW) [33, 34]

Recent analyzes show that the quantum phase transition from SDW- to CDW-phase incorporates a bond-ordered (or dimerized) BOW-phase at a small intermediate region at half-filling which is possibly of Kosterlitz-Thouless type (see Fig. 2.2). Where its existence has been clarified, the form of the phase boundaries is still under discussion [35, 36, 37].

In one dimension and for $U \to \infty$ the extended Hubbard model reduces to the problem of spinless fermions with nearest-neighbor interaction, which can be solved exactly. The case of the 1D extended Hubbard model at quarter-filling ($n = 1/2$) corresponds to a half-filled band of spinless fermions with a metal-insulator transition at $V = 2t$. For $V \ll U$ and off quarter- or half-filling the system is of metallic kind. The spinful case for any filling in the limit $V \to \infty$ the model reduces to the problem free spinless fermions, since the double occupancies cannot decay. In consequence, the spin of unpaired electrons is irrelevant because they cannot be nearest neighbors. For more details and exact solutions we refer to [30].

Ladder properties

In Sec. 1.2 we stressed that for strong anisotropic hopping, ladders may be seen as chains of rungs. Though this applies to several physical quantities, the $T = 0$ phase diagrams of the one-dimensional- and the ladder-can severely differ. To illustrate the difference between the half-filled one-dimensional and the quarter-filled quasi-one-dimensional (ladder) system, their schematic ground state phase diagrams are plotted in Fig. 2.2. They exhibit definitely different behavior due to the additional spatial freedom for the electrons in the ladder. The ground state phase diagram of the quarter-filled chain instead,

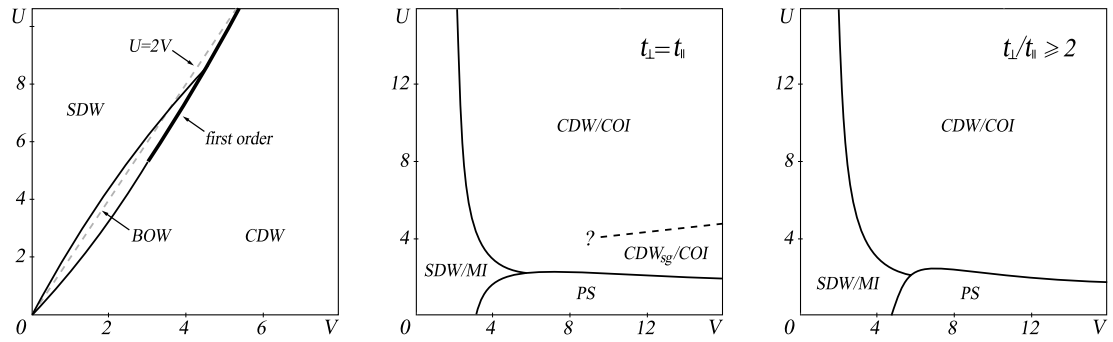

Fig. 2.2: Schematic ground state phase diagrams in the U-V-plane of the extended Hubbard model (half-filled) in one dimension (left) following Ref. [37], in the isotropic quarter-filled ladder (center), in the anisotropic quarter-filled ladder (right), according to Ref. [38]. Phases are indicated by SDW, CDW, BOW (see text), CDW_{sg} (charge density wave with spin gap; phaseboundary could not be determined with DMRG - indicated by the questionmark), PS (phase separation), MI (Mott-insulator) and COI (charge-order-insulator). The COI phase incorporates anti-ferromagnetic order of the rungs along the ladder.

looks similar to the ladders's. A BOW region at the phase boundary from Mott insulator (MI) to charge-order insulator (COI) has not been found yet.

2.5 Coupled fermion-boson system - the Holstein model

Phonons are expected to play an important role in strongly correlated electron systems like sodium vanadate [10, 39]. They affect the electronic behavior in diverse ways, such as causing shifting in temperature dependence of observables, an effective attractive electron-electron interaction, or fully changing the physics in the system, depending on the electron-phonon coupling. The Holstein model has been introduced in the late 1950s [40] in order to study electron-phonon interaction in molecular crystals. It describes the local interaction between dispersion-less optical (Einstein) phonons and the density of electrons at a given lattice site. The Hamiltonian takes the form

$$H_{\mathrm{HO}} = -\sum_{<ij>,\sigma} t_{ij}\left(c^\dagger_{i\sigma}c_{j\sigma} + c^\dagger_{j\sigma}c_{i\sigma}\right) + \sum_i \left(\frac{p_i^2}{2\,M} + \frac{k}{2}\,x_i^2\right) - \alpha' \sum_i n_i x_i \;, \tag{2.3}$$

where k denotes the spring-constant and M, p_i and x_i denote the mass of the vibrating ions, their momenta and their coordinates, respectively. The phonon degrees of freedom are equivalent to local harmonic oscillators coupled to the electron density at each site

with coupling strength α'. The Hamiltonian in second quantization reads

$$H_{\mathrm{HO}} = -\sum_{<ij>,\sigma} t_{ij}\left(c_{i\sigma}^{\dagger}c_{j\sigma} + c_{j\sigma}^{\dagger}c_{i\sigma}\right) + \omega_0 \sum_i a_i^{\dagger}a_i - g\sum_i n_i\left(a_i^{\dagger} + a_i\right) \ . \tag{2.4}$$

Here $c_{i\sigma}^{\dagger}$ ($a_i^{\dagger}$) denote fermionic (bosonic) creation operators of spin-σ electrons (phonons) and i is the Wannier site index again. The free phonon energy is given by the angular frequency $\omega_0 = \sqrt{k/m}$ ($\hbar = 1$) and the electron-phonon coupling g is defined related to α' via $g = \alpha'/\sqrt{2\,M\omega_0}$. The phonon operators in second quantization are related to their counterparts in first quantization via

$$a_i = \sqrt{\frac{M\omega_0}{2}}\,x_i + \mathrm{i}\sqrt{\frac{1}{2\,M\omega_0}}\,p_i \quad , \quad a_i^{\dagger} = \sqrt{\frac{M\omega_0}{2}}\,x_i - \mathrm{i}\sqrt{\frac{1}{2\,M\omega_0}}\,p_i \tag{2.5}$$

and, equivalently,

$$x_i = \sqrt{\frac{1}{2\,M\omega_0}}\,(a_i^{\dagger} + a_i) \quad , \quad p_i = \mathrm{i}\sqrt{\frac{M\omega_0}{2}}\,(a_i^{\dagger} - a_i)\ . \tag{2.6}$$

A common definition is the dimensionless parameter λ related to the electron-phonon coupling g via $\lambda = 2g^2/\omega_0 W$, where W is the free electron bandwidth. For small coupling λ and small frequencies ω the model is treatable via weak-coupling perturbation theory – the opposite with large λ, ω via perturbation theory with the help of the Lang-Firsov transformation (see Sec. 2.9). For the intermediate regime only numerical techniques are applicable, e.g., exact diagonalization, or Quantum Monte Carlo are applicable [41, 42, 43].

Einstein phonons are justifiable for models of realistic compounds in case the compound's phonon modes show only vanishing dispersion. An analytical description of the model is given by the Migdal-Eliashberg theory, however, it suffers from quantitative deviations because of missing interaction terms (vertex corrections) and does not fit to one-dimensional systems, where the phonon energies become of the order of the free electron bandwidth.

Polarons

Coupling electrons to phonons can lead to the formation of quasi-particles (termed polarons after Landau in 1933) in form of charge carriers *dressed* with a cloud of approximately localized coherent phonons. Depending on the coupling to the electrons λ and the retarded action, these quasi-particles can be blurred over several sites or localized at a single site. For small λ the electrons are dressed in a coherent multi-phonon-cloud simply causing a shift in potential energy. With increasing coupling they mediate an

effective attractive potential by renormalizing the transfer integral t_{ij} in the hopping term. As the coupling changes the system behavior, the ratio to the phonon frequency becomes crucial. At coupling $\lambda < 1$ and the ratio $\lambda/\omega_0 < 1/2$ quasi-particle (Bloch-like states) form and the phonon cloud surrounding the electron gives rise to an increased effective mass of the particle, limiting its bandwidth. On the other hand, for $\lambda > 1$ and $\lambda/\omega_0 > 1/2$, the electrons become trapped in their self-induced lattice distortion, usually called small polaron. In general, polaronic effects become more dominant for small phonon frequencies $\omega_0 \to 0$ [43].

2.6 Extended Hubbard Holstein model

Combination of the extended Hubbard model and the Holstein model results in the extended Hubbard Holstein model (EHHM), which is the model we use for our investigations. The Hamiltonian is given by

$$\begin{aligned} H_{\mathrm{EHH}} &= -\sum_{<ij>,\sigma} t_{ij}\left(c^{\dagger}_{i\sigma}c_{j\sigma} + c^{\dagger}_{j\sigma}c_{i\sigma}\right) + U\sum_{i} n_{i\uparrow}n_{i\downarrow} + V\sum_{<ij>} n_i n_j \\ &\quad + \omega_0\sum_{i} a^{\dagger}_i a_i - g\sum_{i} n_i\left(a^{\dagger}_i + a_i\right) \ . \end{aligned} \tag{2.7}$$

As for the Holstein model, in certain parameter regimes, it is energetically favorable for a second electron to remain close to a first electron rather than to distort another portion of the lattice structure. Thus the phonons induce an effective attraction between electrons. Typical energy-scales of electrons ($\mathcal{O}$(1eV)) and phonons ($\mathcal{O}$(10meV)) put close the assumption that the phonons affect the system only in form of small fluctuations. Indeed, as a consequence of the strong correlations, the bandwidths are renormalized to a regime where the influence of the phonons becomes non-negligible.

Fully quantum mechanical treatment of lattice fluctuations in systems with finite electron density has so far received little attention. The reason for this is that such calculations face severe difficulties handling electron-phonon coupling together with strong electron-electron repulsion and their parameter range is heavily restricted. Perturbative studies are restricted to weak, strong, or adiabatic coupling limits and numerical treatment is very delicate. Where Quantum Monte Carlo (QMC) is handicapped by long autocorrelation times, exact diagonalization techniques (e.g., ED, DMRG) are limited within a certain number of degrees of freedom (details will be given in the following chapter).

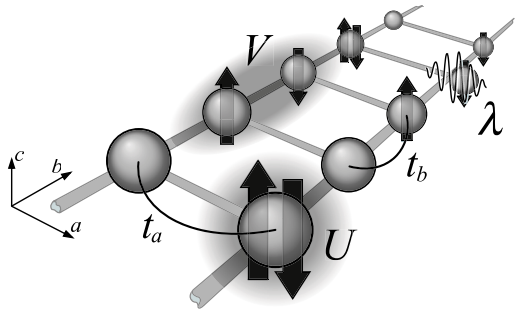

Fig. 2.3: The generic ladder-model with indicated transfer integrals along and perpendicular to the ladder t_a, t_b, on-site and inter-site Coulomb couplings U, V, respectively, and electron-phonon coupling λ.

Polarons and Bipolarons

Depending on the relative strength of the phonon-mediated attraction and the Coulomb repulsion, pairs of electrons may form bonding states called bipolaron. This quasi-particle may consist of two electrons in either a singlet or a triplet state depending on their individual spin alignment. While the singlet consists of two electrons of opposite spin on one site, the triplet lies energetically above the singlet and is usually spread over at least two sites due to the Pauli-exclusion principle.

For small electron-phonon couplings λ (see Sec. 2.5) and large U neither the Hubbard-Holstein model (HHM) with $V = 0$ nor the EHHM is expected to form bound bipolarons. In contrast to the HHM, where the attractive interaction mediated by phonons favors bound singlet bipolarons with increasing λ, in the EHHM the inter-site Coulomb repulsion competes with the attractive potential. This leads first to bounded singlet bipolarons and for strong coupling to a state of coexisting bounded singlet- and bounded triplet bipolarons. The renormalized masses of the polarons and bipolarons become smaller with increasing on-site-repulsion U, which probably makes them more mobile. The HHM shows a transition from a bipolaron state to an unbound polaron formation at a critical value of U. In contrast, the polarons in the EHHM remain bounded even in the limit $U \to \infty$.

Since we will not primarily focus on the polaron and bipolaron formation in the EHHM within this work, we refer the interested reader to the references [43, 44, 45, 46, 47].

2.7 Symmetries of Hubbard models in low dimensions

The application of the theory of groups and their representations for the exploitation of symmetries in quantum mechanics allows consideration of model properties and their behavior in case of symmetry breaking. Their knowledge also allows improved numerical treatment, especially important in exact diagonalization techniques to efficiently minimize the number of states needed to be saved, or the sampling in Monte Carlo simulations. The group transformations are mathematically represented in the state space by operations relating the states to each other. The quantum mechanical analogues are operators acting on the state space, which correspond to the physical observables. Any state of a physical system can be described as a superposition of states of elementary systems and that is, of systems with states which transform according to the *irreducible* representations of the symmetry group. The interpretation of symmetry breaking and its transition allows the classification of models and their critical exponents.

The one-dimensional Hubbard model has infinitely many conserved quantities and is integrable. The non-integrable higher dimensional Hubbard models have only a few known symmetries. On regular (bipartite) lattices with periodic boundary conditions, the general class of Hubbard Hamiltonians has some or all of the following symmetries and invariances:

- $SU(2)$ spin rotational invariance at half-filling – conservation of total spin under global spin-rotations (the generators of the $SU(2)$-algebra).
- $SU(2)$ charge rotational invariance – charge conservation (in the case of symmetric, non-frustrated hopping).
- $U(1)$ phase symmetry – evidently in every particle quantum system (at commensurable filling) an arbitrary phase factor of the wave function leaves observables invariant. In the $U(1)$-broken state the group reduces to a $SU(2)$ s-charge density wave (known in the context of superconductivity).
- Particle-hole symmetry – the transformation of electrons into holes and vice-versa (at half-filling).
- Parity – *site-parity* invariance under spatial reflections (in even numbered systems); *spin-parity/chirality* invariance under chiral-transformations.
- Free choice of sign of the transfer amplitude t under the transformation $c_{i\sigma}^{(\dagger)} \rightarrow (-1)^i\, c_{i\sigma}^{(\dagger)}$ – so that $H(t, U, ...) = H(-t, U, ...)$.
- Translational symmetry – The total momentum on the lattice is conserved.
- Particle number conservation.
- Point symmetry group of the finite lattice – invariance under certain transformations. The corresponding conserved currents are parity and the quantum number of

the discrete lattice rotations, which can be considered as a discrete spatial angular momentum.

The overall symmetry of the Hubbard model at half-filling is given by

$$SO(4) = SU(2) \times SU(2)/Z_2 \ , \tag{2.8}$$

where the reduction through Z_2 is due to the simultaneously integer or half odd-integer eigenvalues of the z-components of total spin and charge. Several more special cases and overviews are given in references [30, 31, 48]. The symmetries of the extended Hubbard Holstein model are discussed in Ref. [49].

There exist some (albeit only a few) rigorous theorems for Hubbard models [50, 51]. The absence of magnetic ordering in one and two dimensions was proven by Ghosh [52], who extended the Bogoliubov inequality method of Mermin and Wagner [53]. This assertion is valid for a general class of Hubbard models and forbids the spontaneously breaking of a continuous symmetry in one or two dimensions at finite temperature (a thermodynamic phase transition). The theorem of Lieb [54] states for the Hubbard model that for finite systems at even filling the system has $S_z = 0$ for total spin and the ground-state is definite (at half-filling) or trivially degenerated in $SU(2)$ symmetry. Another rigorous theorem by Koma and Tasaki [55, 56] yields explicit bounds for the decay of the superconducting and magnetic correlations in one- and two-dimensional Hubbard models, valid for also for non-local interactions. We will return to these symmetry considerations when we interpret and justify the simulation results in Sec. 4.5.

2.8 Model parameters for α'-NaV_2O_5

We have now chosen an appropriate model reflecting the properties of the α'-NaV_2O_5. We need to know now the strength of the Coulomb-couplings, transfer integrals, lattice force constants and dominant phonon frequencies. With the knowledge of the structure (spatial alignment and electronic configuration) almost all these parameters (shown in Fig. 2.3) can be extracted from first-principles band-structure calculations.

We choose the intra-rung transfer integral t_a as the system unit of energy which has been estimated by the LDA calculations done in [16, 26] to be $t_a \approx 0.35\text{eV}$. The transfer integral along the ladder is $t_b \simeq t_a/2$, which favors intra-rung hopping and the quasi-one-dimensional magnetic behavior. For the strong on-site Coulomb repulsion we use $U = 8.0t_a$ as estimated in [16]. We assume an isotropic extended Hubbard Coulomb repulsion which will be left as free parameter. It will be determined within the simulation so that it causes full (in the sense of quantum mechanics) charge order. The electron-phonon coupling can be obtained by comparing the cases of the undistorted and distorted

lattice and is estimated as $\lambda = 0.49t_a$ [26]. Phonon frequencies of dynamical lattice distortions are given by experiment [57], with the smallest dominant frequencies at $\omega_0 = 60\text{meV}, 125\text{meV}$, or $\omega_0 = 0.17t_a, 0.36t_a$ while their eigenvectors are given by first-principles calculations [16, 26]. Now, that we have defined the parameters in terms of t_a, we will no longer exhibit the energy unit in the following definitions explicitly.

We will see in the following that the opening of a spin gap cannot be reconstructed by the model for this distinct set of parameters, but may be a result of lattice vibrations. A Density Matrix Renormalization study by Vojta and others shows a spin gap in the EHM for increasing hopping anisotropy [38]. Another possible idea is that the gap in the magnon spectrum emerges due to a collective mode of a cluster of ladders[58].

2.9 The Lang[4]-Firsov transformation

Unfortunately, sampling phonon configurations by local updating of the phonon coordinates or momenta leads to tremendous autocorrelation times independent of the electronic structure. They grow quadratically with decreasing phonon frequency and temperature. They become problematic at phonon frequencies $\omega_0 < 1$ or strong electron-phonon coupling $\lambda > 1$ – the parameters for which polaron effects are large and the physics is most interesting. These problems can be overcome by applying the Lang-Firsov (LF) transformation [41] to the Hamiltonian. This unitary transformation separates the displacement of the local oscillators from the free oscillator dynamics around the equilibrium positions. The updating process of the phonons involves for less electronic contributions and therefore becomes almost independent of the electron-phonon coupling λ. The transformation does not involve any free parameters and is exact.

This work is, to the best of our knowledge, the first use of the LF-transformation with a QMC-study of a spinful many-electron Hubbard Holstein model. So far, the approach has been used in several ED-studies [59, 60, 61] and Hohenadler and others have intensively investigated the polaron formation in the Holstein model with spinless electrons [62, 43] and the Hubbard Holstein model with two spinful electrons [63, 64, 43]. Perturbative approaches based on the LF-transformation yield reasonable results for strong electron-phonon coupling and intermediate or large phonon frequencies $\omega \geq 1$, but cannot be extended to the regime of intermediate coupling and small finite phonon frequencies.

In this section we basically follow Ref. [43]. It is more convenient to express the phonon variables in Eq. (2.3) in terms of their natural units $x_i \mapsto (M\omega_0)^{-1/2}\, x_i$, $p_i \mapsto (M\omega_0)^{1/2}\, p_i$. Setting $M = 1$, $k = \omega_0^2$ and defining $\alpha = \alpha'/\sqrt{2} = \sqrt{2}g$, the Hamilto-

[4] Unfortunately, NO this is not me!

nian equivalent to Eq. (2.7) in grand-canonical representation becomes

$$\begin{aligned} H^{\mu}_{\mathrm{EHH}} &= -\sum_{<ij>,\sigma} t_{ij}\left(c^{\dagger}_{i\sigma}c_{j\sigma}+c^{\dagger}_{j\sigma}c_{i\sigma}\right)+U\sum_{i} n_{i\uparrow}n_{i\downarrow}+V\sum_{<ij>} n_i n_j \\ &\quad +\frac{\omega_0}{2}\sum_{i}\left(p_i^2+x_i^2\right)-\alpha\sum_{i} n_i x_i-\mu_0\sum_{i} n_i \,, \end{aligned} \tag{2.9}$$

where we introduced the chemical potential μ_0. The unitary operator of the LF-transformation is defined as

$$\mathrm{e}^{S}=\mathrm{e}^{i\gamma\sum_i n_i p_i} \,, \qquad \text{with} \qquad S^{\dagger}=-S \,, \tag{2.10}$$

where n_i is the electron density operator and the operator p_i corresponds to the phonon momentum at site i. The parameter γ depends on the coupling constant and will be defined in the following. The operator e^{S} satisfies anti-hermiticity so that operators transform as

$$A \mapsto \tilde{A}=\mathrm{e}^{S}A\,\mathrm{e}^{-S} \,. \tag{2.11}$$

Via the Campbell-Baker-Hausdorff relation for bosonic operators

$$\tilde{A}=\mathrm{e}^{S}A\,\mathrm{e}^{-S}=A+[S,A]+\frac{1}{2!}[S,[S,A]]+\dots \,, \tag{2.12}$$

we obtain the annihilation (creation) operator commutator relations

$$[S,c^{\dagger}_{i\sigma}]=i\,\gamma\,p_i\,c^{\dagger}_{i\sigma} \,, \qquad [S,c_{i\sigma}]=-i\,\gamma\,p_i\,c_{i\sigma} \,. \tag{2.13}$$

This yields

$$\tilde{c}^{\dagger}_{i\sigma}=c^{\dagger}_{i\sigma}\,\mathrm{e}^{\mathrm{i}\gamma p_i} \,, \qquad \tilde{c}_{i\sigma}=c_{i\sigma}\,\mathrm{e}^{-\mathrm{i}\gamma p_i} \,. \tag{2.14}$$

The transformations for the displacement and the moment of the oscillator at site i are

$$\tilde{x}_i=x_i+\gamma\,n_i \,, \qquad \tilde{p}_i=p_i \,. \tag{2.15}$$

With Eq. (2.14) and Eq. (2.15) we can derive the extended Hubbard Holstein Hamiltonian (Eq. (2.7)) under Lang-Firsov transformation

$$\begin{aligned} \tilde{H}^{\mu}_{\mathrm{EHH}} &= \mathrm{e}^{S}H^{\mu}_{\mathrm{EHH}}\,\mathrm{e}^{-S} \\ &= \mathrm{e}^{S}\left(H_{\mathrm{k}}+H_{\mathrm{U}}+H_{\mathrm{V}}+H_{\mathrm{osc}}+H_{\text{e-ph}}+H_{\mu}\right)\mathrm{e}^{-S} \,. \end{aligned} \tag{2.16}$$

Since the density operators are not affected by the transformation, only the terms $H_{\mathrm{K}}, H_{\mathrm{osc}}$ and $H_{\text{e-ph}}$ change

$$\tilde{H}_{\mathrm{k}} = -\sum_{<ij>,\sigma} t_{ij}\,\mathrm{e}^{i\gamma(p_i-p_j)}\left(c^{\dagger}_{i\sigma}c_{j\sigma}+c^{\dagger}_{j\sigma}c_{i\sigma}\right) \tag{2.17}$$

$$\tilde{H}_{\mathrm{osc}}+\tilde{H}_{\text{e-ph}} = \frac{\omega_0}{2}\sum_{i}\left(p_i^2+(x_i+n_i\gamma)^2\right)-\alpha\sum_{i} n_i(x_i+n_i\gamma) \,. \tag{2.18}$$

By choosing the free parameter

$$\gamma = \frac{\alpha}{\omega_0} \,, \tag{2.19}$$

the coupling term in Eq. (2.18) vanishes. The equation then simplifies to

$$\tilde{H}_{\text{osc}} + \tilde{H}_{\text{e-ph}} = \frac{\omega_0}{2} \sum_i \left(p_i^2 + x_i^2\right) - E_{\text{P}} \sum_i n_i^2 \,. \tag{2.20}$$

The first term matches with the untransformed oscillator-term. The term quadratic in the density operators contains the factor $E_{\text{P}} = \omega_0 \gamma^2/2$. It emerges as a natural parameter from the Lang-Firsov transformation and is commonly termed polaron binding energy. We again use the dimensionless quantity

$$\lambda = \frac{\alpha^2}{\omega_0 W} = \frac{\alpha'^2}{\omega_0^2 W} = \frac{2\,g^2}{\omega_0 W} \,, \tag{2.21}$$

as the electron-phonon coupling constant normalized to the free electron bandwidth $W = 4tD$ in D dimensions. This enables one to compare electron-phonon coupling strengths of systems of different dimension independent of the phonon frequency ω_0. This way we could also have written $\gamma = \sqrt{\lambda W/\omega_0}$ in Eq. (2.19) or for the polaron binding energy $E_{\text{P}} = \lambda W/2$. The quadratic term in Eq. (2.20) can now be written as

$$\begin{aligned} -E_{\text{P}} \sum_i n_i^2 &= -E_{\text{P}} \sum_i \left(n_{i\uparrow} + n_{i\downarrow}\right)^2 \\ &= \underbrace{-E_{\text{P}} \sum_i n_i}_{\to H_\mu} \underbrace{-2\,E_{\text{P}} \sum_i n_{i\uparrow} n_{i\downarrow}}_{\to H_{\text{U}}} \,, \end{aligned} \tag{2.22}$$

leading to additional contributions to the chemical potential and the on-site Hubbard term. The transformed Hamiltonian at last yields

$$\tilde{H}^{\mu}_{\text{EHH}} = \tilde{H}_{\text{k}} + H_{\text{osc}} + \tilde{H}_{\text{U}} + H_{\text{V}} + \tilde{H}_{\mu} \,, \tag{2.23}$$

with the terms

$$\tilde{H}_{\text{k}} = -\sum_{<ij>,\sigma} t_{ij}\, \mathrm{e}^{i\gamma(p_i - p_j)} \left(c^{\dagger}_{i\sigma} c_{j\sigma} + c^{\dagger}_{j\sigma} c_{i\sigma}\right) \,, \tag{2.24}$$

$$H_{\text{osc}} = \frac{\omega_0}{2} \sum_i \left(p_i^2 + x_i^2\right) \,, \tag{2.25}$$

$$\tilde{H}_{\text{U}} = \tilde{U} \sum_i n_{i\uparrow} n_{i\downarrow} \,, \tag{2.26}$$

$$H_{\text{V}} = V \sum_{<ij>} n_i n_j \,, \tag{2.27}$$

$$\tilde{H}_{\mu} = -\tilde{\mu} \sum_i n_i \,, \tag{2.28}$$

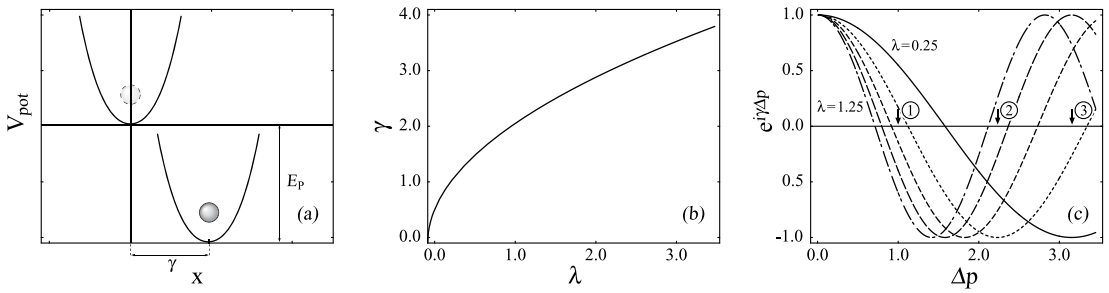

Fig. 2.4: (a) schematic illustration of the shifting of the oscillator potential in the presence of an electron in the LF-transformed model. (b) the factor γ as a function of the electron-phonon coupling λ; (c) the real part of the complex phase $e^{i\gamma(p_i-p_j)}$ as a function of the momenta difference $\Delta p = p_i - p_j$ for couplings of $\lambda = 0.25, 0.5, \ldots, 1.25$ – see Sec. 3.6.2 for discussion; both figures at bandwidth $W = 4\,tD = 4.0$ and $\omega_0 = 1.0$.

and the effective couplings with the contributions from Eq. (2.22)

$$\tilde{U} = U - 2\,E_\mathrm{P} \qquad \text{and} \qquad \tilde{\mu} = \mu_0 + E_\mathrm{P}\ . \tag{2.29}$$

For the case of $U < 2\,E_\mathrm{P}$ this introduces an attractive interaction between electrons on a site. In a physical view the redefinition of U to $\tilde{U}$ reflects the situation at large phonon coupling where it is energetically favorable to pay the energy U instead of destroying the current phononic configuration by electron transfer. Additionally the extension of the hopping term in Eq. (2.17) by the complex phase factor $e^{i\gamma(p_i-p_j)}$ reflects this behavior.

In Fig. 2.4a the shift of the oscillator potential in the presence of an electron is illustrated. When the lattice is displaced by γ, the harmonic potential of the oscillator is lowered by the amount of the polaron binding energy E_P, $4\,E_\mathrm{P}$ in the case of one, two electrons on the same site, respectively. The phase depends on the phonon coupling λ and goes with the square-root $\gamma = \sqrt{\lambda W/\omega_0}$. The hopping is damped or even penalized for increasing momenta-differences as visible in Fig. 2.4b,c.

As shown, the Lang-Firsov transformation removes the electron-phonon coupling term, introduces a Hubbard-like attractive interaction and extends the transfer integral by a complex phase.

3 Numerical method

Numerical methods can no longer be regarded as mere tools to check analytical results, but represent an alternative way to physics. Simulation techniques are still under development – in many cases new techniques are as much a demonstration of an algorithm as they are an exploration of new physics. Difficulties in performing simulations include excessive computation time, non-positive definite probability weights that become negative, non-ergodic behavior and numerical instabilities.

We are dealing with high dimensional integrals and quantum mechanics. The interest is focused on large system sizes, a wide range of parameters (V, λ, ω_0, T) and most of all on the dynamical properties of the system. A suitable technique for evaluating the model is the Quantum Monte Carlo method (QMC) in equilibrium. The QMC is an approximation-free method which gives exact results up to statistical errors and can be applied to large system sizes[1]. Further processing of QMC data via the Maximum Entropy method allows one to obtain dynamical properties of the model as a function of real frequency.

In this chapter the principles of QMC applied onto the grand-canonical ensemble with its benefits and problems will be introduced. Numerical stabilizing techniques as well as analytic optimization are discussed.

3.1 Quantum Monte Carlo

Classical Monte Carlo (MC) is based on sampling configurations of the partition function according to a probability weight. This is done by constructing a Markov sequence of configurations by changing an existing configuration corresponding to the weighting decision introduced by Metropolis and others with respect to the detailed balance condition

[1] Note, precision and discretization errors of some QMC methods can be arbitrarily reduced limited only by computation time.

[65]. This corresponds to replacing the deterministic integral problem by an equivalent stochastic one. As an example, we want to evaluate the expectation value of a function $f(x)$ under a proper weight function $w(x) \geq 0$, where

$$\langle f \rangle_w = \frac{\int dx\, w(x)\, f(x)}{\int dx\, w(x)} \,. \tag{3.1}$$

We may obtain this by a summation over a set of points $\{x_i\}$

$$\langle f \rangle_w = \lim_{N\to\infty} \frac{1}{N} \sum_{\{x_i\}} f(x_i) \,, \tag{3.2}$$

where the points $\{x_i\}$ are distributed according to w. Thus we are exploiting the central limit theorem by sampling an average to average a sample. Proposing the set of points as a Markov chain under the condition that the probability to get from point x to x' is symmetric (the detailed balance condition), i.e.,

$$w(x)\, P(x \to x') = w(x')\, P(x' \to x) \,, \tag{3.3}$$

guarantees w to be the equilibrium distribution of this Markov process. If $w(x)$ corresponds to the Boltzmann weight $\exp(-\beta E(x))$ one can accept a new point (configuration), satisfying Eq. (3.3), with the Metropolis probability

$$P(x \to x') = \min(1, \exp(-\beta[E(x') - E(x)]) \,. \tag{3.4}$$

Its main advantage is, that it allows to evaluate phase space integrals (such as thermal averages) in a time that scales only polynomially with the system size N, although the configuration space expands exponentially with N [66]. Here, only a brief overview to the usage of the MC-method is shown – for a comprehensive overview we refer the reader to the book by Landau and Binder [67].

The statistical mechanics of a *quantum system* can be described by a path integral formalism [68]. In the path integral representation, every quantum particle maps onto a cyclic string. In most path integral simulations like in QMC, the quantum strings are first discretized and then the sum over all paths is carried out by MC integration. In general, the d dimensional quantum system is mapped onto a $d+1$ dimensional classical system. Introductions to various QMC methods are given by von der Linden [69] and Evertz [70].

In the present paper the Determinant Quantum Monte Carlo (DetQMC) method introduced by Blankenbecler, Scalapino and Sugar (BSS) in 1981 is used for the evaluation of the extended Hubbard Holstein model [71, 72, 73]. Part I of the introductory paper to the BSS-formalism has been published in [74] dealing with field operators and

gauge fields on the space-time-lattice, where part II published in [75] deals with fermion operators on sites and bonds. This reflects the similar techniques used in high energy physics and condensed matter physics. The BSS-style-simulation can also be interpreted as a coupled fermion-boson system with nonlinear four-fermion interaction and found its application in the context of the Nambu Jona-Lasinio [76] or Gross-Neveu model (also thought of as a possible model for high-T_c superconductors [77]).

3.2 Basics and Trotter-decomposition

The objective is to calculate quantum mechanical expectation values of the form

$$\langle A \rangle = \frac{1}{\mathcal{Z}} \mathrm{tr} \left(A \, \mathrm{e}^{-\beta H} \right) = \frac{1}{\mathcal{Z}} \int \mathcal{D}\Psi \, \mathrm{e}^{-\beta H} \, A(\Psi) \, , \tag{3.5}$$

where the partition function $\mathcal{Z}$ is given by

$$\mathcal{Z} = \mathrm{tr} \left\{ \mathrm{e}^{-\beta H} \right\} = \int \mathcal{D}\Psi \, \left\langle \Psi \middle| \mathrm{e}^{-\beta H} \middle| \Psi \right\rangle \, , \quad \text{or} \quad \mathcal{Z} = \sum_{|\Psi\rangle} \left\langle \Psi \middle| \mathrm{e}^{-\beta H} \middle| \Psi \right\rangle \, , \tag{3.6}$$

where $\beta = 1/k_{\mathrm{B}}T$ is the inverse temperature and k_{B} denotes Boltzmann's constant. Identifying the inverse temperature as imaginary (Euclidean) time $\beta = \mathrm{i}\, t/\hbar$, we can write the equations in Feynman's path integral representation

$$\langle A \rangle = \frac{1}{\mathcal{Z}} \int \mathcal{D}\Psi \, \mathrm{e}^{-S(\Psi)} \, A(\Psi) \, , \quad \text{with} \quad \mathcal{Z} = \int \mathcal{D}\Psi \, \mathrm{e}^{-S(\Psi)} \, , \tag{3.7}$$

where $S(\Psi)$ denotes the Euclidean action for all possible configurations of the classical fields Ψ. Within quantum simulations one generally studies the operator $\mathrm{e}^{-\beta H}$ by writing each matrix element as a path integral

$$\begin{aligned} \left\langle \Psi_S \middle| \mathrm{e}^{-\beta H} \middle| \Psi_E \right\rangle = \sum_{|\Psi_1\rangle \ldots |\Psi_{L-1}\rangle} & \left\langle \Psi_S \middle| \mathrm{e}^{-\Delta\tau H} \middle| \Psi_1 \right\rangle \left\langle \Psi_1 \middle| \mathrm{e}^{-\Delta\tau H} \middle| \Psi_2 \right\rangle \ldots \\ & \times \left\langle \Psi_{L-1} \middle| \mathrm{e}^{-\Delta\tau H} \middle| \Psi_E \right\rangle \, , \end{aligned} \tag{3.8}$$

where the path integral has been discretized in steps $\Delta\tau = \beta/L$ and $\mathrm{e}^{-\beta H} = \mathrm{e}^{-\mathrm{i}\, t\, H/\hbar}$ is the time evolution operator of the system. The integral is over all paths periodic in imaginary time, with $\left|\Psi\right\rangle = \left|\Psi_S\right\rangle = \left|\Psi_E\right\rangle$. The kinetic and potential terms in the Hubbard Hamiltonian do not commute and therefore cannot be simultaneously diagonalized. However, we may break-up the Hamiltonian to separate the exponentials – diagonalization of the single terms is more easily. In the following we will restrict the treatment

for simplicity to the extended Hubbard Hamiltonian without phonons which has already been introduced in Eq. (2.2). The Hamiltonian in grand canonical representation consists of the parts

$$\begin{aligned} H^{\mu}_{\mathrm{EH}} &= -\sum_{<ij>,\sigma} t_{ij}\left(c^{\dagger}_{i\sigma}c_{j\sigma} + c^{\dagger}_{j\sigma}c_{i\sigma}\right) + U\sum_{i} n_{i\uparrow}n_{i\downarrow} + V\sum_{<ij>} n_i n_j - \mu_0 \sum_i n_i \\ H^{\mu}_{\mathrm{EH}} &= H_{\mathrm{k}} + H_{\mathrm{U}} + H_{\mathrm{V}} + H_{\mu}\,. \end{aligned} \tag{3.9}$$

According to the Suzuki-Trotter decomposition [78, 79, 80] the sum of matrices in an exponent can be written as

$$\mathrm{e}^{(A+B)} = \lim_{L\to\infty}\left(\mathrm{e}^{\frac{A}{L}}\,\mathrm{e}^{\frac{B}{L}}\right)^{L}\,, \tag{3.10}$$

where the breakup parameter L discretizes the imaginary-time or Trotter-time into slices of length $\Delta\tau$, which corresponds to the path integral. We apply this decomposition to the Hubbard Hamiltonian where the discretization leads to a controlled systematic error for a finite L,

$$\begin{aligned} \mathrm{e}^{-\beta H^{\mu}_{\mathrm{EH}}} &= \mathrm{e}^{-\beta\,(H_{\mathrm{k}}+H_{\mathrm{U}}+H_{\mathrm{V}}+H_{\mu})} \\ &= \lim_{L\to\infty}(\mathrm{e}^{-\frac{\beta}{L}H_{\mathrm{k}}}\,\mathrm{e}^{-\frac{\beta}{L}H_{\mathrm{U}}}\,\mathrm{e}^{-\frac{\beta}{L}H_{\mathrm{V}}}\,\mathrm{e}^{-\frac{\beta}{L}H_{\mu}})^{L} \\ &= \prod_{i=1}^{L}\Big(\mathrm{e}^{-\Delta\tau H_{\mathrm{k}}}\,\mathrm{e}^{-\Delta\tau H_{\mathrm{U}}}\,\mathrm{e}^{-\Delta\tau H_{\mathrm{V}}} \\ &\qquad + \frac{1}{2}\,\beta\Delta\tau[[[H_{\mathrm{k}},H_{\mathrm{U}}],H_{\mathrm{V}}],H_{\mu}] + \beta\,\mathcal{O}((\Delta\tau)^2 tUV)\Big)\,. \end{aligned} \tag{3.11}$$

Within the trace, e.g Eq. (3.5), the term linear in $\Delta\tau$ vanishes since a trace over a commutator gives zero. As one can see, the temperature and the systematic error are controlled by the parameters L and $\Delta\tau$. Due to the product over the L slices the error accumulates to $\mathcal{O}(\Delta\tau)$. Some expectation values, defined via Eq. (3.5), only exhibit errors of order $\mathcal{O}((\Delta\tau)^{\nu})$ for $\nu \geq 2$, as for example the total energy [81]. The finite $\Delta\tau$ also plays the role of a high frequency cut-off where $1/\Delta\tau$ is absorbed in the Hubbard-Stratonovich transformation described in the next section. High frequencies originate from the continuous but not differentiable paths in imaginary time,contributing to the path integral, which cannot be represented by a finite number of degrees of freedom on a computer anyway. These frequencies contribute negligibly to most observables and cause no practical limitations in the calculations. In the following we will not explicitly state the Trotter error.

As a consequence of the Suzuki-Trotter decomposition we are able to write the par-

tition function as

$$\begin{aligned} \mathcal{Z} &= \operatorname{tr} \mathrm{e}^{-\beta H_{\mathrm{EH}}^{\mu}} = \operatorname{tr} \mathrm{e}^{-\Delta\tau(H_{\mathrm{k}}+H_{\mathrm{U}}+H_{\mathrm{V}}+H_{\mu})} \\ &= \operatorname{tr} \prod_{L} \left(\mathrm{e}^{-\Delta\tau H_{\mathrm{k}}} \, \mathrm{e}^{-\Delta\tau H_{\mathrm{U}}} \, \mathrm{e}^{-\Delta\tau H_{\mathrm{V}}} \, \mathrm{e}^{-\Delta\tau H_{\mu}} \right) . \end{aligned} \tag{3.12}$$

Here, and in the further expressions we will drop the order of the error term for simplicity and keep in mind this systematic error. For a detailed description of the Suzuki-Trotter decomposition see App. A.1. From now on we distinguish between Monte Carlo time and Trotter time. The propagation in Trotter time (= imaginary time) represents the fluctuations of the quantum mechanical system. This decomposition of non-commuting parts of the Hamiltonian can also be done in continuous imaginary time avoiding the Trotter discretization error as discussed in App. A.1.

3.3 Auxiliary fields

The DetQMC method is based on the formulation of the interactions of the model Hamiltonian in terms of auxiliary-fields and is therefore often referred to as Auxiliary-field-QMC. For comparison of the following description with other works we refer to [82, 83, 84, 85, 86, 87, 88] – we claim to present here a more continuous introduction to the DetQMC.

The DetQMC method works in a space of Slater determinants (basis states of Fock space) which represent the many-body states. Their matrices are built-up by single-particle base states. In order to carry out the trace in Eq. (3.6) we have to write the many-body propagator $\mathrm{e}^{-\beta H}$ in single-particle (bilinear) form, hence as $A = \sum_{ij} a_{ij} c_i^{\dagger} c_j$. This enables us to integrate over the fermionic degrees of freedom explicitly and leaves a pure bosonic theory. Then we can simplify the trace over the exponential fermionic operators $A, B, \ldots$ to a determinant over the matrices (see Sec. A.2)

$$\operatorname{tr} \left\{ \mathrm{e}^{-\sum_{ij} c_i^{\dagger} A_{ij} c_j} \, \mathrm{e}^{-\sum_{ij} c_i^{\dagger} B_{ij} c_j} \ldots \right\} = \det \left(\mathbf{1} + \mathrm{e}^{-\mathbf{A}} \, \mathrm{e}^{-\mathbf{B}} \ldots \right) . \tag{3.13}$$

The electron-electron interaction term is of quadratic order in the densities $n_{i\sigma}$, hence of quartic order in fermion creation (annihilation) operators. In our favored representation only linear dependencies are to be used, thus we have to decouple the interaction term. For the Hubbard model the interaction term H_{U} (not-commuting with the hopping term)

$$\mathrm{e}^{-\Delta\tau H_{\mathrm{U}}} = \mathrm{e}^{-\Delta\tau U \sum n_{i\uparrow} n_{i\downarrow}} \tag{3.14}$$

can be transformed into bilinear form via the Hubbard- Stratonovich transformation [89]. The transformation is based on the identity

$$\mathrm{e}^{\frac{1}{2}A^2} = \frac{1}{\sqrt{2\pi}} \int dx \, \mathrm{e}^{-\frac{1}{2}x^2 - Ax} , \tag{3.15}$$

where the exponential of a square is decomposed by a Gaussian integral. For the Hubbard-term with attractive interaction ($U < 0$), repulsive interaction ($U > 0$) we can write

$$U\, n_{i\uparrow} n_{i\downarrow} = \pm \frac{U}{2} \left((n_{i\uparrow} \pm n_{i\downarrow})^2 - (n_{i\uparrow} + n_{i\downarrow})^2 \right) \ , \tag{3.16}$$

thus the transformation is given by

$$\mathrm{e}^{\Delta\tau \frac{U}{2} (n_{i\uparrow} \mp n_{i\downarrow})^2} = \sqrt{\frac{\Delta\tau}{2\pi}} \int d\phi_i(l)\ \mathrm{e}^{-\frac{\Delta\tau}{2}\phi_i^2(l) + \Delta\tau\sqrt{U}(n_{i\uparrow} \mp n_{i\downarrow})\,\phi_i(l)} \ . \tag{3.17}$$

This replaces the influence of the electron interactions on the motion of a given electron by a space- and time-dependent fictitious field ϕ acting on the electron. Instead of the continuous auxiliary field in Eq. (3.17), it is more convenient to work with discrete variables. Motivated by the fact that the fermion occupation is discrete this results in smaller errors due to the reduced phase space [72]. The transformation reads [90]

$$\exp\left(-\Delta\tau U n_{i\uparrow} n_{i\downarrow}\right) = \frac{1}{2} \sum_{\alpha_i = \pm 1} \exp\left(\lambda_\pm\, \alpha_i \left(n_{i\uparrow} \mp n_{i\downarrow}\right) - \frac{1}{2} \Delta\tau U \left(n_{i\uparrow} + n_{i\downarrow}\right) \right) \ , \tag{3.18}$$

Note that this is an exact identity in the discretized form. The transformation reduces the quadratic self-interaction of the electrons to a linear interaction with the Ising-like variables α_i. The local Coulomb interaction is now in bilinear form and the trace over the fermionic degrees of freedom can be taken easily. This rewriting of a many body problem to a manifold of single particle problems enables us to evaluate the trace in form of a determinant at the price of introducing an additional sum to be carried out.

For a one-dimensional system of N sites, for each density-density interaction $n_i(\tau)\, n_j(\tau)$ in space-time an auxiliary field of L Ising variables is introduced. Note, that the Ising chains for the L time-slices are not perfectly classical systems since they are correlated via the electron density and therefore reveal – depending on the set of parameters (couplings) – quasi-world-line behavior. The connection between the world-line and the determinant functional formulation has been shown by Hirsch in [91]. Back to the transformation, by inserting all possible occupation numbers into Eq. (3.18) we get

$n_{i\uparrow}$	$n_{i\downarrow}$	$\mathrm{e}^{-\Delta\tau U(n_{i\uparrow} n_{i\downarrow})}$	$=$	$\frac{1}{2}\sum_{\alpha=\pm1} \mathrm{e}^{\lambda_\pm\, \alpha\, (n_{i\uparrow} \mp n_{i\downarrow}) - \frac{1}{2}\Delta\tau U (n_{i\uparrow} + n_{i\downarrow})}$
0	0	1	$=$	1
1	0	1	$=$	$\cosh(\lambda_\pm)\, \mathrm{e}^{-\frac{1}{2}\Delta\tau U}$
0	1	1	$=$	$\cosh(\lambda_\pm)\, \mathrm{e}^{-\frac{1}{2}\Delta\tau U}$
1	1	$\mathrm{e}^{-\Delta\tau U}$	$=$	$\mathrm{e}^{-\Delta\tau U}$

and are able to fix the free parameter $\lambda_\pm$ (which must not be confused with the electron-phonon coupling). In order to work with real weights one uses λ_+ (λ_-) for $U > 0$ ($U < 0$).

The real parameter for the on-site Hubbard interaction is then given by

$$\cosh(\lambda_{\mathrm{U}}) = \mathrm{e}^{\frac{1}{2}\Delta\tau U} \qquad \text{or} \qquad \lambda_{\mathrm{U}} = 2\,\mathrm{arctanh}\left(\sqrt{\tanh\left(\Delta\tau U/4\right)}\right) . \tag{3.19}$$

In the case of the nearest neighbor Coulomb interaction H_V the Hubbard-Stratonovich decoupling of the two-body interaction term has to be carried out for all combinations of the two involved spins $(\sigma,\sigma') \in [(\uparrow\uparrow),(\uparrow\downarrow),(\downarrow\uparrow),(\downarrow\downarrow)]$ in $n_{i\sigma}n_{j\sigma'}$ for all space directions – hence four times on each lattice bond. The newly introduced auxiliary Ising-fields $\phi^{x_1}_{\sigma\sigma'}$ and $\phi^{x_2}_{\sigma\sigma'}$, corresponding to the two spatial directions, exist on the bonds between the lattice sites as illustrated in Fig. 3.1 mediating the inter-site interaction. In this case the free parameter is given by

$$\lambda_{\mathrm{V}} = \mathrm{arccosh}\left(\mathrm{e}^{\frac{1}{2}\Delta\tau V}\right) \;=\; 2\,\mathrm{arctanh}\left(\sqrt{\tanh\left(\Delta\tau V/4\right)}\right) . \tag{3.20}$$

The repulsive on-site (inter-site) Coulomb interaction has been replaced by a mediating bosonic field α ($\phi_{\sigma\sigma'}$) which couples to the net spin $\sigma^z_i = (n_\uparrow - n_\downarrow)/2$. The auxiliary fields are massless and provide localized instantaneous interactions. Physically, this amounts to creation of a spin moment in the orbital. A local change in the auxiliary fields leads to a change in the effective potential of the corresponding site. For negative U (attractive interaction) the Ising field couples to the local charge-density. It should be noted that the choice to use the positive solution for λ in Eq. (3.20) breaks the $SU(2)$ spin rotational invariance for a given configuration of the auxiliary fields which is restored after summation over the HS-fields within the ergodic MC-process [83]. Instead it may be convenient to use the negative solution (λ_-) with complex weights. However, in the case of a real-valued computation the positive solution (λ_+) is to be favored due to less computational effort. In appendix A.3 examples for other decoupling-transformations are given.

Now returning, the partition function in Eq. (3.12) has been changed via the Hubbard-Stratonovich transformation to

$$\begin{aligned}
\mathcal{Z} \;&=\; \mathrm{tr}\prod_{L} \mathrm{e}^{-\Delta\tau H_{\mathrm{k}}}\mathrm{e}^{-\Delta\tau H_{\mu}}\mathrm{e}^{-\Delta\tau H_{\mathrm{U}}}\mathrm{e}^{-\Delta\tau H_{\mathrm{V}}} \\
&=\; \mathrm{tr}\Bigg\{ \prod_{l=1}^{L} \mathrm{e}^{-\Delta\tau H_{\mathrm{k}}} \prod_{i=1}^{N} \mathrm{e}^{\Delta\tau\mu(n_{i\uparrow}+n_{i\downarrow})} \\
&\quad\times\quad \frac{1}{2^9} \sum_{\{\alpha(l,i)=\pm 1\}} \mathrm{e}^{\lambda_{\mathrm{U}}\alpha(n_{i\uparrow}-n_{i\downarrow})} \sum_{\{\phi^{x_1}_{\uparrow\uparrow}(l,i)\}} \sum_{\{\phi^{x_1}_{\downarrow\downarrow}(l,i)\}} \sum_{\{\phi^{x_1}_{\uparrow\downarrow}(l,i)\}} \sum_{\{\phi^{x_1}_{\downarrow\uparrow}(l,i)\}} \sum_{\{\phi^{x_1}_{\downarrow\downarrow}(l,i)\}} \\
&\quad\times\quad \mathrm{e}^{\lambda_{\mathrm{V}} n_{i\uparrow}(\phi^{x_1}_{\uparrow\uparrow}+\phi^{x_1}_{\uparrow\downarrow})}\, \mathrm{e}^{\lambda_{\mathrm{V}} n_{i\downarrow}(\phi^{x_1}_{\downarrow\uparrow}+\phi^{x_1}_{\downarrow\downarrow})}\, \mathrm{e}^{-\lambda_{\mathrm{V}} n_{i+1\uparrow}(\phi^{x_1}_{\uparrow\uparrow}+\phi^{x_1}_{\downarrow\uparrow})}\, \mathrm{e}^{-\lambda_{\mathrm{V}} n_{i+1\downarrow}(\phi^{x_1}_{\uparrow\downarrow}+\phi^{x_1}_{\downarrow\downarrow})} \Bigg\} .
\end{aligned} \tag{3.21}$$

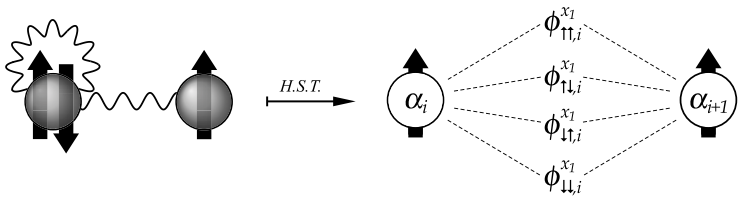

Fig. 3.1: The local and the inter-site Coulomb interaction maps onto Ising-fields α_i and $\phi^{x_1}_{\sigma\sigma'}$, respectively, via the Hubbard-Stratonovich transformation.

Here, {..} stands for all possible configurations of the auxiliary fields (for simplicity, only one dimension x_1 for the inter-site coupling has been taken into account here). We introduced the chemical potential $\mu = \mu_0 - U/2 - n_{\rm nn}V$ which contains the shift resulting from the HS-transformations, where $n_{\rm nn}$ denotes the number of nearest neighbors and μ_0 is the standard chemical potential without corrections. To provide a more compact form we combine the kinetic and the interaction terms separately for each spin $\sigma = \uparrow, \downarrow$ into the single electron propagators

$$\mathcal{B}^\sigma_l = \mathrm{e}^{-\Delta\tau\, c^\dagger_{i\sigma}\,(\mathbf{K})_{ij} c_{j\sigma}}\, \mathrm{e}^{-\Delta\tau\, c^\dagger_{i\sigma}\,(\mathbf{V}^\sigma_l)_{ij} c_{j\sigma}}\ , \tag{3.22}$$

where $\mathbf{K}$ is the tight-binding-style hopping matrix and the interactions are built-in the matrices $\mathbf{V}$ on all time-slices l. For a two dimensional inter-site interaction the matrices are

$$(\mathbf{K})_{ij} = \begin{cases} -t & \text{for } i,\, j \text{ nearest neighbors} \\ 0 & \text{otherwise} \end{cases}\ , \tag{3.23}$$

$$\begin{aligned} (\mathbf{V}^\sigma_l)_{ij} = {} & \delta_{ij}\{\mu + \frac{1}{\Delta\tau}\sigma\lambda_{\rm U}\,\alpha(l,i) \\ & + \frac{1}{\Delta\tau}\lambda_{\rm V}(\phi^{x_1}_{\sigma\uparrow}(l,i) + \phi^{x_1}_{\sigma\downarrow}(l,i) - \phi^{x_1}_{\uparrow\sigma}(l,i-1) - \phi^{x_1}_{\downarrow\sigma}(l,i-1) \\ & + \phi^{x_2}_{\sigma\uparrow}(l,i) + \phi^{x_2}_{\sigma\downarrow}(l,i) - \phi^{x_2}_{\uparrow\sigma}(l,i-1-n_x) - \phi^{x_2}_{\downarrow\sigma}(l,i-1-n_x))\}\ . \end{aligned} \tag{3.24}$$

We have now expressed the partition function Eq. (3.12) in terms of auxiliary fields

$$\mathcal{Z} = \frac{1}{2^{9NL}} \sum_{\{\alpha(l)\}} \sum_{\{\phi^{x_1}_{\uparrow\uparrow}(l)\}} \dots \sum_{\{\phi^{x_2}_{\downarrow\downarrow}(l)\}} \mathrm{tr} \prod_{l=1}^{L} \mathcal{B}^\uparrow_l\, \mathcal{B}^\downarrow_l\ . \tag{3.25}$$

The next step is to take the trace over fermions explicitly. Following Hirsch [72] we use the identity given in Eq. (3.13) and specified in App. A.2 to write the trace as

$$\mathcal{Z} = \frac{1}{2^{9NL}} \sum_{\{\alpha(l)\}} \sum_{\{\phi^{x_1}_{\uparrow\uparrow}(l)\}} \dots \sum_{\{\phi^{x_2}_{\downarrow\downarrow}(l)\}} \prod_{\sigma} \det\left(\mathbf{1} + \mathbf{B}^\sigma_L \dots \mathbf{B}^\sigma_1\right)\ . \tag{3.26}$$

Here the matrices $\mathbf{B}_l^\sigma = \mathrm{e}^{-\Delta\tau\,\mathbf{K}}\,\mathrm{e}^{-\Delta\tau\,\mathbf{V}_l^\sigma}$ represent the operators $\mathcal{B}_l^\sigma$. In this step the $(LN)^2$-Slater determinant is reduced to N^2-matrices via recursion. Alternatively, one can prove this by working in a coherent state basis with Grassmann variables [74]. Introducing

$$\mathbf{M}^\sigma[\check{x}] = \mathbf{1} + \mathbf{B}_L^\sigma \ldots \mathbf{B}_1^\sigma \;, \tag{3.27}$$

where $\{x\}$ represents all configurations x of the auxiliary fields, we arrive at a formulation which makes clear the expression *determinant* Quantum Monte Carlo

$$\mathcal{Z} = \frac{1}{2^{9NL}}\;\mathrm{tr}\;\left\{\det\mathbf{M}^\uparrow[\check{x}]\cdot\det\mathbf{M}^\downarrow[\check{x}]\right\}\;. \tag{3.28}$$

In this last equality the product of determinants defines an effective density matrix. To conclude this subsection: we have rewritten the integral over the mixed-fermionic-bosonic action to a sum over the auxiliary field configurations only, by doing the sum over the fermions exactly

$$\mathcal{Z} = \sum_{\{\check{x}\}}\sum_{\text{fermionic}}\mathrm{e}^{-S} = \frac{1}{2^{9NL}}\;\sum_{\{\check{x}\}}\prod_\sigma\det\mathbf{M}^\sigma[\check{x}] = \sum_{\{\check{x}\}} w_\mathrm{f}[\check{x}]\;. \tag{3.29}$$

Here, $w_f[\check{x}]$ denotes the weight for a configuration $\check{x} = \{\alpha, \phi^{x_1}, \phi^{x_2}\}$ which will be integrated stochastically to obtain the partition function. We will refer to it as the fermionic weight, although we are left with a sampling over Ising-like degrees of freedom only.

3.4 The propagator

In this section we will deduce the Green's function in the DetQMC formulation as the central object in the simulation. The Green's function will play two essential roles: the first one is in the importance sampling of the auxiliary fields discussed in the following section, whereas the second one is in measurements of the electronic degrees of freedom, which will be the subject of Sec. 4.1[2].

The matrix elements of the equal-time one-particle Green's function are [93]

$$\mathcal{G}_{ij}^\sigma(\tau,\tau) := \left\langle c_{i\sigma}(\tau)\,c_{j\sigma}^\dagger(\tau)\right\rangle = \delta_{ij} - \left\langle c_{j\sigma}^\dagger(\tau)\,c_{i\sigma}(\tau)\right\rangle \tag{3.30}$$

where $\langle\ldots\rangle$ represents the expectation value over the grand canonical ensemble. Though Eq. (3.30) is a common notation, the equal-time one-particle Green's function is independent of τ. We will express the Green's function in terms of the introduced single electron

[2] According to Wick's theorem all desired measurements can be derived from the Green's function [92].

propagators $\mathcal{B}_l^\sigma$ – similar to the partition function. Following Loh and Gubernatis [82] we can write the operator $c_{j\sigma}^\dagger\, c_{i\sigma}$ as

$$c_{j\sigma}^\dagger\, c_{i\sigma} = \frac{\partial}{\partial h}\, \mathrm{e}^{h\, c_{j\sigma}^\dagger\, c_{i\sigma}}\Big|_{h=0} = \frac{\partial}{\partial h} \prod_{ab\sigma'} \mathrm{e}^{h\, c_{a\sigma'}^\dagger\, O_{ab}^{\sigma'} c_{b\sigma'}}\Big|_{h=0} \tag{3.31}$$

with the matrix $\mathbf{O}^{\sigma'}$ containing only the single nonzero element $O_{ab}^{\sigma'} = O_{ji}^{\sigma} = 1$. Now the expectation value of the Green's function reads

$$\begin{aligned}
\left\langle c_{j\sigma}^\dagger(\tau_l)\, c_{i\sigma}(\tau_l)\right\rangle &= \delta_{ij} - \mathcal{G}_{ij}^\sigma(\tau_l,\tau_l) \\
&:= \frac{1}{\mathcal{Z}}\frac{\partial}{\partial h}\mathrm{tr}\, \mathrm{e}^{-(\beta-\tau_l)H} \mathrm{e}^{h\, c_{a\sigma'}^\dagger\, O_{ab}^{\sigma'} c_{b\sigma'}} \mathrm{e}^{-\tau_l H}\Big|_{h=0} \\
&= \frac{1}{2^{9LN}}\frac{1}{\mathcal{Z}}\frac{\partial}{\partial h} \sum_{\{\alpha_i(l)\}} \cdots \sum_{\{\phi_{\downarrow\downarrow}^{x_2}(l)\}} \\
&\qquad \times \prod_{\sigma'} \det(\mathbf{1} + \mathbf{B}_L^{\sigma'} \ldots \mathbf{B}_{l+1}^{\sigma'}\, \mathrm{e}^{h\mathbf{O}^{\sigma'}}\, \mathbf{B}_l^{\sigma'} \ldots \mathbf{B}_1^{\sigma'})\Big|_{h=0} \\
&= \frac{1}{2^{9LN}}\frac{1}{\mathcal{Z}}\frac{\partial}{\partial h} \sum_{\{\alpha_i(l)\}} \cdots \sum_{\{\phi_{\downarrow\downarrow}^{x_2}(l)\}} \prod_{\sigma',\sigma'',\sigma'''} \det(\mathbf{1} + \mathbf{B}_L^{\sigma''} \ldots \mathbf{B}_1^{\sigma''}) \\
&\qquad \times \frac{\det(\mathbf{1} + \mathbf{B}_L^{\sigma'} \ldots \mathbf{B}_{l+1}^{\sigma'}\, \mathrm{e}^{h\mathbf{O}^{\sigma'}}\, \mathbf{B}_l^{\sigma'} \ldots \mathbf{B}_1^{\sigma'})}{\det(\mathbf{1} + \mathbf{B}_L^{\sigma'''} \ldots \mathbf{B}_1^{\sigma'''})}\Bigg|_{h=0}
\end{aligned} \tag{3.32}$$

Expression Eq. (3.32) represents the expectation value of the Green's function in the DetQMC formulation, where

$$w_{\mathrm{f}}[\check{x}] = \frac{1}{2^{9LN}}\frac{1}{\mathcal{Z}} \prod_{\sigma''} \det(\mathbf{1} + \mathbf{B}_L^{\sigma''} \ldots \mathbf{B}_1^{\sigma''})\,, \tag{3.33}$$

is the fermionic weight which has been already defined in Eq. (3.29) and

$$\delta_{ij} - G_{ij}^\sigma(\tau_l,\tau_l) := \frac{\partial}{\partial h} \prod_{\sigma',\sigma'''} \frac{\det(\mathbf{1} + \mathbf{B}_L^{\sigma'} \ldots \mathbf{B}_{l+1}^{\sigma'}\, \mathrm{e}^{h\mathbf{O}^{\sigma'}}\, \mathbf{B}_l^{\sigma'} \ldots \mathbf{B}_1^{\sigma'})}{\det(\mathbf{1} + \mathbf{B}_L^{\sigma'''} \ldots \mathbf{B}_1^{\sigma'''})}\Bigg|_{h=0}\,, \tag{3.34}$$

is the Green's function for a specific configuration $\check{x}$ of auxiliary fields. Here we use the symbol G instead of $\mathcal{G}$ which we use for the operator. Hence Eq. (3.32) can also be written as

$$\left\langle c_{j\sigma}^\dagger(\tau_l)\, c_{i\sigma}(\tau_l)\right\rangle = \delta_{ij} - \mathcal{G}_{ij}^\sigma(\tau_l,\tau_l) := \sum_{\{\check{x}\}} w_{\mathrm{f}}[\check{x}]\left(\delta_{ij} - G_{ij}^\sigma(\tau_l,\tau_l)\right)\,. \tag{3.35}$$

The expression in Eq. (3.34) can be simplified via the identity[3] $\ln\det\mathbf{A} = \mathrm{tr}\ln\mathbf{A}$ to

$$\begin{aligned}
\delta_{ij} - G^{\sigma}_{ij}(\tau_l,\tau_l) &= \frac{\partial}{\partial h}\ln\det(\mathbf{1}+\mathbf{B}^{\sigma}_{L}\dots\mathbf{B}^{\sigma}_{l+1}\,\mathrm{e}^{h\mathbf{O}^{\sigma}}\,\mathbf{B}^{\sigma}_{l}\dots\mathbf{B}^{\sigma}_{1})\,\Big|_{h=0} \\
&= \frac{\partial}{\partial h}\,\mathrm{tr}\,\ln(\mathbf{1}+\mathbf{B}^{\sigma}_{L}\dots\mathbf{B}^{\sigma}_{l+1}\,\mathrm{e}^{h\mathbf{O}^{\sigma}}\,\mathbf{B}^{\sigma}_{l}\dots\mathbf{B}^{\sigma}_{1})\,\Big|_{h=0} \\
&= \mathrm{tr}\,(\mathbf{1}+\mathbf{B}^{\sigma}_{L}\dots\mathbf{B}^{\sigma}_{1})^{-1}\mathbf{B}^{\sigma}_{L}\dots\mathbf{B}^{\sigma}_{l+1}\mathbf{O}^{\sigma}\mathbf{B}^{\sigma}_{l}\dots\mathbf{B}^{\sigma}_{1} \\
&= \left[\mathbf{B}^{\sigma}_{l}\dots\mathbf{B}^{\sigma}_{1}(\mathbf{1}+\mathbf{B}^{\sigma}_{L}\dots\mathbf{B}^{\sigma}_{1})^{-1}\mathbf{B}^{\sigma}_{L}\dots\mathbf{B}^{\sigma}_{l+1}\right]_{ij} \\
&= \left[\mathbf{1}+(\mathbf{B}^{\sigma}_{l+1})^{-1}\dots(\mathbf{B}^{\sigma}_{L})^{-1}(\mathbf{B}^{\sigma}_{1})^{-1}\dots(\mathbf{B}^{\sigma}_{l})^{-1}\right]^{-1}_{ij}\,. \qquad (3.36)
\end{aligned}$$

In the last step we used the identity $(\mathbf{XY})^{-1} = \mathbf{Y}^{-1}\mathbf{X}^{-1}$ to multiply out the inverse of the exprtess in the parenthesis. The Green's function at a time-slice l is then given by

$$\mathbf{G}^{\sigma}(\tau_l,\tau_l) = \left(\mathbf{1}+\mathbf{B}^{\sigma}_{l}\dots\mathbf{B}^{\sigma}_{1}\,\mathbf{B}^{\sigma}_{L}\dots\mathbf{B}^{\sigma}_{l+1}\right)^{-1}\,. \qquad (3.37)$$

This major result enables us to evaluate the partition function by calculating the product of the single electron propagators $\mathbf{B}^{\sigma}_{l}$ of all time-slices for all possible configurations of the auxiliary fields. As simple as this sounds, note that there exist 2^{5NL} configurations (in one dimension). A typical system treated in this thesis has about $10^{55,600}$ possible configurations (no phonons have been taking into account here), which would correspond to a 430×430 classical 2D-Ising model. This sounds not too bad, but one is confronted with a product of 160 matrices of sizes up to 128×128 and its inverse for each and every configuration. Computing this product $10^{55,600}$ times – that takes a very long time! No need to despair, cheer up – there is Monte Carlo!

3.5 Single spin-flip and the MC-update

The integration over all configuration of the auxiliary fields has now to be performed via Monte Carlo. According to the weight w_{f} defined in Eq. (3.33) a Markov-chain of field configurations is generated. In this stochastic process, the number of samples needed to obtain reasonably good measurements on the physical system is many orders of magnitude smaller than the whole configuration space. Let $\langle A(\check{x})\rangle$ be the expectation value of the operator A for a field configuration $\check{x} = \{\alpha, \phi^{x_1}, \phi^{x_2}\}$. The expectation value in the MC-process is given by

$$\langle A\rangle = \frac{\sum_{\{\check{x}\}} w_{\mathrm{f}}[\check{x}]\;A(x)}{\sum_{\{\check{x}\}} w_{\mathrm{f}}[\check{x}]}\,. \qquad (3.38)$$

[3] This identity may be formally shown by expanding the logarithm and using the cyclic properties of the trace.

An appropriate method to sample new auxiliary field configurations with high acceptance rates within the MC-process is needed. To compute the fermionic weight w_f according to Eq. (3.33) the determinant of the expensive matrix product of the L $\mathbf{B}^\sigma$-matrices is needed. To reduce the effort to determine the weight of a proposal configuration (which might be rejected) we stick to single spin-flip updates. These updates can be made at minor costs compared to the evaluation of the matrix products in Eq. (3.33).

For a given auxiliary field configuration the probability R of flipping a single Ising spin is calculated. R is given by the ratio of the current and the proposed weight of both configurations.

$$R = \frac{w_\mathrm{f}'}{w_\mathrm{f}} \,. \tag{3.39}$$

When the Ising-spin on site j of the on-site Coulomb repulsion field α flips

$$\alpha(l,j) \to \alpha(l,j)' = -\alpha(l,j) \,, \tag{3.40}$$

then the interaction matrix $\mathbf{V}_l$ and the matrix $\mathbf{B}_l^\sigma$ change

$$\begin{aligned} (\mathbf{V}_l^\sigma)'_{jj} &\to (\mathbf{V}_l^\sigma)_{jj} \mp 2\sigma\lambda_\mathrm{U}\alpha(l,j) \\ (\mathbf{B}_l^\sigma)' &\to (\mathbf{1} + \mathbf{\Delta}_l^\sigma)\ \mathbf{B}_l^\sigma \,, \end{aligned} \tag{3.41}$$

where we introduced the matrix $\mathbf{\Delta}_l^\sigma$ containing only one nonzero element

$$(\mathbf{1} + \mathbf{\Delta}_l^\sigma)_{jj} = \mathrm{e}^{-2\sigma\,\lambda_\mathrm{U}\,\alpha(l,j)} \,. \tag{3.42}$$

The auxiliary fields for the inter-site Coulomb interaction are treated analogous to the on-site interaction. For a flip

$$\phi_{\sigma\sigma'}(l,i) \to \phi_{\sigma\sigma'}(l,i)' = -\phi_{\sigma\sigma'}(l,i) \,, \tag{3.43}$$

where $\sigma' = \sigma$ we get the changes

$$\begin{aligned} (\mathbf{V}_l^\sigma)'_{jj} &\to (\mathbf{V}_l^\sigma)_{jj} - 2\lambda_\mathrm{V}\phi_{\sigma\sigma'}(l,i) \\ (\mathbf{V}_l^\sigma)'_{j+1,j+1} &\to (\mathbf{V}_l^\sigma)_{j+1,j+1} - 2\lambda_\mathrm{V}\phi_{\sigma\sigma'}(l,i) \\ (\mathbf{B}_l^\sigma)' &\to (\mathbf{1} + \mathbf{\Delta}_1 + \mathbf{\Delta}_2)\ \mathbf{B}_l^\sigma \end{aligned} \tag{3.44}$$

$$\begin{aligned} (\mathbf{\Delta}_1)_{mn} &= (\mathrm{e}^{-2\lambda_\mathrm{V}\phi_{\sigma\sigma'}(l,i)} - 1)\,\delta_{mi}\,\delta_{in} \\ (\mathbf{\Delta}_2)_{mn} &= (\mathrm{e}^{2\lambda_\mathrm{V}\phi_{\sigma\sigma'}(l,i)} - 1)\,\delta_{m,i+1}\,\delta_{i,n+1} \,. \end{aligned}$$

For the case $\sigma' = -\sigma$ the changes are

$$\begin{aligned}
\phi_{\sigma\sigma'}(l,i)' &\rightarrow -\phi_{\sigma\sigma'}(l,i) \\
(\mathbf{V}_l^\sigma)'_{jj} &\rightarrow (\mathbf{V}_l^\sigma)_{jj} - 2\lambda_{\mathrm{V}}\phi_{\sigma\sigma'}(l,i) \\
(\mathbf{V}_l^\sigma)'_{j+1,j+1} &\rightarrow (\mathbf{V}_l^\sigma)_{j+1,j+1} - 2\lambda_{\mathrm{V}}\phi_{\sigma\sigma'}(l,i) \\
(\mathbf{B}_l^\sigma)' &\rightarrow (\mathbf{1} + \mathbf{\Delta}_1)\ \mathbf{B}_l^\sigma \qquad (3.45) \\
(\mathbf{B}_l^{\sigma'})' &\rightarrow (\mathbf{1} + \mathbf{\Delta}_2)\ \mathbf{B}_l^{\sigma'} \qquad (3.46)
\end{aligned}$$

$$\begin{aligned}
(\mathbf{\Delta}_1)_{mn} &= (\mathrm{e}^{-2\lambda_{\mathrm{V}}\phi_{\sigma\sigma'}(l,i)} - 1)\,\delta_{mi}\,\delta_{in} \\
(\mathbf{\Delta}_2)_{mn} &= (\mathrm{e}^{2\lambda_{\mathrm{V}}\phi_{\sigma\sigma'}(l,i)} - 1)\,\delta_{m,i+1}\,\delta_{i,n+1}\ .
\end{aligned}$$

The acceptance probabilities can now be calculated via the changes in the $\mathbf{B}_l^\sigma$ matrices. According to Eq. (3.39) we compare the configuration weights of Eq. (3.33) for a flip of a single Ising-spin in the α-field

$$\begin{aligned}
R^\sigma &= \frac{\det\left(\mathbf{1} + \mathbf{B}_L^\sigma \dots \mathbf{B}_{l+1}^\sigma\,(\mathbf{1} + \mathbf{\Delta}_l^\sigma)\ \mathbf{B}_l^\sigma \dots \mathbf{B}_1^\sigma\right)}{\det(\mathbf{1} + \mathbf{B}_L^\sigma \dots \mathbf{B}_{l+1}^\sigma \mathbf{B}_l^\sigma \dots \mathbf{B}_1^\sigma)} \\
&= \frac{\det\left(\mathbf{1} + \mathbf{B}_L^\sigma \dots \mathbf{B}_1^\sigma + \mathbf{B}_L^\sigma \dots \mathbf{B}_{l+1}^\sigma \mathbf{\Delta}_l^\sigma\ \mathbf{B}_l^\sigma \dots \mathbf{B}_1^\sigma\right)}{\det(\mathbf{1} + \mathbf{B}_L^\sigma \dots \mathbf{B}_1^\sigma)} \\
&= \det\left(\mathbf{1} + (\mathbf{1} + \mathbf{B}_L^\sigma \dots \mathbf{B}_1^\sigma)^{-1}\,\mathbf{B}_L^\sigma \dots \mathbf{B}_{l+1}^\sigma \mathbf{\Delta}_l^\sigma\ \mathbf{B}_l^\sigma \dots \mathbf{B}_1^\sigma\right) \\
&= \det\left(\mathbf{1} + \mathbf{\Delta}_l^\sigma\ \mathbf{B}_l^\sigma \dots \mathbf{B}_1^\sigma (\mathbf{1} + \mathbf{B}_L^\sigma \dots \mathbf{B}_1^\sigma)^{-1} \mathbf{B}_L^\sigma \dots \mathbf{B}_{l+1}^\sigma\right) \\
&= \det\left(\mathbf{1} + \mathbf{\Delta}_l^\sigma\ (\mathbf{1} - (\mathbf{B}_l^\sigma \dots \mathbf{B}_1^\sigma \mathbf{B}_L^\sigma \dots \mathbf{B}_{l+1}^\sigma)^{-1})\right) \\
&= \det\left(\mathbf{1} + \mathbf{\Delta}_l^\sigma\ (\mathbf{1} - \mathbf{G}^\sigma(\tau_l,\tau_l))\right)\ . \qquad (3.47)
\end{aligned}$$

Here, the cyclic rearrangement under the determinant is allowed since only quadratic matrices with well-defined inverses are involved. The acceptance probability to flip a spin at site j of the auxiliary field α at time-slice l is determined

$$R = R^\uparrow\, R^\downarrow = \prod_\sigma \left(1 + \Delta_{jj}^\sigma\,\left(1 - G_{jj}^\sigma(\tau_l,\tau_l)\right)\right)\ . \qquad (3.48)$$

In a similar fashion the acceptance probability for single spin-flips in the $\phi_{\sigma\sigma'}$-fields for $\sigma = \sigma'$ is obtained. We drop the Trotter-slice index for simplicity and have

$$R^\sigma = \det\left(\mathbf{1} + (\mathbf{1} - \mathbf{G}^\sigma)\,(\mathbf{\Delta}_1 + \mathbf{\Delta}_2)\right)\ , \qquad (3.49)$$

where expanding the determinant yields

$$\begin{aligned}
R^\sigma &= \left[1 + \left(1 - G_{jj}^\sigma\right)\,\Delta_{1,jj}\right]\left[1 + \left(1 - G_{j+1,j+1}^\sigma\right)\Delta_{2,j+1,j+1}\right] \qquad (3.50) \\
&\quad -G_{j,j+1}^\sigma\,\Delta_{1,jj}\,G_{j+1,j}^\sigma\,\Delta_{2,j+1,j+1}\ , \\
R^{-\sigma} &= 1\ . \qquad (3.51)
\end{aligned}$$

For the spin-flip in $\phi_{\sigma\sigma'}$ with $\sigma' = -\sigma$ we have

$$R^{\sigma} = \left[1 + \left(1 - G^{\sigma}_{jj}\right)\, \Delta_{1,jj}\right] \tag{3.52}$$

$$R^{-\sigma} = \left[1 + \left(1 - G^{-\sigma}_{j+1,j+1}\right)\, \Delta_{2,j+1,j+1}\right] \,. \tag{3.53}$$

Again the acceptance probability R is given by the product of $R = R^{\uparrow}R^{\downarrow}$, here a bit more complicated. One can now do a Metropolis- [65] or heatbath-update (or Gibbs sampler) [67] where the probabilities are given by

$$\begin{array}{cc} \text{Metropolis sampler} & \text{Heatbath-Gibbs sampler} \\ P_{\text{acc}} = \min[1, R] = \min\left[1, \dfrac{w'_{\text{f}}}{w_{\text{f}}}\right] \,, & P_{\text{acc}} = \min\left[1, \dfrac{R}{1+R}\right] = \min\left[1, \dfrac{w'_{\text{f}}}{w_{\text{f}} + w'_{\text{f}}}\right] \,. \end{array} \tag{3.54}$$

The choice of the Metropolis-update guarantees optimal single spin-flip sampling in a Ising-like system with respect to the autocorrelation time and variance as demonstrated in [94] and [95]. For both cases the spin-flip is accepted if the probability P_{acc} is greater than a uniformly distributed pseudo random number in the interval $[0, 1)$.

The single spin-flip move enables us to generate a cheap (in the sense of computation time) proposal for a new configuration. We will see in the following that this local change in the auxiliary field leads to a simple rescaling of the elements of the Green's function which as already has been mentioned will be needed for the measurement of observables. The drawback of the single spin-flip is that consecutive configurations are highly correlated and independent field configurations are obtained only by skipping a large number of updates between measurements. More on this problem will be discussed in Sec. 3.9.1 and Sec. 3.6.2 about nonlocal updating-schemes.

If single spin-flip move at a site on time-slice l is accepted, the Green's function changes to[4]

$$\begin{aligned} (\mathbf{G}^{\sigma}_{l})' &= \left(\mathbf{1} + (\mathbf{1} + \mathbf{\Delta}^{\sigma}_{l})\, \mathbf{B}^{\sigma}_{l} \ldots \mathbf{B}^{\sigma}_{1}\, \mathbf{B}^{\sigma}_{L} \ldots \mathbf{B}^{\sigma}_{l+1}\right)^{-1} \\ &= \mathbf{G}^{\sigma}_{l}\, \left(\mathbf{1} + \mathbf{\Delta}^{\sigma}_{l}(\mathbf{G}^{\sigma-1}_{l} - 1)\mathbf{G}^{\sigma}_{l}\right)^{-1} \\ &= \mathbf{G}^{\sigma}_{l}\, \left(\mathbf{1} + \mathbf{\Delta}^{\sigma}_{l}(1 - \mathbf{G}^{\sigma}_{l})\right)^{-1} \,, \end{aligned} \tag{3.55}$$

where we use the abbreviation $\mathbf{G}^{\sigma}_{l}$ for $\mathbf{G}^{\sigma}(\tau_l, \tau_l)$. The sparse matrix $\mathbf{\Delta}^{\sigma}_{l}(1 - \mathbf{G}^{\sigma}_{l})$ can be numerically effectively evaluated with the Sherman-Woodbury and Morrison formulas [96], which are used to calculate small changes in an inverse of a matrix without invoking the full machinery of matrix inversion. We use the Ansatz

$$(\mathbf{1} + \mathbf{\Delta}^{\sigma}_{l}(\mathbf{1} - \mathbf{G}^{\sigma}_{l}))^{-1} = (\mathbf{1} + x\mathbf{\Delta}^{\sigma}_{l}(\mathbf{1} - \mathbf{G}^{\sigma}_{l})) = \mathbf{Q}^{-1} \tag{3.56}$$

[4] Eq. (3.55) corresponds to a rearrangement of the Dyson equation $(\mathbf{G}^{\sigma}_{l})' = \mathbf{G}^{\sigma}_{l} - (\mathbf{G}^{\sigma}_{l})'\mathbf{\Delta}^{\sigma}_{l}(1 - \mathbf{G}^{\sigma}_{l})$.

for the inverse. Since the matrix $\mathbf{\Delta}_l^\sigma$ consists of a single non-zero element we can easily evaluate

$$\mathbf{Q}^{-1}\mathbf{Q} = \mathbf{1} = (\mathbf{1} + x\mathbf{\Delta}_l^\sigma(\mathbf{1} - \mathbf{G}_l^\sigma))\,(\mathbf{1} + \mathbf{\Delta}_l^\sigma(\mathbf{1} - \mathbf{G}_l^\sigma))\ , \tag{3.57}$$

which gives us for $x = 1/(1 + \mathbf{\Delta}_l^\sigma(\mathbf{1} - \mathbf{G}_l^\sigma))$. We can now *update* the Green's function after a change in the α-field easily by

$$\mathbf{G}^\sigma(\tau_l, \tau_l)' = \mathbf{G}^\sigma(\tau_l, \tau_l) - \frac{\mathbf{\Delta}_l^\sigma}{R^\sigma}\,(\mathbf{1} - \mathbf{G}^\sigma(\tau_l, \tau_l))\,\mathbf{G}^\sigma(\tau_l, \tau_l)\ . \tag{3.58}$$

For a flip made in a $\phi_{\sigma\sigma'}$-field with $\sigma = \sigma'$ the update is given as (Trotter-slice index has been dropped on the rhs for simplicity)

$$\begin{aligned} G_{km}^\sigma(\tau_l, \tau_l)' &= G_{a,km}^\sigma - \frac{\left(1 - G_{a,k,j+1}^\sigma\right) G_{a,j+1,m}^\sigma \Delta_{2,j+1,j+1}}{1 + \left(1 - G_{a,j+1,j+1}^\sigma\right)\Delta_{2,j+1,j+1}}\ , \\ \text{with } G_{a,km}^\sigma &= G_{km}^\sigma - \frac{\left(1 - G_{kj}^\sigma\right) G_{jm}^\sigma \Delta_{1,jj}}{1 + \left(1 - G_{jj}^\sigma\right)\Delta_{1,jj}}\ , \end{aligned} \tag{3.59}$$

and for $\sigma' = -\sigma$ we have

$$G_{km}^\sigma(\tau_l, \tau_l)' = G_{km}^\sigma - \frac{\Delta_{1,jj}}{R^\sigma}\left(1 - G_{kj}^\sigma\right) G_{jm}^\sigma\ , \tag{3.60}$$

$$G_{km}^{-\sigma}(\tau_l, \tau_l)' = G_{km}^{-\sigma} - \frac{\Delta_{2,j+1,j+1}}{R^{-\sigma}}\left(1 - G_{k,j+1}^{-\sigma}\right) G_{j+1,m}^{-\sigma}\ . \tag{3.61}$$

As we have now proposed a new configuration via, e.g. Eq. (3.48) and updated the Green's function via according to NEWG we can process all sites of the auxiliary fields on the time-slice and are ready to do so as well on the next time-slice. To *wrap* to the next (preceding) slice the corresponding $\mathbf{B}_l^\sigma$ matrices have to be applied to the Green's function

$$\mathbf{G}^\sigma(\tau_{l+1}, \tau_{l+1}) = \mathbf{B}_{l+1}^\sigma\,\mathbf{G}^\sigma(\tau_l, \tau_l)\,(\mathbf{B}_{l+1}^\sigma)^{-1}\ , \tag{3.62}$$

$$\mathbf{G}^\sigma(\tau_{l-1}, \tau_{l-1}) = (\mathbf{B}_{l-1}^\sigma)^{-1}\,\mathbf{G}^\sigma(\tau_l, \tau_l)\,\mathbf{B}_{l-1}^\sigma\ , \tag{3.63}$$

respectively, which results in a product like given by Eq. (3.37). Now we have all tools to effectively generate a Markov-chain of auxiliary-field configurations.

The numerical effort is of the order $\mathcal{O}(N^2)$, whereas the standard matrix product would be of the order $\mathcal{O}(N^3)$. Unfortunately, one cannot restrict oneself to calculate the changes in the propagator this way since the matrices are numerical ill-conditioned and numerical errors would accumulate very fast updating single matrix elements only. Thus, the calculation of the Green's function via direct multiplication of the $\mathbf{B}_l^\sigma$ matrices is necessary at regular intervals, i.e. every few (~ 8) time slices. The required number of these stabilization points needed increases with U and V (latter needs more changes

in the Green's function and therefore destabilzises the calculation faster) and is set to preserve numerical accuracy[5]. By saving partial products from the construction of the Green's function, one can severely reduce the computational effort

$$\mathbf{G}^{\sigma}(\tau_{l_2},\tau_{l_2}) = (\mathbf{1} + \mathbf{B}^{\sigma}_{l_2} \dots \underbrace{\mathbf{B}^{\sigma}_{l_1} \dots \mathbf{B}^{\sigma}_{1}\, \mathbf{B}^{\sigma}_{L} \dots \mathbf{B}^{\sigma}_{l_2+1}}_{\text{unchanged}})^{-1} \,. \tag{3.64}$$

Let l_1 be the last time the Green's function has been calculated from scratch, only the four to eight matrices $\mathbf{B}^{\sigma}_{l_2}, \dots, \mathbf{B}^{\sigma}_{l_1+1}$ have to be multiplied with the unchanged matrix product in order to obtain the Green's function at time-slice l_2. The computational effort for a whole lattice sweep is therefore made up by $L \cdot N$ proposals for new configurations at the cost of $\mathcal{O}(N^2)$ plus L standard matrix products of $\mathcal{O}(N^3)$. Hence, this is an overall effort of $\mathcal{O}(2\,L\,N^3)$[6]. Nevertheless, the updating via single spin-flips is effective in generating new configurations with respect to computation time, but causes long autocorrelation times.

We have rewritten the problem of interacting electrons as problem of independent electrons moving under the influence of a time dependent field. The complex many-body problem has been reduced to a sum of simple problems. From the basic quantity of the algorithm – the elementary Green's function – all possible observables can be calculated as discussed in Sec. 4.1.1. What is left are the phonon degrees of freedom treated in the next section. Methods to overcome numerical instabilities and autocorrelation times will be discussed in the following sections.

3.6 Auxiliary field QMC under Lang-Firsov transformation

We now extend the so far purely electronic DetQMC by phononic degrees of freedom in form of dispersionless Einstein-phonons treated under Lang-Firsov (LF) transformation. As described in Sec. 2.9 the LF transformation adds a complex phase to the hopping-term which has not been taken into account in the QMC-algorithm described so far. Nevertheless, this drawback which forces us to compute with complex values favors the use of a spin-symmetry conserving HS-transformation, which is advantageous for convergence of the MC simulation.

In addition to the decoupling of the oscillators, the LF transformed Hamiltonian provides a formulation for an efficient MC-update of the phonon degrees of freedom.

[5] This way, the maximum (mean) deviation of Green's function matrix elements from numerically exact values is usually of the order 10^{-10} (10^{-12}), which is orders of magnitude smaller than the statistical uncertainty of results.

[6] Here, no additional needed decompositions have been taken into account. These will be discussed in Sec. 3.7.

3.6.1 Changes in the algorithm

In this section we follow the approach for spinless fermions by Hohenadler et al [43] and extended it to the extended Hubbard Holstein model. Let us recall the extended Hubbard Holstein Hamiltonian under LF-transformation in grand-canonical representation

$$\begin{aligned}\tilde{H}^{\mu} &= \sum_{<ij>,\sigma} t_{ij}\, \mathrm{e}^{i\gamma(p_i-p_j)} \left(c^{\dagger}_{i\sigma}c_{j\sigma} + c^{\dagger}_{j\sigma}c_{i\sigma}\right) + \tilde{U}\sum_i n_{i\uparrow}n_{i\downarrow} + V\sum_{<ij>} n_i n_j \\ &\quad + \frac{\omega_0}{2}\sum_i \left(p_i^2 + x_i^2\right) - \tilde{\mu}\sum_i n_i \,, \end{aligned} \tag{3.65}$$

with the effective couplings $\tilde{U} = U - 2\,E_{\mathrm{P}}$ and $\tilde{\mu} = \mu_0 - U/2 - n_{\mathrm{nn}}V + E_{\mathrm{P}}$. Applying the Suzuki-Trotter decomposition we can write the EHH Hamiltonian under LF-transformation as

$$\mathrm{e}^{-\beta\tilde{H}^{\mu}} \approx \left(\mathrm{e}^{-\Delta\tau\tilde{H}_{\mathrm{k}}}\,\mathrm{e}^{-\Delta\tau\tilde{H}_{\mathrm{U}}}\,\mathrm{e}^{-\Delta\tau\tilde{H}_{\mathrm{V}}}\,\mathrm{e}^{-\Delta\tau\tilde{H}_{\mathrm{osc,p}}}\,\mathrm{e}^{-\Delta\tau\tilde{H}_{\mathrm{osc,x}}}\,\mathrm{e}^{-\Delta\tau\tilde{H}_{\mu}}\right)^L \equiv \mathcal{U}\,, \tag{3.66}$$

with $\Delta\tau = \beta/L$. Here we have split up the oscillator term into $\tilde{H}_{\mathrm{osc}} = \tilde{H}_{\mathrm{osc,p}} + \tilde{H}_{\mathrm{osc,x}}$ (see Eq. (3.21)). The trace in the partition function $\mathcal{Z} = \mathrm{tr}\,\mathrm{e}^{-\beta\tilde{H}^{\mu}}$ can be split up into a bosonic and a fermionic component. Inserting L complete sets of momentum eigenstates leads to the approximation for the partition function

$$\mathcal{Z} = \mathrm{tr}\int \mathrm{d}P_1\,\mathrm{d}P_2\,\ldots\mathrm{d}P_L\,\big\langle P_1\big|\mathcal{U}\big|P_2\big\rangle\ldots\big\langle P_L\big|\mathcal{U}\big|P_1\big\rangle\,, \tag{3.67}$$

where $\mathrm{d}P_l \equiv \prod_i \mathrm{d}p_{i,l}$ and the indices run over all lattice sites $i = 1,\ldots,N$ and time slices $l = 1,\ldots,L$ with periodic boundary conditions in Trotter time, such that $P_{L+1} = P_1$. The phonon coordinates x in $\mathcal{Z}_L$ can be integrated out analytically by inserting complete sets of eigenstates $\int \mathrm{d}x_l\big|x_l\big\rangle\big\langle x_l\big|$. The x_l integrals are of Gaussian form and can be easily carried out, we obtain

$$\big\langle P_l\big|\mathrm{e}^{-\Delta\tau\tilde{H}_{\mathrm{osc,x}}}\big|P_{l+1}\big\rangle = C^N \mathrm{e}^{-\frac{1}{2\omega_0\Delta\tau}\sum_i (p_{i,l}-p_{i,l+1})^2}\,, \quad \text{with} \quad C = \sqrt{\frac{2\pi}{\omega_0\Delta\tau}}\,, \tag{3.68}$$

Therefore the momentum operators p_i can be replaced by their eigenvalues $p_{i,l}$ at each site i on time slice l. With the abbreviation $\mathcal{D}p \equiv \prod_\tau \mathrm{d}p_l$ and $\sum_{\{\check{x}\}}$ denoting the sum over all auxiliary field configurations $\check{x}$ (seeEq. (3.29)) the partition function can be written as

$$\begin{aligned}\mathcal{Z} &= C^{NL}\int \mathcal{D}p\;\mathrm{e}^{-\Delta\tau S_{\mathrm{b}}}\sum_{\{\check{x}\}}\mathrm{tr}\prod_{l=1}^{L}\tilde{\mathcal{B}}_l^{\uparrow}\,\tilde{\mathcal{B}}_l^{\downarrow} \\ &= C^{NL}\int \mathcal{D}p\; w_{\mathrm{b}}[p]\sum_{\{\check{x}\}}\tilde{w}_{\mathrm{f}}[\check{x},p] \end{aligned} \tag{3.69}$$

Here we introduced the bosonic weight $w_\mathrm{b}[p] = \mathrm{e}^{-\Delta\tau S_\mathrm{b}}$. The bosonic action S_b is local in space and contains only classical variables (compare with Eq. (3.68))

$$S_\mathrm{b} = \frac{\omega_0}{2} \sum_{i,l} p_{i,l}^2 + \frac{1}{2\,\omega_0\,\Delta\tau^2} \sum_{i,l} (p_{i,l} - p_{i,l+1})^2 \; . \tag{3.70}$$

The operators $\tilde{\mathcal{B}}_l^\sigma = \mathrm{e}^{\mathrm{i}\gamma(p_i - p_j)} \mathrm{e}^{-\Delta\tau\, c_{i\sigma}^\dagger\, (\mathbf{K})_{ij} c_{j\sigma}}\, \mathrm{e}^{-\Delta\tau\, c_{i\sigma}^\dagger\, (\tilde{\mathbf{V}}_l^\sigma)_{ij} c_{j\sigma}}$ in Eq. (3.69) contain the hopping and the electronic interactions similar to the operators $\mathcal{B}_l^\sigma$ in Eq. (3.22). The matrix $\tilde{\mathbf{V}}_l^\sigma$ differs only in the chemical potential $\tilde{\mu}$ instead of μ from the definition in Eq. (3.23). The fermionic degrees of freedom can be integrated out exactly in the same way as already described in Sec. 3.3. The trace in Eq. (3.69) can be then expressed as a determinant

$$\mathrm{tr}\,(\tilde{\mathcal{B}}_1^\sigma \tilde{\mathcal{B}}_2^\sigma \ldots \tilde{\mathcal{B}}_L^\sigma) = \det\,(\mathbf{1} + \tilde{\mathbf{B}}_1^\sigma \tilde{\mathbf{B}}_2^\sigma \ldots \tilde{\mathbf{B}}_L^\sigma) \equiv \det\, \tilde{\mathbf{M}}^\sigma[\check{x}, p] \; , \tag{3.71}$$

with the matrices

$$\begin{aligned} \left(\tilde{\mathbf{B}}_l^\sigma\right)_{ij} &= \mathrm{e}^{\mathrm{i}\gamma(p_{i,l} - p_{j,l})}\, \left(\mathrm{e}^{-\Delta\tau\mathbf{K}}\right)_{ij} \left(\mathrm{e}^{-\Delta\tau\tilde{\mathbf{V}}_l^\sigma}\right)_{ij} \\ &= \mathrm{e}^{\mathrm{i}\gamma p_{i,l}}\, \left(\mathrm{e}^{-\Delta\tau\mathbf{K}}\right)_{ij} \mathrm{e}^{-\mathrm{i}\gamma p_{j,l}}\, \left(\mathrm{e}^{-\Delta\tau\tilde{\mathbf{V}}_l^\sigma}\right)_{ij} \\ \tilde{\mathbf{B}}_l^\sigma &= \mathbf{D}_l\, \boldsymbol{\kappa}\, \mathbf{D}_l^\dagger\, \boldsymbol{\upsilon}_l^\sigma \; . \end{aligned} \tag{3.72}$$

Here $\boldsymbol{\kappa}$, $\boldsymbol{\upsilon}_l^\sigma$ is the exponentiated hopping matrix $\mathrm{e}^{-\Delta\tau\mathbf{K}}$ and diagonal interaction matrix $\mathrm{e}^{-\Delta\tau\tilde{\mathbf{V}}_l^\sigma}$, respectively, l the Trotter-slice and the complex phases have been extracted into the diagonal unitary $N \times N$ matrices[7] $\mathbf{D}_l$. The fermionic weight $\tilde{w}_\mathrm{f}[\check{x}, p] = \prod_\sigma \det\, \tilde{\mathbf{M}}^\sigma[\check{x}, p]$ in Eq. (3.69) is therefore a function of the auxiliary fields and the phonon momenta.

With Eq. (3.69) we have an expression similar to the partition function for the extended Hubbard model without phonons in Eq. (3.29). The difference is the additional integral over the phonon momenta via the bosonic weight and the phase in the hopping matrix.

3.6.2 Principle components representation

What is left, is to deal with the updating of the phonon degrees of freedom. In standard approach the phonon momenta (or coordinates) are updated locally [97]. To obtain independent measurements a large number of configurations has to be skipped between

[7] Note that $(\mathbf{D}_l)_{ij} = \delta_{ij}\mathrm{e}^{\mathrm{i}\gamma p_{j,l}}$ and $\boldsymbol{\upsilon}_l$ commute since they are diagonal.

them. To overcome these autocorrelations very long QMC runs and lots of CPU-time are required.

Autocorrelations can be strongly reduced when we use the LF transformed model, as described by Hohenadler et al [43]. This is a consequence of the fact that the large displacements of the oscillators in the presence of an electron are explicitly contained in the Hamiltonian [62]. The oscillations around the potential-minimum are therefore separated from the displacement of the oscillators.

The problem of long autocorrelation times can *additionally* be eased by the simple but effective idea of a transformation to so-called *principle components*. This enables us to represent the phonon fraction of the bosonic action of Eq. (3.70) in form of the system's normal modes. The action may be written as

$$S_{\mathrm{b}} = \sum_i \mathbf{p}_i^T \mathbf{A}\, \mathbf{p}_i = \sum_i \mathbf{p}_i^T \mathbf{A}^{\frac{1}{2}}\, \mathbf{A}^{\frac{1}{2}}\, \mathbf{p}_i = \sum_i \boldsymbol{\xi}_i^T \cdot \boldsymbol{\xi}_i \tag{3.73}$$

with $\mathbf{p}_i = (p_{i,1}, \ldots, p_{i,L})$ and the principle components given by $\boldsymbol{\xi}_i = \mathbf{A}^{\frac{1}{2}}\, \mathbf{p}_i$. The matrix $\mathbf{A}$ is tridiagonal with the nonzero elements

$$A_{l,l} = \frac{\omega_0}{2} + \frac{1}{\omega_0\, \Delta\tau^2} \qquad \text{and} \qquad A_{l,l\pm1} = -\frac{1}{2\,\omega_0\, \Delta\tau^2}\ . \tag{3.74}$$

Since the trace is taken the matrix has to provide periodic boundary conditions $A_{1,L} = A_{L,1} = -1/(2\,\omega_0\,\Delta\tau^2)$ as well, so that $\mathbf{p}_{i,L+1} = \mathbf{p}_{i,1}$. Using this representation we can write the bosonic weight of the phonons as

$$w_{\mathrm{b}} = \exp\left(-\Delta\tau \sum_i \boldsymbol{\xi}_i^T \cdot \boldsymbol{\xi}_i\right)\ , \tag{3.75}$$

which is in fact a simple Gaussian form with the standard deviation $\sigma_{ph} = \sqrt{1/(2\Delta\tau)}$. This leads to the conclusion that the QMC can now be performed directly in terms of the new variables $\boldsymbol{\xi}$ that can easily be generated as samples of a Gaussian distribution via the Box-Müller method [96]. The matrix $\mathbf{A}^{\frac{1}{2}}$ mediates between the principle components and the phonon momenta $\mathbf{p}_i$ to calculate the Green's function.

In the simulation we sample a new set of variables $\boldsymbol{\xi}$ according to a Gaussian distribution with standard deviation σ_{ph}. This corresponds to a change of all phonon coordinates $\mathbf{p}_i$ at all time slices, thus the updating lost its local character in imaginary time. The new phonon configuration is then accepted or declined in a Metropolis decision Eq. (3.54). Between the phonon updates a reasonable number of auxiliary field configurations are sampled via local updates. The computational effort of a new configuration proposal for the phonon momenta $p_{i,j}$ is of the same order as a lattice sweep, since it is necessary to compute the Green's function and its weight in Eq. (3.37) from scratch.

In the representation of $\boldsymbol{\xi}$ variables we are able to sample weakly autocorrelated phonon momenta configurations. The acceptance-rate of correspondingly sampled configurations can be increased at the cost of longer autocorrelation times by sampling the $\boldsymbol{\xi}$s no longer in the systems's normal modes (full range of the Gaussian distribution with variance σ_{ph}), but as small changes with respect to their last values.

3.6.3 Changes in the code

The changes in the Hamiltonian due the LF transformation concern the observables and the updating in the MC-process, now that we deal with a complex action.

The formal description of the DetQMC method does not change when we use complex matrices instead of real ones. In the program code all functions and variables involved in the construction and updating of the Green's function (Eq. (3.37)) have to be changed to complex data type. Note that the matrix-transpositions needed in the SVD-decomposition (see Sec. 3.7) have to be extended by complex conjugations since the algorithm now runs with complex matrices. The phase has to be included in the routines calculating the matrix products of the propagator-matrices $\tilde{\mathbf{B}}$ and the couplings have to be renormalized according to Eq. (2.29). This implies the need of an auxiliary field even in the case of initial $U = 0$.

As we are now running the simulation of the transformed Hamiltonian, the observables have to be transformed as well. Our main-quantity the Green's function transforms with the definition in Eq. (2.14) to

$$\left\langle c^\dagger_{i\sigma}\, c_{j\sigma} \right\rangle \to \left\langle \tilde{c}^\dagger_{i\sigma}\, \tilde{c}_{j\sigma} \right\rangle = \left\langle c^\dagger_{i\sigma}\, \mathrm{e}^{\mathrm{i}\gamma p_i} c_{j\sigma}\, \mathrm{e}^{-\mathrm{i}\gamma p_j} \right\rangle \tag{3.76}$$

such that we have to apply the phase of the current time-slice to the Green's function before we measure our observables. For the imaginary time correlators, pairs of phases corresponding to the time-slices have to be applied. Since most observables are derived from the Green's function their implementation remains unchanged, solely the total energy has to be adapted by including the phonon degrees of freedom – the measurement of observables is described in chapter 4.

Of course, $\tilde{H}^\mu$ is Hermitian $\tilde{H}^\mu = (\tilde{H}^\mu)^\dagger$ such that the MC-estimators, e.g.,

$$\left\langle O \right\rangle = \frac{1}{\mathcal{Z}_L} \sum_{\check{x},p} \tilde{w}_{\mathrm{f}}[\check{x},p]\; \tilde{w}_{\mathrm{b}}[p]\; \tilde{O}(\check{x},p)\;, \tag{3.77}$$

are real quantities

$$\left\langle \tilde{\Psi} \middle| \tilde{O} \middle| \tilde{\Psi} \right\rangle = \left\langle \Psi \middle| U^\dagger\, UOU^\dagger\, U \middle| \Psi \right\rangle \in \mathbb{R}\;, \tag{3.78}$$

where U denotes the unitary operator introduced with the LF-transformation in Eq. (2.10). Though, this statement does not necessarily hold for a single configuration of phonon

momenta but after integration over the whole phase space. Therefore one has to include the weights in the observables and needs to keep track of them in the analysis.

3.6.4 Complex Hubbard-Stratonovich transformation

Accordingly, we are now forced to compute with complex values, which increases the computation time for all operations and functions by a factor ~ 3. We can exploit this handicap by using a different Hubbard-Stratonovich transformation. Instead of taking the real valued (positive) solution of the free parameter λ in Eq. (3.20) we choose to take the negative solution of the square-root

$$\exp\left(-\Delta\tau\tilde{U}n_{i\uparrow}n_{i\downarrow}\right) = \frac{1}{2}\sum_{\alpha_i=\pm 1}\exp\left(2\,\mathrm{i}\,\lambda_{\tilde{U}}\,\alpha_i\,(n_{i\uparrow}+n_{i\downarrow}) - \frac{1}{2}\Delta\tau\tilde{U}\,(n_{i\uparrow}+n_{i\downarrow})\right)\ , \quad (3.79)$$

where

$$\begin{aligned}\cos(\lambda_{\tilde{U}}) &= \mathrm{e}^{-\frac{1}{2}\Delta\tau\tilde{U}} \\ \mathrm{i}\,\lambda_{\tilde{U}} = \mathrm{i}\arccos\left(\mathrm{e}^{-\frac{1}{2}\Delta\tau\tilde{U}}\right) &= 2\,\mathrm{arctanh}\left(\sqrt{-\tanh\left(\Delta\tau\tilde{U}/4\right)}\right)\ . \end{aligned} \quad (3.80)$$

As already mentioned, for this choice of the Hubbard-Stratonovich transformation, $SU(2)$ spin invariance is retained for any given auxiliary-field configuration [98] for the repulsive Hubbard model ($\tilde{U} > 0$). The auxiliary fields no longer couple to the spin but to the local density – thus spin dependent observables (and other quantities which do not commute with the z-component of the spin) are stabilized. In case of the $SU(2)$-invariant algorithm, one has

$$\left\langle c^\dagger_{i\uparrow}c_{j\uparrow}\right\rangle = \left\langle c^\dagger_{i\downarrow}c_{j\downarrow}\right\rangle \quad (3.81)$$

for all pairs of i, j and for all times τ. Thus the total magnetization is identical to zero for all configurations of the HS-fields

As discussed by Assaad [98] spin-dependent imaginary time displaced Green's functions (multi-point correlators) profit from this choice of HS-transformation. Fig. 3.2 shows the spin-spin correlation function $\left\langle S(\mathbf{Q},\tau)\,S(-\mathbf{Q},0)\right\rangle$, with $\mathbf{Q} = (\pi,\pi)$ for a square Hubbard model with and without $SU(2)$ invariant code. Here also the result for a Green's function coupled to the z-component of the spin only and the relative errors of the two coding variants are given, which remain stable for all values of τ. The computation time for both versions was held equal by carrying out more than twice as many sweeps for the $SU(2)$ non-invariant code. Assaad also showed for an extra auxiliary fields (e.g. an additional pairing term) which hampers a fully spin-symmetric simulation additionally, that the $SU(2)$ invariant code performs even better.

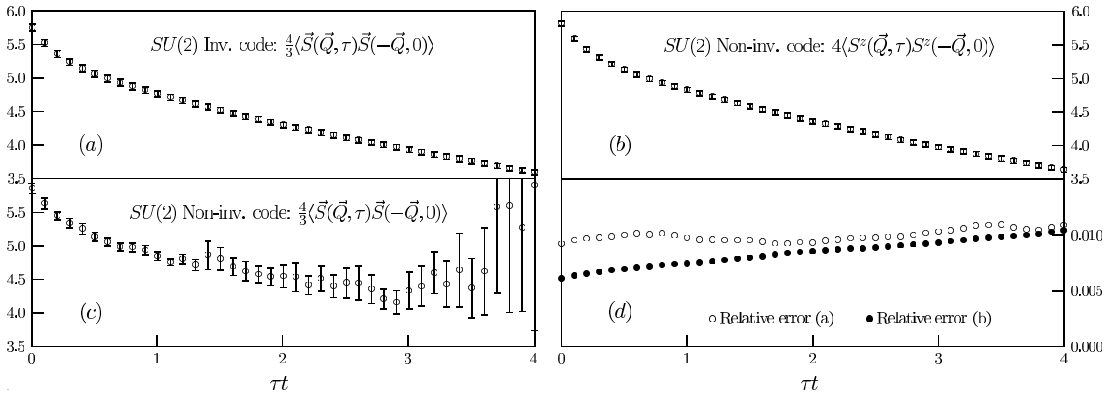

Fig. 3.2: Imaginary time displaced spin-spin correlations at $\mathbf{Q} = (\pi, \pi)$ of a 6×6 Hubbard model with $U/t = 4$ at half-filling and zero temperature taken from Ref. [98]. Compare the graphs on the lhs for the difference of the $SU(2)$ invariant HS-transformation. The rhs shows the Green's function of the non-invariant code coupled to the z-component of the spin only and the relative errors of (a) and (b) - for equal computation time the non-invariant code gives slightly better converged results for small distances in imaginary time.

The physical interpretation of a spin-flip in the auxiliary fields here changed to the creation (annihilation) of electrons at a space-time site. The balance of the equal number of up- and down-spins is given for all times and the fluctuations of the auxiliary fields now affect the noise in the filling of the system. Although this can be seen as a disadvantage, it does not severely hamper convergence of density-dependent observables.

3.7 Stabilizing the computation

Within the procedure to obtain the Green's function, the evaluation of the product of several matrices $\tilde{\mathbf{B}}_l^\sigma$ is necessary. Sometimes these matrices are numerically ill-conditioned in sense of the ratio of the largest singular value of the matrix to the smallest one. This ratio represents an upper bound to be amplification of errors in matrix multiplications.In calculating the Slater determinants in Eq. (3.28), one computes small differences of large matrix elements. These differences are very inaccurate, dominated by the noise in the least significant bits of the matrix elements due to their finite numerical representation. This problem becomes more serious as the number of time-slices is increased to obtain simulations at low temperatures. Simulations neglecting this fact ultimately fail because of these awkward scale-features.

The singular value decomposition (SVD) technique allows to deal with those matrices based on the Gram-Schmidt orthogonalization of linear algebra [96]. The product of m

matrices can be expressed (spin indices are dropped for simplicity) as

$$\mathbf{M} = \tilde{\mathbf{B}}^m \, \tilde{\mathbf{B}}^{m-1} \ldots \tilde{\mathbf{B}}^1 = \mathbf{UDV} \; , \tag{3.82}$$

where $\mathbf{U}$ is a well conditioned orthonormal, $\mathbf{D}$ is a diagonal matrix with a wide spectrum of values and $\mathbf{V}$ is an upper triangular matrix. Using the fact that $\mathbf{U}$ and $\mathbf{V}$ are sufficiently well-conditioned, we can multiply them by other matrices without compromising the accuracy. Decomposing the ill conditioned matrices this way, only the diagonal matrix contains the numerically problematic values. In order to understand what we gain of this factorization, consider the schematic matrix product

$$\begin{aligned} \mathbf{M} = \mathbf{UDV} &= \begin{pmatrix} \mathrm{X} & \mathrm{X} & \mathrm{X} & \mathrm{X} \\ \mathrm{X} & \mathrm{X} & \mathrm{X} & \mathrm{X} \\ \mathrm{X} & \mathrm{X} & \mathrm{X} & \mathrm{X} \\ \mathrm{X} & \mathrm{X} & \mathrm{X} & \mathrm{X} \end{pmatrix} \cdot \begin{pmatrix} \mathrm{X} & & & \\ & \mathrm{X} & & \\ & & \mathrm{X} & \\ & & & \mathrm{x} \end{pmatrix} \cdot \begin{pmatrix} \mathrm{X} & \mathrm{X} & \mathrm{X} & \mathrm{X} \\ & \mathrm{X} & \mathrm{X} & \mathrm{X} \\ & & \mathrm{X} & \mathrm{X} \\ & & & \mathrm{X} \end{pmatrix} \\ &= \begin{pmatrix} \mathrm{X} & \mathrm{X} & \mathrm{X} & \mathrm{X} \\ \mathrm{X} & \mathrm{X} & \mathrm{X} & \mathrm{X} \\ \mathrm{X} & \mathrm{X} & \mathrm{X} & \mathrm{X} \\ \mathrm{X} & \mathrm{X} & \mathrm{X} & \mathrm{X} \end{pmatrix} . \end{aligned}$$

Here, the product is essentially the outer product of the first column of $\mathbf{U}$ and the first row of $\mathbf{V}$ at the order of the largest scale in $\mathbf{D}$. The different scales now exist implicitly as very small differences of large matrix elements. As example for a sufficiently well conditioned matrix product consider a matrix $\mathbf{W}$ where its small scales are explicitly given in its columns. We decompose into $\mathbf{W} = \mathbf{UDV}$ such that we can write the *stable* product to illustrate the difference:

$$\begin{aligned} \mathbf{U}^{-1}\mathbf{W}\mathbf{V}^{-1} &= \begin{pmatrix} \mathrm{X} & \mathrm{X} & \mathrm{X} & \mathrm{X} \\ \mathrm{X} & \mathrm{X} & \mathrm{X} & \mathrm{X} \\ \mathrm{X} & \mathrm{X} & \mathrm{X} & \mathrm{X} \\ \mathrm{X} & \mathrm{X} & \mathrm{X} & \mathrm{X} \end{pmatrix} \cdot \begin{pmatrix} \mathrm{X} & \mathrm{X} & \mathrm{X} & \mathrm{x} \\ \mathrm{X} & \mathrm{X} & \mathrm{X} & \mathrm{x} \\ \mathrm{X} & \mathrm{X} & \mathrm{X} & \mathrm{x} \\ \mathrm{X} & \mathrm{X} & \mathrm{X} & \mathrm{x} \end{pmatrix} \cdot \begin{pmatrix} \mathrm{X} & \mathrm{X} & \mathrm{X} & \mathrm{X} \\ & \mathrm{X} & \mathrm{X} & \mathrm{X} \\ & & \mathrm{X} & \mathrm{X} \\ & & & \mathrm{X} \end{pmatrix} \\ &= \begin{pmatrix} \mathrm{X} & & & \\ & \mathrm{X} & & \\ & & \mathrm{X} & \\ & & & \mathrm{x} \end{pmatrix} = \mathbf{D} \; . \end{aligned}$$

Obviously, multiplication on the left of $\mathbf{W}$ is stable – combining elements of the same scale. Multiplication on the right by $\mathbf{V}^{-1}$ mixes different scales but can be kept stable by appropriate down-scaling. This factorization conserves all information without compromising accuracy (too much).

In practice, to get the product of $\tilde{\mathbf{B}}$-matrices from time-slice l to $l+1$ we write according to Loh and Gubernatis [82]

$$\begin{aligned}
\tilde{\mathbf{B}}_{l+1}\tilde{\mathbf{B}}_l \dots \tilde{\mathbf{B}}_1 &= \tilde{\mathbf{B}}_{l+1}\,\mathbf{UDV} = (\tilde{\mathbf{B}}_{l+1}\,\mathbf{UD})\mathbf{V} \\
&= \left(\tilde{\mathbf{B}}_{l+1}\,\mathbf{U}\begin{pmatrix} \mathrm{X} & & & \\ & \mathrm{X} & & \\ & & \mathrm{X} & \\ & & & \mathrm{x} \end{pmatrix}\right)\mathbf{V} = \begin{pmatrix} \mathrm{X} & \mathrm{X} & \mathrm{X} & \mathrm{x} \\ \mathrm{X} & \mathrm{X} & \mathrm{X} & \mathrm{x} \\ \mathrm{X} & \mathrm{X} & \mathrm{X} & \mathrm{x} \\ \mathrm{X} & \mathrm{X} & \mathrm{X} & \mathrm{x} \end{pmatrix}\mathbf{V} \\
&= (\mathbf{U}'\mathbf{D}'\mathbf{V}')\mathbf{V} = \mathbf{U}'\mathbf{D}'(\mathbf{V}'\mathbf{V})\,,
\end{aligned}$$

which is the decomposition of the new partial product $\tilde{\mathbf{B}}_{l+1}\tilde{\mathbf{B}}_l \dots \tilde{\mathbf{B}}_1$. With this technique the safe inversion to obtain the Green's (Eq. (3.37)) function is given by

$$\begin{aligned}
\mathbf{G}^\sigma(\tau_l,\tau_l) &= (\mathbf{1} + \tilde{\mathbf{B}}_l \dots \tilde{\mathbf{B}}_1\tilde{\mathbf{B}}_L \dots \tilde{\mathbf{B}}_{l+1})^{-1} \\
&= (\mathbf{1} + \mathbf{UDV})^{-1} \\
&= \mathbf{V}^{-1}\,\underbrace{\left(\mathbf{U}^{-1}\mathbf{V}^{-1} + \mathbf{D}^{-1}\right)^{-1}}_{\text{decompose to } (\mathbf{U}'\ \mathbf{D}'\ \mathbf{V}')^{-1}}\,\mathbf{U}^{-1} \\
&= \mathbf{V}^{-1}\left(\mathbf{U}'\mathbf{D}'\mathbf{V}'\right)^{-1}\mathbf{U}^{-1} \\
&= \left(\mathbf{V}'\mathbf{V}\right)^{-1}\mathbf{D}'^{-1}\left(\mathbf{U}\mathbf{U}'\right)^{-1}\,. \qquad (3.83)
\end{aligned}$$

Here, we isolate the divergent scales into $\mathbf{D}$ and invert the individual pieces. Elements of different scales are separated until the last step. There they are combined which cuts off the divergent scales and information definitely gets lost. Nevertheless, this does not severely compromise the accuracy of the computation of the the Green's function. In the decomposition of the single-particle propagator the matrices $\mathbf{U}$ and $\mathbf{V}$ contain the information for the states for a given HS-field configuration. The scales of these states are explicitly contained in $\mathbf{D}$. Overwriting of divergent scales in $\mathbf{D}$ by numerically representable numbers does not erase the information of which scales are *small* or *large*. Thus, this computation does not induce any significant error into the computations of the Green's function.

The effort of stabilizing the construction of the Green's function is proportional to the number of the time-slices L. Since the number of decompositions one must perform in each reconstruction increases with L as well, the computational overhead scales as L^2. Storing SVD-factorized matrix products at recurrent check-points within the simulation saves computer-time. A helpful approach is to sweep back and forth through the lattice from time-slice $1 \dots L$ and back again from $L \dots 1$, enables one to save SVD-factorized matrix products of the actual configuration on the fly which are needed for the return trip. Instead of re-evaluating Eq. (3.83) for different times τ_l we can compute the Green's

function from the stored SVD-decompositions of two partial products. We define the partial product from the right and left hand side as

$$\tilde{\mathbf{B}}_l \dots \tilde{\mathbf{B}}_1 = \mathbf{U}_\mathrm{R}\mathbf{D}_\mathrm{R}\mathbf{V}_\mathrm{R} \;, \qquad \text{and} \qquad \tilde{\mathbf{B}}_L \dots \tilde{\mathbf{B}}_{l+1} = \mathbf{V}_\mathrm{L}\mathbf{D}_\mathrm{L}\mathbf{U}_\mathrm{L} \;. \tag{3.84}$$

We can now compute the Green's function from Eq. (3.37) on time-slice l by expanding with $\mathbf{U}_\mathrm{L}\mathbf{U}_\mathrm{L}^{-1}$ and $\mathbf{U}_\mathrm{R}^{-1}\mathbf{U}_\mathrm{L}$

$$\begin{aligned} \mathbf{G}^\sigma(\tau_l,\tau_l) &= (\mathbf{1} + \mathbf{U}_\mathrm{R}\mathbf{D}_\mathrm{R}\mathbf{V}_\mathrm{R}\mathbf{V}_\mathrm{L}\mathbf{D}_\mathrm{L}\mathbf{U}_\mathrm{L})^{-1} \\ &= \mathbf{U}_\mathrm{L}^{-1}\left(\mathbf{U}_\mathrm{R}^{-1}\mathbf{U}_\mathrm{L}^{-1} + \mathbf{D}_\mathrm{R}\mathbf{V}_\mathrm{R}\mathbf{V}_\mathrm{L}\mathbf{D}_\mathrm{L}\right)\mathbf{U}_\mathrm{R}^{-1} \;. \end{aligned} \tag{3.85}$$

Similar to Eq. (3.83) the inverse of the ill-conditioned sum can be obtained by further decomposition and inverting the individual pieces. This reduces the stabilization overhead to scale only with L.

The partial products in Eq. (3.84) should be stored every few (≈ 8, depending on your set of parameters) time-slices. The memory necessary to store the partial products is bearably small.

3.8 Checkerboard breakup

A good spot to reduce computation time is in optimizing matrix operations. The exchange operator $\mathrm{e}^{-\Delta\tau\mathbf{K}}$ is a densely occupied matrix. A default matrix product produces costs of $\mathcal{O}(N^3)$. It can be reduced to $\mathcal{O}(N^2)$ by applying the Suzuki-Trotter decomposition one more time

$$\mathrm{e}^{\Delta\tau\,\mathbf{K}} = \mathrm{e}^{\Delta\tau\,\sum_{<ij>} t_{ij} c_{i\sigma}^\dagger c_{j\sigma}} \approx \prod_{<ij>} \mathrm{e}^{\Delta\tau\, t'_{ij} c_{i\sigma}^\dagger c_{j\sigma}} \;, \tag{3.86}$$

with the sum over all pairs of lattice sites connected via the transfer $t'_{ij} \neq 0$. This can be viewed as the product of the exponential of an $N \times N$-matrix $\mathbf{t}'$ containing solely two nonzero elements t'_{ij}, t'_{ji} with $t'_{ji} = {t'_{ij}}^*$. The Trotter-approximated fermionic

contribution to the partition function is now given by

$$\exp(\Delta\tau\mathbf{K}) \approx \prod_{<ij>} \exp\ \Delta\tau \begin{pmatrix} 0 & \cdots & 0 & \cdots & 0 & \cdots & 0 \\ \vdots & & \vdots & & \vdots & & \vdots \\ 0 & \cdots & 0 & \cdots & t'_{ij} & \cdots & 0 \\ \vdots & & \vdots & & \vdots & & \vdots \\ 0 & \cdots & {t'_{ij}}^* & \cdots & 0 & \cdots & 0 \\ \vdots & & \vdots & & \vdots & & \vdots \\ 0 & \cdots & 0 & \cdots & 0 & \cdots & 0 \end{pmatrix}$$

$$= \prod_{<ij>} \begin{pmatrix} 1 & \cdots & 0 & \cdots & 0 & \cdots & S \\ \vdots & \ddots & \vdots & & \vdots & & \vdots \\ 0 & \cdots & C & \cdots & S & \cdots & 0 \\ \vdots & & \vdots & \ddots & \vdots & & \vdots \\ 0 & \cdots & S^* & \cdots & C & \cdots & 0 \\ \vdots & & \vdots & & \vdots & \ddots & \vdots \\ S^* & \cdots & 0 & \cdots & 0 & \cdots & 1 \end{pmatrix}, \tag{3.87}$$

with $C = \cosh(\Delta\tau\|t'_{ij}\|)$ and $S = \frac{t'_{ij}}{\|t'_{ij}\|}\sinh(\Delta\tau\|t'_{ij}\|)$ on the diagonals. This matrix manipulation is called *Checkerboard-breakup* [99]. The error of this additional Suzuki-Trotter transformation is small compared to the systematic error of the Hamiltonian decomposition – as shown by Endres in [84], its influence on the results is negligible. While the exact treatment of the hopping term leaves the Hamiltonian Eq. (2.7) symmetric under particle-hole transformation at half-filling, this symmetry is no longer conserved using the Checkerboard-breakup-approximation [43]. This is because of the additional Suzuki-Trotter error in the approximation of the kinetic matrix. This way, half-filling $n = 1.0$ is no longer obtained by setting $\mu = -E_{\mathrm{P}} + U/2 - N_{\mathrm{nn}}V$, but has to be slightly adjusted to different values.

Alternatively, for uniform transfer integrals, one may utilize Fast-Fourier-Transformations in order to apply the kinetic-energy factor $\mathrm{e}^{\Delta\tau\mathbf{K}}$ in momentum space, in which $\mathbf{K}$ is diagonal.

3.9 Improving convergence

Since consecutive auxiliary field configurations differ only in small amounts because of the local updates described in Sec. 3.5 their autocorrelation time as a measure of dependence is fairly high. To obtain independent measurements one is therefore forced to skip a large number of local updates between them.

One way to overcome this problem is to profit from global updates, which are usually difficult to construct due to the nontrivial correlations of the degrees of freedom. Other ways to enhance the sampling in the Monte Carlo process are tempering and reweighting.

Parallel Tempering is based on sampling configurations for different couplings simultaneously, Simulated Tempering and reweighting methods like the Multi-canonical Monte Carlo alter the sample weights. These methods aim to allow the Markov-chain to move faster in phase space (circumnavigating improbable regions) than it is possible with conventional moves. Therefore observables converge faster.

In this work we choose a combination of the nonlocal moves and tempering in the inter-site coupling.

3.9.1 Global updates

Like the LF transformation depicted in Sec. 2.9 and Sec. 3.6 is used to obtain a representation of the phonon momenta in orthogonal space to sample new low correlated phonon configurations, an improved updating scheme for the auxiliary field configurations enhances the Monte Carlo procedure. It is necessary to identify physically the collective (slow and nonlocal) modes of the system, and to devise an efficient computational algorithm for speeding up those modes. Unfortunately these two goals are in conflict; it is very difficult to devise global-move algorithms that are nonlocal enough that their computational cost outweighs the reduction of slowing down. Cluster algorithms used in classical models (Wolff–, Swendsen-Wang algorithm) cannot be applied to the DetQMC because of the nonlocal determinant weight.

So far we introduced a single spin-flip update for the Ising fields of the Hubbard and the extended Hubbard interaction in Sec. 3.5. As shown by Scalettar and others [100], for the bare Hubbard model the configuration space (at real-valued HS-transformation) shows two extrema separated by an intersection growing with the repulsive coupling U illustrated in Fig. 3.3. The intersection covers the bulk of improbable configurations. Note that this is only visible in the approximation of the strong coupling $U \gg t$ limit. This approach becomes rigorously correct only for large U/t, though it definitely illustrates the problem.

For large βU and half-filling the auxiliary field configuration $\Sigma = \sum_i \alpha(i,l)$ with all Ising spins up (down) can be assigned to $n_\uparrow \approx 1$ ($n_\downarrow \approx 1$), the intersection with $n_\uparrow = n_\downarrow = 1/2$,. For example to get from configuration $\alpha(i,l) = +1$ to configuration $\alpha(i,l) = -1$ for the site i at all l-time-slices is very improbable. In this case it is unlikely that the observables will converge using only single spin-flip moves since the simulation time is limited. Observables depending on symmetric sampling of these configurations would not converge satisfactorily. Naturally, if ergodicity is violated so badly, other

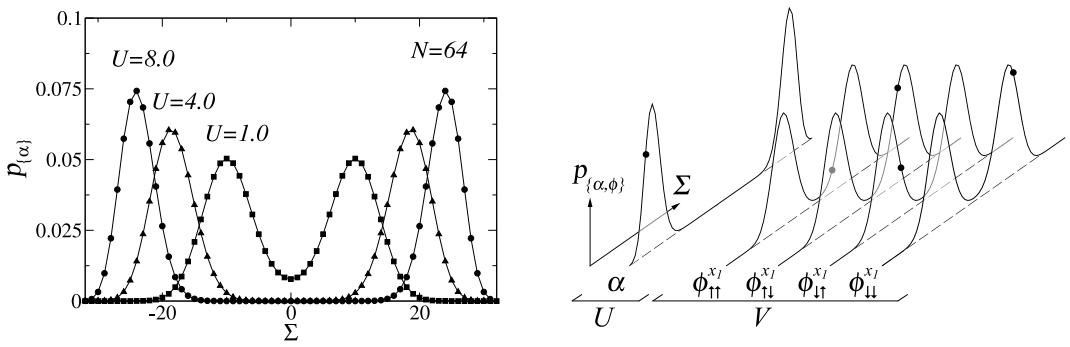

Fig. 3.3: Left: The probability of auxiliary field configurations in the strong coupling limit $t = 0$ for values of $U = 1.0$ (squares), $U = 4.0$ (triangles) and $U = 8.0$ (circles) illustrating the tunneling barrier. Lines are guide to the eye only. Right: Schematic illustration of the phase space for a specific configuration indicated by the black dots

correlation functions are unlikely to be obtained correctly either.

Scalettar and others [100] introduced a nonlocal update by flipping the spin at a site $\alpha(i,l)' = -\alpha(i,l)$ for all time-slices l and obtained impressive improvements. Such a move has the interpretation of flipping a spin in the large-U Heisenberg limit of the Hubbard model. For the extended Hubbard model in real representation Zacher demonstrated that naive application of the Scalettar-move to the inter-site coupling fields shows no advantages since the acceptance rate drops to zero – especially near half-filling [34]. As a result of the Hubbard-Stratonovich transformation the nearest neighbor Coulomb interaction is realized by four Ising-fields per dimension. Zacher proposed additionally to the Scalettar-move to swap the fields coupled to an *up*-spin with those of a *down*-spin for fixed i and all time-slices l

$$\begin{aligned} \phi^{x_i}_{\uparrow\uparrow}(l,i)' &\rightarrow \phi^{x_i}_{\downarrow\uparrow}(l,i)\,, & \phi^{x_i}_{\downarrow\uparrow}(l,i)' &\rightarrow \phi^{x_i}_{\uparrow\uparrow}(l,i)\,, \\ \phi^{x_i}_{\uparrow\downarrow}(l,i)' &\rightarrow \phi^{x_i}_{\downarrow\downarrow}(l,i)\,, & \phi^{x_i}_{\downarrow\downarrow}(l,i)' &\rightarrow \phi^{x_i}_{\uparrow\downarrow}(l,i)\,. \end{aligned} \tag{3.88}$$

Depending on the filling and the couplings of the system one can try to give the HS-field configurations a physical interpretation. For example, at a filling of 1/8-th with onsite and inter-site coupling the electrons are probably delocalized to more than one site. Thus, if one wants to flip the spin of an electron the proposed move from Eq. (3.88) should be applied to four neighboring sites and to the onsite field simultaneously.

A reliable indicator for ergodicity in the repulsive Hubbard models with real-valued HS-transformation is the over-all spin $\langle S_z \rangle = (n_\uparrow - n_\downarrow)/2$. As a consequence of the symmetry provided by the model, the grand-canonical expectation value is zero. In non-ergodic simulations at large couplings one obtains values like $\langle n_\uparrow \rangle = 9 \pm 0.000002$

and $\langle n_\downarrow \rangle = 7 \pm 0.000002$ [100]. It is obvious that the simulation is stuck in a small area of configuration space – the problem is therefore called *sticking-problem*. Tracking the estimators in Monte Carlo time their expectation values are stuck as well, instead of showing a Gaussian deviated accumulation around the correct mean value.

For the parameters of the sodium vanadate, the Scalettar-move greatly improves the convergence of $\langle S_z \rangle$ with acceptance rates of approximately 8–12% (depending on the system size). The Zacher-move is hardly ever accepted and contributes only negligibly to the convergence.

As already said in Sec. 3.6.4, this indicator for ergodicity is replaced by the accumulation of the imaginary part of the Green's function to zero in the case of the SU(2)-invariant HS-transformation. With the complex solution of the HS-transformation the probability-distribution of the auxiliary field configurations changes to an oscillating form around $\Sigma = 0$ in Gaussian shape, while the condition $\langle S_z \rangle = 0$ is always fulfilled in the simulation. Nonetheless, any global move is of help, enhancing the movement of the Markov-chain.

3.9.2 Parallelization

For large system sizes the use for large scale computing is inevitable and the need for parallelization is evident. The simulation is perfectly suited for trivial parallelization, where several simulations with the same set of parameters but different random-seeds can be run in parallel without any communication in between and their output can be easily combined within the Jackknife analysis (Sec. 4.3).

3.9.3 Tempering

Having the situation of parallel running processes suggest itself to implement Parallel Tempering, a modification of Simulated Tempering [101, 102, 103]. In this procedure a number of simulations run simultaneously with slightly different parameters (e.g. couplings for the auxiliary fields). Frequently, after passing several thousand updates the processes exchange their current auxiliary field configurations in form of a detailed balance Metropolis decision. That way, the systems remain in equilibrium and canonical expectation values are calculated unchanged without the need of reweighting.

The tempering procedure is possible in any parameter of the system, although just for few ones it really pays off. For our simulation, the tempering in the extended Hubbard coupling V seems to be the best choice. One obtains results for a wide range of the coupling without producing unneeded data. Tempering in the on-site coupling U would enhance the sampling of the (for large U) separated configuration space, however,

we are not interested in different values for the Hubbard interactions, since this is a fixed parameter for sodium vanadate. Additionally to the tempering in V, one can try global updates of the onsite-interaction auxiliary fields as one swaps the configurations of different processes which all run at the same value for U.

The range of our tempering-parameter V should include the charge ordered phase as well as the disordered phase of the system to provide efficient sampling. Then we estimate the number of different couplings required in the range as follows. In order that each process wanders over the whole coupling region, the acceptance probabilities of the exchange process should be in the vicinity of one and approximately constant. While in classical systems this number can be estimated via the Boltzmann weight [101], the dependence of the auxiliary fields to the configuration weights in DetQMC are nontrivial. Nonetheless the intervals can be estimate via the transition of the order parameter as a function of V or the overlap of the distributions via the Kullback-Leibler number. To allow nearly constant acceptance ratios the intervals have to become more dense as they approach the critical point.

The necessary conditions for effective tempering can be seen as:

(i) The exchange in both directions is realized with a non-negligible probability for all adjacent pairs of processes;

(ii) Each process moves around the whole coupling range in reasonable simulation time;

(iii) By wandering in the coupling, the system forgets where it was trapped.

In this simulation the communication is realized via the MPI-libraries [104] in master-slave topology. The jobs run independently several hundred sweeps and report in at the controlling master process. The master collects the probability weights of the current auxiliary field configurations w_i and computes the probability of an exchange of the auxiliary fields between adjacent (in the sense of their couplings V_i) processes i and $i+1$ according to [105] via

$$P_{\text{swap}}(V_i, V_{i+1}) = \min\left[1, \frac{w_i(V_{i+1})\, w_{i+1}(V_i)}{w_i(V_i)\, w_{i+1}(V_{i+1})}\right] . \tag{3.89}$$

If the swap is accepted the auxiliary field configurations are exchanged and the processes resume their computation independently and are then reporting in again. The data-amount sent in this communication is small and can be processed very fast. The exchange could also be done via point-to-point communication between the processes without a master.

3.10 Outline of the algorithm

In this chapter we gave a detailed introduction into BSS-style determinant (or auxiliary field) QMC. The Suzuki-Trotter decomposition of the Hamiltonian enabled us to define the problem in a path integral formalism. Via the Hubbard-Stratonovich transformation we were able to linearize the quadratic interaction of the Hubbard-term by introducing auxiliary fields over which one has to integrate. This high-dimensional integral can be evaluated by means of MC-sampling. In the BSS-style QMC the MC-configurations can be efficiently generated by a single spin-flip algorithm, which can be improved by global updates, tempering, or different types of the Hubbard-Stratonovich transformation.

We discussed the changes in the algorithm, necessary to extend the Hamiltonian by Einstein-phonons with Holstein coupling. Preparing the Hamiltonian with the LF transformation allows highly efficient sampling of the phonon degrees of freedom. It can be additionally enhanced as one samples the phonon configurations in the system's normal modes. Technical details on how to speed up matrix products and how to deal with numerical instabilities prepared us to combine all these methods in our simulation.

Running once through all lattice sites in space and time and trying to update the corresponding Ising-spins is called a sweep. By decreasing the temperature (or coupling-strength) stepwise the auxiliary fields are equilibrated before starting the measurement. As a rule of thumb one can, e.g., run a large number of multiple of the integrated autocorrelation time for warmup sweeps, or drop the first ten percent of the collected data of the simulation. Another method is to observe an observable to determine when the transient region in the beginning ends. Both methods should be sufficient, but one can never be sure not to be trapped in a meta-stable phase space region. The measurements are taken after skipping enough sweeps in between to obtain low-correlated time series. The overall QMC-algorithm is described in some pseudo-code:

```
INIT - Initialize all fields to arbitrary (e.g.  randomly chosen) spin-alignment;
    calculate the Green's function for the first time-slice given in Eq. (3.37);
    prepare runtime environment for all nodes involved in the tempering process

DO I=1,WARM+MEAS*SKIP
    IF (I <= WARM) THEN
        TEMPERPARAMS - Adjust all couplings slowly with increasing I so that
            sufficient sweeping at final coupling strength is guaranteed
    END IF
    SWEEP - run trough all lattice sites and for all time slices; update Ising
        spins according to the probability in Eq. (3.54); calculate the new
        Green's function as defined in Eq. (3.58)
    IF time to stabilize THEN
        IF time for global move THEN
```

```
            UPDATE PHONONS - propose new phonon configuration; sample new
                Gaussian distributed momenta according to Eq. (3.75)
            TEMPER - swap HS-fields with other processes via MPI as described
                in Sec. 3.9.3
            CLUSTER FLIPS - propose new HS-field configuration according to
                the description in Sec. 3.9.1
        END IF
        GFSCRATCH - calculate the Green's function from the scratch via
            SVD-decomposition as given in Eq. (3.37)
    END IF
    IF (I > WARM && MOD(I-WARM,SKIP) == 0) THEN
        MEASURE - calculate observables from current configuration
    END IF
END DO
```

From the data output, averages and errors of the observables will be calculated via the Jackknife method. The analytic continuation of the imaginary time data is done by the Maximum Entropy method. Both will be discussed in the following sections.

3.11 DetQMC compared to other methods

Usually we want: large system sizes, a huge number of particles, scan through a wide range of parameters, observables of any kind and complexity, my personal supercomputer for home, world peace, ... – apart from the last two the DetQMC-method can provide a good bunch of them. The most important feature for this work is the ability to calculate dynamic quantities, although via the detour of Maximum Entropy described in Sec. 4.4. However, there are restrictions as already described, like the sign- or phase problem from Sec. 4.2 which restricts the size and temperature of the system, numerical instabilities like in Sec. 3.7 and strong autocorrelations depict in Sec. 3.9 and Sec. 4.3.

Alternative numerical methods exhibit excellent properties but are not as flexible as QMC is. Exact diagonalization (ED) techniques like the Lanczos method can perform zero- as well as finite temperature calculations [106], produce static observables and dynamical spectra – and that (as labeled) almost exactly. Unfortunately the diagonalization requires huge amounts of memory which restricts system size and parameter range leading to undesirable finite size effects. Cluster perturbation theory (CPT) utilizing ED (CPT must not be necessarily incorporate ED) suffers from similar problems, since cluster sizes are small and additionally the decoupling into clusters breaks translational invariance. At present no method is known to measure multi-point-correlations in CPT and dynamical spectra are limited to the one-particle Green's function.

Density matrix renormalization group (DMRG) is a variational diagonalization method where larger systems than in ED can be treated. In principal dynamical spectra can be

calculated with DMRG – the drawback is that the computation would exceed the effort using QMC by far. Since DMRG is based on a variational Ansatz the results do not necessarily lead to the exact eigenstates. This is due to the specific construction of the system-block, where the system may get stuck. The effects of boundary conditions are a delicate subject in DMRG as well.

Another non-perturbative approach is the dynamical mean field theory (DMFT) based on a self-consistency loop with a system-solver (e.g. QMC, ED). While DMFT directly works in the thermodynamical limit of infinite system size and is exact in the case of infinite dimensions, it must be regarded as a strong approximation for low-dimensional problems due to the neglected spatial correlations. Finally, and most importantly for coupled-electron-phonon systems, the infinite Hilbert-space associated with the bosonic degrees of freedom represents a substantial difficulty for ED, DMRG and CPT (with ED) in contrast to QMC.

Other QMC-methods, include Stochastic Series Expansion (SSE) introduced and extended by Sandvik and Kurkijärvi [107], where the partition function is treated non-perturbative in powers of the Hamiltonian. This and other world-line-like methods with loop or worm algorithms are suffering from an undesirably bad sign problem for dimensionality higher than one, far worse than in the DetQMC. There are as well DetQMC (or related) algorithms which try to compensate or overcome the minus-sign problem (or also nodal problem for the auxiliary fields), generally known as constrained- path or fixed-node QMC [108, 109]. Unfortunately, dropping the *fermionic noise* leads only to approximate results as already discussed by Klein and Pickett in 1976 [110]. The problem is that *all* regions of phase space are important but have contributions which tend to cancel each other. All those methods in this class can usually be extended to continuous time avoiding the Trotter-error. A continuous-time formalism for the DetQMC-method has been proposed by Rombouts and others [111]. Recently, a method without the need of the HS-transformation has been introduced by Rubtsov and others [112]. Both are discussed in the appendix about the imaginary-time discretization (App. A.1).

4 Analysis

In this chapter we will introduce the measured observables, their analysis and some theoretical background necessary for their interpretation.

4.1 Observables

4.1.1 Wick's theorem

The universal quantity calculated throughout the simulation is the thermal one particle Green's function. According to Wick's theorem the expectation value of an arbitrary (time-ordered) product of creators and annihilators for a bilinear Hamiltonian can be expressed through the Green's function in order to calculate any observables of interest [113, 93]. In the extended Hubbard model the Hamiltonian is bilinear for every configuration of the auxiliary fields.

We follow Ref. [114] and define the *contraction* between two arbitrary creation (annihilation) operators A and B as

$$\overbrace{AB} \equiv AB - \{AB\} \,, \tag{4.1}$$

where $\{AB\}$ indicates the normal-ordered form of the pair (thus all annihilation operators standing to the right of all creation operators). As one can easily check, the only nonzero contraction of the combination of a creator-annihilator pair is

$$\overbrace{c_i c_j^\dagger} = c_i c_j^\dagger - \{c_i c_j^\dagger\} = c_i c_j^\dagger + c_j^\dagger c_i \delta_{ij} \,. \tag{4.2}$$

Thus only a limited number of pairings of creators and annihilators are physically interesting: an annihilator applied to the vacuum makes sense only in case it is trailed by a creator. The used anticommutator relations are given in App. A.2. The Wick's

reduction of a general time-ordered product of interaction-free particles is given by the sum of all contractions which is a sum of single particle propagators.

For a fixed HS-configuration of Ising-spins, one has a free theory interacting with the HS-fields. Thus, Wick's theorem holds and an observable can be given by its Wick's reduction. As an example consider an operator consisting of two creators and two annihilators. With the equal time Green's function $\langle c_{i\sigma}\, c^\dagger_{j\sigma'}\rangle = \delta_{\sigma\sigma'} G^\sigma_{ij}$ one can write [114]

$$\begin{aligned}
\langle c^\dagger_{i_1\sigma_1} c_{i_2\sigma_2} c^\dagger_{i_3\sigma_3} c_{i_4\sigma_4}\rangle &= \langle c^\dagger_{i_1\sigma_1} c_{i_2\sigma_2}\rangle\langle c^\dagger_{i_3\sigma_3} c_{i_4\sigma_4}\rangle + \langle c^\dagger_{i_1\sigma_1} c_{i_4\sigma_4}\rangle\langle c_{i_2\sigma_2} c^\dagger_{i_3\sigma_3}\rangle \\
&= \left(\delta_{i_1 i_2}\delta_{\sigma_1\sigma_2} - \langle c_{i_2\sigma_2} c^\dagger_{i_1\sigma_1}\rangle\right)\cdot\left(\delta_{i_3 i_4}\delta_{\sigma_3\sigma_4} - \langle c_{i_4\sigma_4} c^\dagger_{i_3\sigma_3}\rangle\right) \\
&\quad + \left(\delta_{i_1 i_4}\delta_{\sigma_1\sigma_4} - \langle c_{i_4\sigma_4} c^\dagger_{i_1\sigma_1}\rangle\right)\langle c_{i_2\sigma_2} c^\dagger_{i_3\sigma_3}\rangle \\
&= \delta_{\sigma_1\sigma_2}\delta_{\sigma_3\sigma_4}\left(\delta_{i_1 i_2} - \mathcal{G}^{\sigma_1}_{i_2 i_1}\right)\left(\delta_{i_3 i_4} - \mathcal{G}^{\sigma_3}_{i_4 i_3}\right) \\
&\quad + \delta_{\sigma_1\sigma_4}\delta_{\sigma_2\sigma_3}\left(\delta_{i_1 i_4} - \mathcal{G}^{\sigma_1}_{i_4 i_1}\right)\mathcal{G}^{\sigma_2}_{i_2 i_3}\,. \qquad (4.3)
\end{aligned}$$

The number of terms necessary for an operator of n pairs is $n!$, thus this leads to rather complicated expressions which can be constructed and simplified with the help of Mathematica. As reviewed by Assaad [115] any n-point correlation function ($n \geq 1$) can now be decoupled into a sum of products of Green's functions (two point correlators).

4.1.2 Static quantities

In our DetQMC simulation the thermodynamic expectation value for the operator A

$$\langle A\rangle = \frac{1}{\mathcal{Z}}\,\mathrm{tr}\, A\,\mathrm{e}^{-\beta H} = \frac{1}{\mathcal{Z}}\,\mathrm{tr}\,\tilde{A}\,\mathrm{e}^{-\beta\tilde{H}}\,, \qquad (4.4)$$

become using importance sampling

$$\langle A\rangle = \lim_{N_{\mathrm{meas}}\to\infty}\frac{1}{N_{\mathrm{meas}}}\sum_{i=1}^{N_{\mathrm{meas}}} A(x_i)\,, \qquad (4.5)$$

where N_{meas} is the number of measurements taken at HS-field configurations $\check{x}_i$. For a finite number of measurements the estimate for $\langle A\rangle$ is given by

$$\overline{A} = \frac{1}{N_{\mathrm{meas}}}\sum_{i=1}^{N_{\mathrm{meas}}} A(x_i)\,, \qquad (4.6)$$

and the fluctuation around the true expectation value $\langle A\rangle = \overline{A} \pm \Delta\overline{A}$. The methods to obtain correct estimates for the statistical error $\Delta\overline{A}$ will be described in Sec. 4.3. We will now give an overview of the basic observables.

Our universal quantity, the thermal one-particle Green's function for the the Hamiltonian under LF-transformation $\tilde{G}$ is given by

$$\tilde{G}^{\sigma}(\tau,\tau',i,j) = -\mathrm{i}\left\langle T\,\tilde{c}_{i\sigma}(\tau)\,\tilde{c}^{\dagger}_{j\sigma}(\tau')\right\rangle . \tag{4.7}$$

For equal-time observations $\tau = \tau'$ the Wick time-order operator T can be dropped and the Green's functions are given by

$$\tilde{G}^{\sigma,a}_{ij} = -\mathrm{i}\left\langle \tilde{c}_{i\sigma}\tilde{c}^{\dagger}_{j\sigma}\right\rangle \tag{4.8}$$

$$\tilde{G}^{\sigma,b}_{ij} = \left\langle \tilde{c}^{\dagger}_{i\sigma}\tilde{c}_{j\sigma}\right\rangle , \tag{4.9}$$

Working in real-space and imaginary time, we have for the one-electron Green's function within the DetQMC-algorithm as defined in Eq. (3.37). The computation of the static quantities within the formalism as a thermal average is straightforward. The particle density is given by

$$\left\langle n\right\rangle = \frac{1}{N}\sum_{i,\sigma}\left\langle n^{\sigma}_{i}\right\rangle , \tag{4.10}$$

where the expectation value $\left\langle n^{\sigma}_{i}\right\rangle$ can be calculated from the trace over the Green's function Eq. (4.9) via $\left\langle n^{\sigma}_{i}\right\rangle = \left\langle \tilde{\mathcal{G}}^{b,\sigma}_{ii}\right\rangle$. The sum over the off-diagonal elements yields the kinetic energy

$$E_{\mathrm{k}} = -t\sum_{<ij>,\sigma}\left\langle \tilde{c}^{\dagger}_{i\sigma}\tilde{c}_{j\sigma}\right\rangle = -\frac{t}{N}\sum_{<ij>,\sigma}\left\langle \tilde{\mathcal{G}}^{\sigma,b}_{ji}\right\rangle . \tag{4.11}$$

The total energy can now be obtained from the thermodynamic relation

$$\begin{aligned} E &= \frac{\partial}{\partial\beta}\ln\mathcal{Z} \\ &= E_{\mathrm{k}} + E_{\mathrm{U}} + E_{\mathrm{V}} + E_{\mathrm{ph}} - 2E_{\mathrm{P}}\sum_{i,\sigma}\left\langle n^{\sigma}_{i}\right\rangle , \end{aligned} \tag{4.12}$$

where E_{P} is the polaron binding energy given in Eq. (2.20) and $\sum_{i,\sigma}\left\langle n^{\sigma}_{i}\right\rangle$ yields the number of electrons. The remaining terms are the kinetic energy given in Eq. (4.11), the onsite and inter-site Hubbard terms which can be easily computed from combinations of $\left\langle n^{\sigma}_{i}\right\rangle$ and the phonon contribution

$$E_{\mathrm{ph}} = \frac{N}{2\Delta\tau} - \frac{1}{2\omega_0\Delta\tau^2}\sum_{i,\tau_l}\left\langle \left(p_{i,\tau_l} - p_{i,\tau_{l+1}}\right)^2\right\rangle + \frac{\omega_0}{2}\sum_{i,\tau_l}\left\langle p^2_{i,\tau_l}\right\rangle , \tag{4.13}$$

which corresponds to the bosonic action in Eq. (3.70). For comparison with other work one can subtract the ground state energy of the phonons $E_{0,\mathrm{ph}} = N\omega_0/2$.

Any quantity can be constructed from these simple expressions as one employs Wick's theorem to reduce the expectation values of arbitrary constructs of creation and annihilation operators to a sum of single particle propagators.

Static structure factors and order parameter

The connected correlation functions to measure the charge- and spin-fluctuations in **k**-space are given by

$$S_c(\mathbf{k}) = \frac{1}{N}\sum_{<ij>} \mathrm{e}^{\mathrm{i}\mathbf{k}(\mathbf{r}_i-\mathbf{r}_j)} \left(\langle n_i n_j\rangle - \langle n\rangle^2\right) \tag{4.14}$$

$$S_s(\mathbf{k}) = \frac{1}{N}\sum_{<ij>} \mathrm{e}^{\mathrm{i}\mathbf{k}(\mathbf{r}_i-\mathbf{r}_j)} \left(\sum_i \langle S_i^z S_j^z\rangle - \langle S^z\rangle^2\right) \tag{4.15}$$

$$\text{with} \quad S_i^z = \frac{1}{2}\left(n_{i\uparrow} - n_{i\downarrow}\right) \ .$$

Here we can restrict ourselves to measure S^z due to the $O(3)$ symmetry of the spins in space. Connected correlation function means to subtract the average (order) parameter, such that only the fluctuations are measured. The corresponding structure factors S_C and S_S are the non-connected correlation functions at vector $\mathbf{Q} = (\pi, \pi)$ which can be obtained simply as one drops the quadratic term.

The spin- and charge-correlation function provide information about the strength of magnetic order, charge order or traces of phase separation. The order parameter for the zig-zag charge pattern on the ladder is therefore

$$m_{CO}^2 = \frac{1}{N\langle n\rangle^2}\, S_c(\mathbf{Q}) \,, \tag{4.16}$$

where $\langle n\rangle^2$ ensures that the order parameter is equal to unity for full charge order. In the latter case the electron density or valence at the occupied sites is $\langle n\rangle = \frac{1}{2} \pm \frac{m_{CO}}{2}$.

4.1.3 Dynamic quantities

Imaginary time displaced, dynamic response functions, or spectral functions are represented by the imaginary part of Green's functions [93] of the type

$$A_{\mathcal{O}}(\mathbf{k},\omega) = \mathcal{I}\,\frac{1}{\pi}\langle E_n|\mathcal{O}^\dagger(\mathbf{k})\frac{1}{\omega - (H - E_n) - \mathrm{i}0_+}\mathcal{O}(\mathbf{k})|E_n\rangle \ , \tag{4.17}$$

here is $\mathbf{k}$ the wave number and ω the angular-frequency – in natural units ($\hbar = 1$) these are interpreted as momentum and energy. They determine at which energy and momentum the response of the system to an outer perturbation is probed. This way the primary excitations, their interplay and their stability can be extracted, providing insight into the dynamics of the quantum system. Quantities like spin- or charge-susceptibility,

optical conductivity and single particle spectral functions provide the possibility of direct comparison with experiments, such as electron energy loss-, neutron scattering- or photo-emission spectroscopy as described in App. A.4.

The relation between the representation in Eq. (4.17) and correlators or Green's functions in imaginary time can be shown via the spectral theorem [92]. From here on we use a notation without phonon degrees of freedom for simplicity. The spectral function of the operator $\mathcal{O}$ is given by

$$A_{\mathcal{O}}(\omega) = -\frac{1}{\pi}\mathrm{Im}\, G^{\mathrm{ret}}_{\mathcal{O}}(\omega)\ , \tag{4.18}$$

where $G^{\mathrm{ret}}_{\mathcal{O}}$ denotes the retarded (time-displaced) Green's function for the operator $\mathcal{O}$. In the DetQMC formulation this time-displaced Green's function can be defined by writing the operator $c_{i\sigma}$ at time-slice τ_l

$$c_{i\sigma}(\tau_l) = \mathrm{e}^{\mathrm{i}\,\Delta\tau(H_l^\alpha - \mu N)}\, c_{i\sigma} \mathrm{e}^{-\mathrm{i}\,\Delta\tau(H_l^\alpha - \mu N)} = \sum_{i'} \left(\mathbf{B}_l^\sigma\right)_{ii'}\, c_{i'\sigma}(\tau_{l-1})\ , \tag{4.19}$$

where H_l^α is the decoupled Hamiltonian at slice l. Consequently, the time-displaced Green's function is given by

$$\left\langle c_{i\sigma}(\tau_l)\, c^\dagger_{j\sigma}(0)\right\rangle = \sum_{i'} \left(\mathbf{B}_l^\sigma \mathbf{B}_{l-1}^\sigma \dots \mathbf{B}_1^\sigma\right)_{ii'} \left\langle c_{i'\sigma}(0)\, c^\dagger_{j\sigma}(0)\right\rangle\ . \tag{4.20}$$

Owing to Eq. (3.37) we can express the time-displaced Green's function as

$$\left\langle c^\dagger_{i\sigma}(\tau_l)\, c_{j\sigma}(0)\right\rangle = \left(\left(\mathbf{1} + \mathbf{B}_L^\sigma \mathbf{B}_{L-1}^\sigma \dots \mathbf{B}_1^\sigma\right)^{-1} \mathbf{B}_L^\sigma \mathbf{B}_{L-2}^\sigma \dots \mathbf{B}_{l+1}^\sigma\right)_{ji}\ . \tag{4.21}$$

Remember that as described in Sec. 3.6.3 for phonons additional pairs of phases corresponding to the time-slices have to be applied!

With these two Green's functions, the static Green's function Eq. (3.37) and the Wick theorem, any dynamical quantity can be computed. Unfortunately, multi-point correlation functions like current- current correlators are hard to obtain with a simulation, since their expectation values strongly fluctuate giving rise to large error bars.

One particle Green's function

Inserting a complete set of eigenstates before and after the observable in Eq. (4.17) one obtains

$$A_{\mathcal{O}}(\mathbf{k},\omega) = \sum_i \left|\left\langle E_i\middle|\mathcal{O}(\mathbf{k})\middle|E_n\right\rangle\right|^2 \delta(\omega - (E_i - En))\ , \tag{4.22}$$

with the eigenstates $\langle E_n \rangle$ for eigenvalues E_n of the Hamiltonian. Photo-emission (inverse photo-emission) measurements correspond to spectral weight function $A_k^+(\omega)$ ($A_k^-(\omega)$). These are basically determined through transition matrix elements to the particle-states n, m with the particle numbers N_m, $N_n = n_m + 1$ such that

$$\begin{aligned} A(\mathbf{k},\omega) \quad \propto \quad & \frac{1}{\mathcal{Z}} \sum_{m,n} \left| \langle \Psi_n | c_k^\dagger | \Psi_m \rangle \right|^2 \, \mathrm{e}^{-\beta(E_m - \mu N_m)} \left(1 - \mathrm{e}^{-\zeta\beta\omega} \right) \\ & \times 2\pi\delta \left(E_n - E_m - \mu - \omega \right) \, , \end{aligned} \tag{4.23}$$

and

$$A_k^+(\omega) \quad \propto \quad \sum_m \left| \langle \Psi_0^N | c_k | \Psi_0^{N+1} \rangle \right|^2 \, \delta \left(\omega - \left(E_0^{N+1} - E_0^N \right) \right) \tag{4.24}$$

$$A_k^-(\omega) \quad \propto \quad \sum_m \left| \langle \Psi_0^N | c_k^\dagger | \Psi_0^{N-1} \rangle \right|^2 \, \delta \left(\omega - \left(E_0^N - E_0^{N-1} \right) \right) \, . \tag{4.25}$$

This is the Lehmann representation of the operators

$$\begin{aligned} A_{ij}^+ &= \langle c_{i\sigma}^\dagger(\tau_2) \, c_{i\sigma}(\tau_1) \rangle \\ A_{ij}^- &= \langle c_{i\sigma}(\tau_2) \, c_{i\sigma}^\dagger(\tau_1) \rangle \end{aligned} \quad , \quad \text{for} \qquad \tau_2 > \tau_1 \, . \tag{4.26}$$

The time-displaced one particle Green's function reflects the system's reaction to particles (electrons) with a distinct energy ω inserted or removed with the moment $\mathbf{k}$. The integral over all momenta gives the density of states (DOS) of the system.

The time time-displaced one-particle Green's function is related to the spectral function via Eq. (4.18)

$$G^b(\mathbf{k},\tau) = \langle c_{\mathbf{k}\sigma}^\dagger(\tau) c_{\mathbf{k}\sigma} \rangle \tag{4.27}$$

is related to the spectral function via Eq. (4.18) such that

$$G^b(\mathbf{k},\tau) = \int_{-\infty}^{+\infty} d\omega \, \frac{\mathrm{e}^{-\tau\omega}}{1 + \mathrm{e}^{-\beta\omega}} \, A(\mathbf{k},\omega) \, . \tag{4.28}$$

As will be discussed in Sec. 4.4 the inversion of of Eq. (4.28) is ill-conditioned and can be obtained using Maximum Entropy. The function $G^b(\mathbf{k},\tau)$ is computed via Fourier transformation from the measured Green's function

$$G^b(\mathbf{k},\tau) = \frac{1}{N} \sum_{ij} \mathrm{e}^{\mathrm{i}\mathbf{k}(\mathbf{r}_i \mathbf{r}_j)} G_{ij}^b(\tau) \, . \tag{4.29}$$

Spin- and charge-susceptibility

Similar to the spectral function we can express the spin- and the charge-susceptibility by defining

$$\mathcal{O}_S(\mathbf{k}) = S^z_{\mathbf{k}} = \sum_{\mathbf{p}} \left(c^\dagger_{\mathbf{p}+\mathbf{k},\uparrow} c_{\mathbf{p},\uparrow} - c^\dagger_{\mathbf{p}+\mathbf{k},\downarrow} c_{\mathbf{p},\downarrow} \right) \tag{4.30}$$

$$\mathcal{O}_C(\mathbf{k}) = \rho_{\mathbf{k}} = \sum_{\mathbf{p}} n_{\mathbf{p}} = \sum_{\mathbf{p},\sigma} c^\dagger_{\mathbf{p}+\mathbf{k},\sigma} c_{\mathbf{p},\sigma} \tag{4.31}$$

With the spectral theorem we can obtain the susceptibilities via the inversion of

$$\left\langle \mathcal{O}_{S,C}(\mathbf{k},\tau)\, \mathcal{O}_{S,C}(\mathbf{k},0) \right\rangle = -\mathrm{i} \int_\infty^\infty d\omega \, \frac{\mathrm{e}^{-\tau\omega}}{1-\mathrm{e}^{-\beta\omega}} \chi_{S,C}(\mathbf{k},\omega) \; . \tag{4.32}$$

Here the kernel $\frac{\mathrm{e}^{-\tau\omega}}{1-\mathrm{e}^{-\beta\omega}}$ with the minus in the denominator is used since the susceptibilities are bosonic quantities.

4.2 The sign problem

Determinant Monte Carlo

As flexible as the DetQMC method is, its curse is the notorious (and in general unsolved) minus-sign problem evident in any kind of fermionic QMC.

Apart from half filling, particle-hole symmetry is no longer conserved in the repulsive Hubbard model. This implies that the fermionic determinant defined in Eq. (3.28) is no longer strictly positive, nor factorizes. Consequently the weights $w_\mathrm{f}[\check{x}]$ in Eq. (3.33) can become negative, no longer representing a probability for a specific configuration. In this situation it is necessary to deal with the estimators by taking the absolute value of the weight and including the sign explicitly in the observables

$$\left\langle A \right\rangle = \frac{\sum_{\{\check{x}\}} |w_\mathrm{f}[\check{x}]| \, \mathrm{sign}(w_\mathrm{f}[\check{x}]) \, A(\check{x})}{\sum_{\{\check{x}\}} |w_\mathrm{f}[\check{x}]| \, \mathrm{sign}(w_\mathrm{f}[\check{x}])} \overset{\mathrm{MC}}{\approx} \frac{\sum_{k=1}^K A_k \, sign_k}{\sum_{k=1}^K sign_k} \tag{4.33}$$

where (compare with Eq. (3.29))

$$\left\langle sign \right\rangle = \frac{\mathcal{Z}_{w_\mathrm{f}}}{\mathcal{Z}_{|w_\mathrm{f}|}} = \frac{\sum_{\{\check{x}\}} w_\mathrm{f}[\check{x}]}{\sum_{\{\check{x}\}} |w_\mathrm{f}[\check{x}]|} = \mathrm{e}^{-\beta N \Delta f} \; . \tag{4.34}$$

Here Δf denotes the difference of the free energy densities. The average sign is strictly positive and real.

Unfortunately, the problem gets worse with decreasing temperature $1/\beta$ and increasing system size N. As the partition functions in Eq. (4.34) are exponentials and the average sign is a fraction of exponentials, the problem behaves like an exponential $\mathrm{e}^{-\beta N}$. The average sign is decreasing rapidly with temperature, for large clusters and large couplings – where, for too small values of $\langle\, sign \,\rangle$, the fluctuations of $A_k\, sign_k$ dominate and the computational cost to obtain converging estimators is enormous.

For $U < 0$ (attractive interaction) there is no sign-problem since $M^{\uparrow} = M^{\downarrow}$ in Eq. (3.28). Consequently, the product of two determinants in Eq. (3.29) becomes a square and therefore strictly positive semidefinite, even though the determinant itself is not positive semidefinite.

The origin of the minus-sign problem is controversial and can be explained as a consequence of the Hubbard-Stratonovich transformation [99, 73]. Since, for strong coupling the Hubbard-Stratonovich fields display quasi-world-line behavior the minus-sign might then be understood as a crossing of fermion-lines in Euclidean time [91]. As shown by Batrouni and Scalettar anomalous decouplings (others than the decomposition used in Sec. 3.3) yield the same problem [116]. In fact, Batrouni and Forcrand argue that there is no general Hubbard-Stratonovich transformation that is capable of giving a semidefinite positive product of the determinants [117].

Recently, Troyer and Wiese [66] argued the sign problem to be generically NP-hard (nondeterministic polynomial), hence not solvable in polynomial growing time effort [118]. Their discussion is based on the mapping of the fermionic quantum system to the classical spin-glass model, which is believed to be NP-hard. Since any NP-hard problem can be mapped onto another with polynomial complexity, a general solution of an NP-hard problem is thus equivalent solving *any* NP-problem[1]. Nevertheless, it is still possible that specific sign problems, like that for DetQMC may be solved. For an example in a different model see Chandrasekharan's and Wiese's Meron-Cluster solution [119].

In Fig. 4.1 the avergage sign versus the inter-site coupling V at inverse temperature $\beta = 8.0$ and the parameters given in Sec. 2.8 is plotted. The figure shows the values which apply to our simulation results in chapter 5. It increases with V and as we will see with increasing charge order. The devolution for the ladder lengths of $N_x = 8, 16$ and 32 rungs shows that the problem gets worse with increasing system size. In this work the most expensive simulation has been perfomed for a ladder of 32 rungs (64 sites) at $V = 1.0$ and an average sign of ≈ 0.9.

[1] This would revolutionize computing algorithms and compromise all classical encryption methods. If you are the lucky one who solves the problem in general – get ready for your ticket to Stockholm!

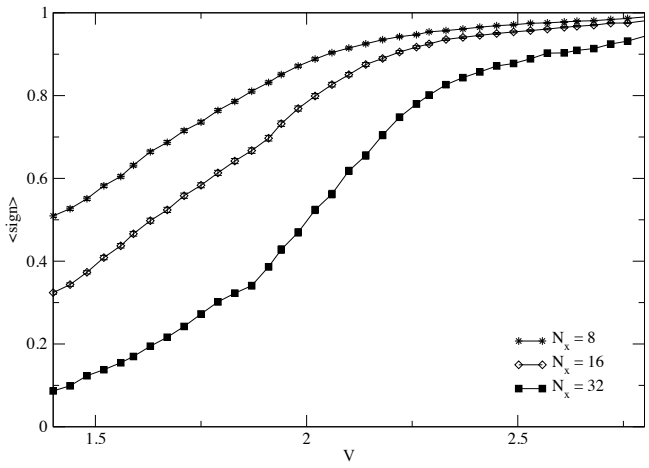

Fig. 4.1: average sign versus intersite coupling for ladders of $N_x = 8, 16, 32$ rungs at $\beta = 8.0$. Error bars are small than symbols.

Determinant Monte Carlo under LF-transformation

The determinant-based grand-canonical simulation of the pure Holstein model (without U, or V) with phonon coordinates $a(x,t)$ as dynamic variables at any filling does not suffer from the sign-problem, since the coupling of electrons and phonons is the same for both spin directions. The model after LF transformation however, is afflicted by some *fermionic noise*.

As Hohenadler stated [62, 43], the sign problem in this approach has a different origin. The transformation introduces an attractive Hubbard on-site term which could still allow factorization of the determinant and therefore this cannot be the source of evil. In fact, the negative weights are a result of the complex phase factor in the transformed hopping term (Eq. (2.24)).

In our spinful many-electron case of the Hubbard-Holstein model including the LF transformation, we face this additional *phononic* sign-problem (or phase-problem) as well. It behaves similar to the fermionic one, getting worse with increasing system size and decreasing temperature. BUT: it is much more severe! Where the average sign is near one for small systems up to 8 sites, $\beta = 10$ and electron-phonon coupling $\lambda < 1.0$ at frequencies $\omega_0 > 1.0$ and a large range of the parameters β and U it drops off rapidly for larger systems and temperatures.

Unfortunately the sign-problem for our set of paramters (see Sec. 2.8) is so severe that we are forced to abandon the intention to include the coupling to lattice degrees of freedom in our simulation. The problem arises already for very small systems. Since

the approach to sample via principle components in a LF-transformed model works for investigations of the bipolaron (only two electrons) in the Hubbard Holstein model we stress that the here presented approach might find its application in systems with low electron density.

4.3 Data analysis

Although several sweeps are skipped between measurements the data are correlated and blue-eyed analysis would severely bias the results. Therefore, the autocorrelation times have to be calculated, uncorrelated means have to be determined and from those the variances can be computed unbiased. This procedure provides trustworthy and statistically correct estimators, errors and their correlations [120].

4.3.1 Binning and autocorrelation time

The small changes in the electronic-configuration via single spin flips cause statistical correlations which have to be taken into account in the analysis. To quantify these correlations we define the autocorrelation function for an observable $\mathcal{O}$

$$\begin{aligned} C_{\mathcal{O}}(t) = C_{\mathcal{O}}(\mathcal{O}_i, \mathcal{O}_{i+t}) &= \left\langle \left(\mathcal{O}_i - \left\langle \mathcal{O}_i \right\rangle\right)\left(\mathcal{O}_{i+t} - \left\langle \mathcal{O}_{i+t} \right\rangle\right) \right\rangle \\ &= \left\langle \mathcal{O}_i \mathcal{O}_{i+t} \right\rangle - \left\langle \mathcal{O}_i \right\rangle \left\langle \mathcal{O}_{i+t} \right\rangle , \end{aligned} \tag{4.35}$$

where the number index i denotes the number of the measurement and t defines the separation of the measurements in the time-series. In this section we use $\left\langle \dots \right\rangle$ to denote the average over all indices i. In the limit $N \to \infty$ measurements, this becomes the physical expectation value. For $t = 0$ the correlation function equals the variance in case of single uncorrelated measurements $\sigma^2_{\mathcal{O}}$. With this definition we introduce the normalized autocorrelation function given by

$$\Gamma(t) = \frac{C_{\mathcal{O}}(t)}{C_{\mathcal{O}}(0)} = \sum_{i=1}^{N-t} \frac{\left\langle \mathcal{O}_i \mathcal{O}_{i+t} \right\rangle - \left\langle \mathcal{O}_i \right\rangle \left\langle \mathcal{O}_i \right\rangle}{\left\langle \mathcal{O}_i^2 \right\rangle - \left\langle \mathcal{O}_i \right\rangle \left\langle \mathcal{O}_i \right\rangle} , \tag{4.36}$$

with N as the total number of measurements. For increasing separation in the time-series, $\Gamma(t)$ decays exponentially

$$\Gamma(t) \overset{t\to\infty}{\longrightarrow} a \, \mathrm{e}^{-t/\tau_{\mathcal{O},\mathrm{exp}}} , \tag{4.37}$$

where $\tau_{\mathcal{O},\mathrm{exp}}$ denotes the so-called *exponential* autocorrelation time and a is a constant. The exponential autocorrelation time defines the upper limit of how strongly subsequent

measurements are correlated. The variance of correlated measurements is calculated by collecting the diagonal and off-diagonal terms of

$$\begin{aligned}
\sigma^2_{\mathcal{O}} &= \frac{1}{N^2}\sum_{i,j=1}^{N}\langle\mathcal{O}_i\mathcal{O}_j\rangle - \frac{1}{N^2}\sum_{i,j=1}^{N}\langle\mathcal{O}_i\rangle\langle\mathcal{O}_j\rangle = \frac{1}{N^2}\sum_{i,j=1}^{N} C_{\mathcal{O}}\left(|i-j|\right) \\
&= \frac{1}{N^2}\sum_{t=-N+1}^{N-1}\sum_{k=1}^{N-|t|} C_{\mathcal{O}}\left(|t|\right) = \sum_{t=-N}^{N} C_{\mathcal{O}}\left(|t|\right)\frac{N-|t|}{N^2} \\
&= \frac{C_{\mathcal{O}}\left(0\right)}{N}\sum_{t=-N}^{N}\Gamma_{\mathcal{O}}\left(|t|\right)\left(1-\frac{|t|}{N}\right) \\
&= \frac{\sigma^2_{\mathcal{O}}}{N}\,2\left[\frac{1}{2}+\sum_{t=1}^{N}\Gamma_{\mathcal{O}}\left(t\right)\left(1-\frac{t}{N}\right)\right] = \frac{\sigma^2_{\mathcal{O}}}{N}\,2\tau_{\mathcal{O},\mathrm{int}}\ . \qquad (4.38)
\end{aligned}$$

Here, we defined the so-called (proper) *integrated* autocorrelation time

$$\tau_{\mathcal{O},\mathrm{int}} = \frac{1}{2}+\sum_{t=1}^{N}\Gamma_{\mathcal{O}}\left(t\right)\left(1-\frac{t}{N}\right) = \frac{N\sigma^2_{\mathcal{O}}}{2\,\sigma^2_{\mathcal{O}}}\ , \qquad (4.39)$$

where in realistic models $\tau_{\mathcal{O},\mathrm{int}} \leq \tau_{\mathcal{O},\mathrm{exp}}$ [121]. In some descriptions, the factor $(1-t/N)$ is neglected. This is justified, since it vanishes with large N and is additionally suppressed by the exponentially decreasing normalized autocorrelation function. One can now determine the integrated autocorrelation time by integrating the autocorrelation function in Eq. (4.38) for increasing separations up to sufficiently large t and by estimating the remaining contributions from the slope of the asymptotic exponential behavior.

For a large number of data sets, invoking the analysis by integration (Eq. (4.38)) to obtain the integrated autocorrelation time is often too cumbersome for a day by day basis [120] – the data analysis would easily exceed the simulation time. A fast estimation of the autocorrelation time can be obtained from plots of the MC time-series of observables. Autocorrelations of large time-scales can be identified by eye. Note that the expression in Eq. (4.38) is correct for simple averages only. For sign-afflicted observables additional terms have so be taken into account (see below).

The binning (or blocking) analysis is much more convenient, though somewhat less accurate than full integration of Eq. (4.38). By grouping the incoming data into bins, one forms a new (shorter) time series. Large enough bin-sizes result in a series of almost uncorrelated block-values and thus can be analyzed by standard means. Let us assume that the original data time series consists of N correlated measurements $\mathcal{O}_i$. We block them in N_B bins of length k such that $N = N_B\,k$. The block-average of the n-th bin is

given by

$$\mathcal{O}_{B,n} = \frac{1}{k}\sum_{i=1}^{k} \mathcal{O}_{(n-1)\,k+i} \qquad n = 1, \ldots, N_B \; . \tag{4.40}$$

Obviously, the mean value over all bin-averages satisfies $\overline{\mathcal{O}}_B = \overline{\mathcal{O}}$. If the bins are large enough to form a basically uncorrelated series, their variance can be computed as an unbiased estimator leading to the square of the error of the mean value

$$\epsilon^2_{\overline{\mathcal{O}}} \equiv \sigma^2_{\overline{\mathcal{O}}} \simeq \frac{\sigma^2_B(N_B)}{N_B} \equiv \frac{1}{N_B\,(N_B-1)} \sum_{n=1}^{N_B} \left(\mathcal{O}_{B,n} - \overline{\mathcal{O}}_B\right)^2 \; . \tag{4.41}$$

The integrated autocorrelation time is now given by

$$\tau_{\mathcal{O},\mathrm{int}}(N_B) = \frac{k\,\sigma^2_B(N_B)}{2\,\sigma^2_{\mathcal{O}_i}} \; , \tag{4.42}$$

which grows monotonically with decreasing binning block-number N_B (and therefore statistical independence) converging to the integrated autocorrelation time $\tau_{\mathcal{O},\mathrm{int}}$. If $\tau_{\mathcal{O},\mathrm{int}}(N_B)$ does not converge, then the expectation value at the largest available N_B is a lower bound for $\tau_{\mathcal{O},\mathrm{int}}$, giving a lower bound for the error of $\mathcal{O}$. In that case, the simulation has not converged and one cannot deduce reliable physical results for $\langle\mathcal{O}\rangle$. For increasing block-sizes, the number of data-points becomes small and the uncertainty of the estimate for $\tau_{\mathcal{O},\mathrm{int}}$ increases. The calculated estimates for the autocorrelation time may converge but then start to fluctuate heavily, over- or under- estimating the *correct* value. It is therefore reasonable to stop increasing the block-size if the error of $\tau_{\mathcal{O},\mathrm{int}}$ becomes of the order of $\tau_{\mathcal{O},\mathrm{int}}$ itself, or if $\tau_{\mathcal{O},\mathrm{int}}$ becomes significantly smaller for a block-size which is larger than the preceding block-size.

Due to these temporal correlations of the measurements the statistical error $\epsilon_{\overline{\mathcal{O}}} = \sigma_{\overline{\mathcal{O}}}$ of the MC-estimator $\mathcal{O}$ is increased by a factor $\sqrt{2\,\tau_{\mathcal{O},\mathrm{int}}}$. This leads to the *effective* statistics

$$N_{\mathrm{eff}} = \frac{N}{2\,\tau_{\mathcal{O},\mathrm{int}}} \; , \quad \text{or respectively} \quad \sigma^2_{\overline{\mathcal{O}},\mathrm{eff}} = 2\,\tau_{\mathcal{O},\mathrm{int}}\,\sigma^2_{\overline{\mathcal{O}}} \; , \tag{4.43}$$

which shows that only every $2\,\tau_{\mathcal{O},\mathrm{int}}$-th measurement is approximately uncorrelated. By tuning the number of sweeps skipped between MC-measurements with respect to the integrated autocorrelation time, the computational overhead can be reduced. For n-point correlators, which require a ten times better statistic than simple observables (by rule of thumb) – their much stronger autocorrelations additionally increase the computational costs.

Finally, we briefly mention the issue of *critical slowing down*. While the autocorrelation-time depends on the updating algorithm, it is also influenced by the parameters of the lattice system. One can expect the integrated (exponential) autocorrelation

time to increase as $\tau_{\text{int}} \sim \xi^z$, where ξ is the leading correlation length in the system and z denotes the dynamical critical exponent *of the MC algorithm* employed. As one approaches a phase transition, the correlation length diverges, or on the finite lattice becomes of the order of the system size $\xi \leq N$ ($\xi \leq L$ for correlations in imaginary time). The computational effort then grows typically like $NL \min[\xi, N, L]^z$. For local updates one expects $z \approx 2$ [70].

Sign bias[2]

We measure estimates of the form

$$\langle \mathcal{O} \rangle = \frac{\langle \mathcal{O}\, w \rangle}{\langle w \rangle} \approx \frac{\overline{\mathcal{O}\, w}}{\overline{w}} = \frac{\sum_{i=1}^{N} \mathcal{O}_i\, w_i}{\sum_{i=1}^{N} w_i} \,, \tag{4.44}$$

where we identify w as the sign or the phase discussed in Sec. 4.2. Unfortunately, these represent a non-linear combination of the basic observable $\mathcal{O}$ and w, thus trivial error propagation is no longer valid. The correct estimates and errors can be calculated simply via the Jackknife procedure explained in the next section. Another way is to compute the error propagation directly. The exact estimator is given by

$$\langle \mathcal{O} \rangle = \langle \mathcal{O} \rangle_{\text{biased}} \left[1 - \frac{\langle \overline{\mathcal{O}\, w}; \overline{\mathcal{O}\, w} \rangle}{\langle \overline{\mathcal{O}\, w} \rangle^2} + \frac{\langle \overline{w}; \overline{w} \rangle}{\langle \overline{w}^2 \rangle} + \dots \right] \tag{4.45}$$

with $\langle \mathcal{O} \rangle_{\text{biased}}$ defining the naive expectation value and the abbreviation $\langle \overline{\mathcal{O}\, w}; \overline{w} \rangle = \langle \overline{\mathcal{O}\, w\, w} \rangle - \langle \overline{\mathcal{O}\, w} \rangle \langle \overline{w} \rangle$. The error is then given by

$$\sigma^2_{\mathcal{O}} = \langle \mathcal{O} \rangle^2_{\text{biased}} \left[\frac{\langle \overline{\mathcal{O}\, w}; \overline{\mathcal{O}\, w} \rangle}{\langle \overline{\mathcal{O}\, w} \rangle^2} + \frac{\langle \overline{w}; \overline{w} \rangle}{\langle \overline{w}^2 \rangle} - 2 \frac{\langle \overline{\mathcal{O}\, w}; \overline{w} \rangle}{\langle \overline{\mathcal{O}\, w} \rangle \langle \overline{w} \rangle} + \dots \right] \,, \tag{4.46}$$

or with $\langle \overline{\mathcal{O}\, w}; \overline{w} \rangle = \langle \mathcal{O}_i w_i; w_i \rangle \frac{2\tau_{\mathcal{O}w,w,\text{int}}}{N}$ via

$$\begin{aligned} \sigma^2_{\mathcal{O}} \;=\; \langle \mathcal{O} \rangle^2_{\text{biased}} \Bigg[& \frac{\langle \overline{\mathcal{O}\, w}; \overline{\mathcal{O}\, w} \rangle}{\langle \overline{\mathcal{O}\, w} \rangle^2} \frac{2\tau_{\mathcal{O}w,\text{int}}}{N} + \frac{\langle \overline{w}; \overline{w} \rangle}{\langle \overline{w}^2 \rangle} \frac{2\tau_{w,\text{int}}}{N} \\ & - 2 \frac{\langle \overline{\mathcal{O}\, w}; \overline{w} \rangle}{\langle \overline{\mathcal{O}\, w} \rangle \langle \overline{w} \rangle} \frac{2\tau_{\mathcal{O}w,w,\text{int}}}{N} \Bigg] \,. \end{aligned} \tag{4.47}$$

Since we only want to determine a good estimate of the integrated autocorrelation time, we will not employ Eq. (4.47), where we would need to do multiple binning analyzes for

[2] In this section we basically follow references [120] and [122].

the different integrated autocorrelation times $\tau_{\mathcal{O}w,\mathrm{int}}$, $\tau_{\mathcal{O}w,w,\mathrm{int}}$ and $\tau_{w,\mathrm{int}}$. Instead one can estimate of the variance by taking the first few terms of Eq. (4.46). This should be a reasonable approximation for the autocorrelation time.

4.3.2 Jackknife

With the knowledge of the integrated autocorrelation time, the means of the measured quantities and their error can be computed. Instead of solving the complicated error propagation of non-linear combinations of observables, the Jackknife method allows to obtain a controlled estimate of the variances. *automatically* [3] The method has also the advantage to give reliable results even for a small number of data points.

Similar to the binning analysis, the original data are blocked into bins of length $k = N/N_B$. To obtain the asymptotic error, k must be significantly larger than the relevant integrated autocorrelation time $\tau_{\mathcal{O},\mathrm{int}}$. With this approximately uncorrelated set of data points the, possibly highly nonlinear, analysis of, e.g., weighted observables will be then repeatedly done with all but one (varying) data point. First from all N_B data we calculate the overall average $\overline{\mathcal{O}}$. The Jackknife-averages $\mathcal{O}_{J,n}$ containing all but one of the block-values is obtained with the n-th-block-average $\mathcal{O}_{B,n}$ via

$$\mathcal{O}_{J,n} = \frac{N\overline{\mathcal{O}} - k\,\mathcal{O}_{B,n}}{N-k} \qquad n = 1, \ldots, N_B \; . \tag{4.48}$$

Then overall Jackknife-average $\overline{\mathcal{O}}_J = (1/N_B)\sum_{N_B} \mathcal{O}_{J,n}$. The N_B Jackknife blocks now containing $N-k$ data are trivially correlated since each of them originates from nearly the same $N_B - 1$ bins. This correlation (which has nothing to do with the temporal correlation of the original data) leads to under-estimated Jackknife block-variances. Fortunately, because of the trivial nature of this correlation, the underestimation can be corrected by multiplying with a factor $(N_B - 1)^2$ leading to the final error

$$\epsilon^2_{\mathcal{O}} = \sigma^2_{\mathcal{O}} = \frac{N_B - 1}{N_B} \sum_{n=1}^{N_B} \left(\mathcal{O}_{J,n} - \overline{\mathcal{O}}_J\right)^2 \; . \tag{4.49}$$

The estimator of the observable $\mathcal{O}$ is then given by

$$\mathcal{O} = \overline{\mathcal{O}} - \mathrm{Bias} \tag{4.50}$$

$$\mathrm{Bias} = (N_B - 1)(\overline{\mathcal{O}}_J - \overline{\mathcal{O}}) \; . \tag{4.51}$$

[3] The Jackknife is a very general procedure and can be utilized for a large number of problems to determine non-linear combinations [70].

As said before, in this procedure error propagation is *automatic* by making $N_B + 1$ analyzes using almost the full data-pool. In case of a Jackknife-bias Eq. (4.50) not negligible with respect to the error Eq. (4.49), the data should be checked more closely. A *bias-free* error analysis can be obtained by using the Double-Jackknife method, which in principle consists of the repeated application of the standard Jackknife process. Usually, the computational costs do not outweigh the minimal corrections in the error propagation.

We summarize: from the binning analysis the integrated autocorrelation time can be determined. Blocking the data into bins of a size significantly larger than the integrated autocorrelation time results in approximately statistically independent variables. Finally, we employ the jackknife method to obtain the errors of arbitrary combinations of measured observables.

4.4 Analytic continuation

Dynamical properties are described by spectral-functions – for comparison with experimental data (see App. A.4) and the identification of excitation energies, the analytic continuation to the real frequency axis is required. Maximum Entropy is currently the most sophisticated method for the ill posed inversion of QMC data.

4.4.1 The Maximum Entropy method

The Quantum Monte Carlo simulation provides Matsubara correlators for a discrete set of points $0 \leq \tau_l < \beta$ ($\tau_l = l\Delta\tau$, $l = 0, \ldots, L$), e.g.,

$$G_{\mathbf{k}\sigma} = \left\langle c_{\mathbf{k}\sigma}(\tau_l) c^\dagger_{\mathbf{k}\sigma}(0) \right\rangle \qquad \text{from} \qquad \mathrm{FT}(\left\langle \mathrm{c}_{\mathrm{i}\sigma}(\tau_\mathrm{l}) \mathrm{c}^\dagger_{\mathrm{j}\sigma}(0) \right\rangle) \; . \tag{4.52}$$

As already mentioned in Sec. 4.1.3 the spectral density or one-particle Green's function $A(\mathbf{k}, \omega)$ is related to the measured time-displaced Green's function G by

$$A(\mathbf{k}, \omega) = -\frac{1}{\pi} \operatorname{Im} G(\mathbf{k}, \omega) \; , \tag{4.53}$$

where the imaginary time-dependent Green's function at a specific momentum can be obtained via the spectral-theorem [92] through

$$G(\tau) = \int_{-\infty}^{+\infty} d\omega \; \frac{\mathrm{e}^{-\tau\omega}}{1 + \eta \, \mathrm{e}^{-\beta\omega}} \; A(\omega) \; . \tag{4.54}$$

Here, the kernel of the integral is defined with $\eta = +1$ ($\eta = -1$) for fermionic (bosonic) operators. From this we need to reconstruct the continuous function $A(\omega)$ in form of an

inverse Laplace transform. For a finite number of frequencies ω_i, $i = 1, \ldots, M$ on the energy-axis, equation (4.54) can be expressed in matrix form

$$\mathbf{G} = \mathbf{K}\mathbf{A} \quad \text{with} \quad G_l = \sum_w K_{li}\, A_i \quad \text{and} \quad K_{li} = \frac{\mathrm{e}^{-\tau_l \omega_i}}{1 + \eta\, \mathrm{e}^{-\beta \omega_i}} \,. \tag{4.55}$$

This leads to a system of linear equations with the vector $\mathbf{A}$ of size M ($\mathbf{K}$ must not be confused with the hopping matrix). Here, G_l is an $(L+1)$-vector holding the values of the single particle propagator at imaginary times τ_l, $l = 0, \ldots, L$. Owing to the form of the kernel K, the $(L+1) \times M$ matrix $\mathbf{K}$ exponentially suppresses the data of $\mathbf{A}$ for large frequencies ω as shown in Fig. 4.2. Consequently, the condition number (ratio of the largest to the smallest singular value) of the matrix is undesirably large – similar to the problem of stabilizing the matrix product given in Sec. 3.7.

Additionally, as a consequence of the finite number of field configurations generated, the data is afflicted with a statistical error. The inversion is therefore utterly ill posed due to the incomplete and noisy data. In 1990, Silver and others suggested the Maximum Entropy method (MaxEnt) [123, 124]. Standard likelihood analysis (χ^2-fitting) is inapplicable here, since many degenerate solutions lead to small χ^2, resulting in mathematically (numerically) correct, but physically useless data (noise). MaxEnt is based on Bayesian probability theory and provides logic as consistent theory. The method allows to input additional information like symmetries, sum rules and momenta into the reconstruction.

Within MaxEnt, the most probable solution for $A(\omega)$ for a given value of $G(\tau_l)$ (the aposteriori-probability) is obtained by maximizing

$$P\left(A(\omega)\middle|G(\tau_l)\right) \propto \mathrm{e}^{\alpha S - \chi^2/2} \,. \tag{4.56}$$

Here $\mathrm{e}^{\alpha S}$ is an a-priori-probability and $\chi^2 \propto P(G(\tau_l)|A(\omega))$ is the likelihood-function with the discrete kernel K_{li} of Eq. (4.54), defined by

$$\chi^2 \;=\; \sum_l \left(\frac{\sum_i K_{li} A(\omega_i) - G(\tau_l)}{\sigma(\tau_l)} \right)^2 \,, \tag{4.57}$$

$$\text{with} \qquad \sigma^2 = \frac{1}{N_m(N_m-1)} \sum_{l=1}^{N_m} \left(\langle \overline{G_l} \rangle - G_l \right)^2 \,. \tag{4.58}$$

N_m denotes the number of measurements of the Green's function G at time l, and S denotes the Shannon-Jaynes-entropy

$$S = \sum_i \left(A(\omega_i) - m_i - A(\omega_i) \ln \frac{A(\omega_i)}{m_i} \right) \Delta\omega \,. \tag{4.59}$$

Here m is the so-called default-model, which is usually chosen as a constant function (flat), but can also be defined by the atomic limit of the Hamiltonian or similar approximations. Note that any initial assumption biases the result!

There are several approaches to determine the regularization parameter α in Eq. (4.56) [86]. Maximizing the the aposteriori-probability in Eq. (4.56) is referred to as the *classical* method [125, 86]. The method results in the solution passing a χ^2-fit and having the least variation compared to the default model. Thus, it plays out the competition between the goodness-of-fit measure χ^2 and the entropy prior S. The MaxEnt-method requires careful analysis of variances and correlations of the input data to ensure trustworthy results.

The behavior for a model-case is illustrated in Fig. 4.3 showing the resolution and reliability of MaxEnt-reconstructions for different structures and errors. For each reconstruction a sample spectrum of two narrow Gaussians with varying weight-ratio and position was transformed with the kernel mentioned before and blurred by normally distributed random noise. In each plot we show the model and the MaxEnt reconstruction for artificial errors of $\mathcal{O}(10^{-2})$ and $\mathcal{O}(10^{-3})$. The insets show the corresponding Green's function on a logarithmic scale. We can identify the multiple peak structures by the different slopes of the correlation function. While for a single peak the Green's function decays nearly linearly, there are two slopes for two peak structures. The better the Green's function is defined at $\beta/2$, the more structure will be seen in the MaxEnt result. At high frequencies, the kernel suppresses the information exponentially, thus (even with large spectral weight) peaks can only be identified there with extremely accurate data.

As one can see, one can never be sure if an excitation from MaxEnt is a single peak, or an averaged bunch of multiple peaks. Excitations at high frequency are in general reproduced with minor peak height than they actually should have. There exist several different approaches to compute the MaxEnt results, e.g., with the help of integral corrections, Gaussians of fixed or variable width and many more. Although most of the approaches result in different peak structures, the deviation of their corresponding Green's functions from the input Green's function lie within the same range. Thus the different results can be seen as equivalent. We want to emphasize, that in general a *blurry* results can be seen as more trustworthy than an fine structured one. Consistent behavior along several k-vectors may also lend more credence to the results results.

In the following, shadeplots consisting of multiple MaxEnt results (corresponding to the different momenta) are shown with error bars. These bars indicate the uncertainty of the position of the peak-maximum and are obtained from the peak weights and slopes. Thus, they do not result from error-propagation directly, but represent a reasonable estimate.

MaxEnt is a sophisticated method for analysis of QMC-data, but not the one and only

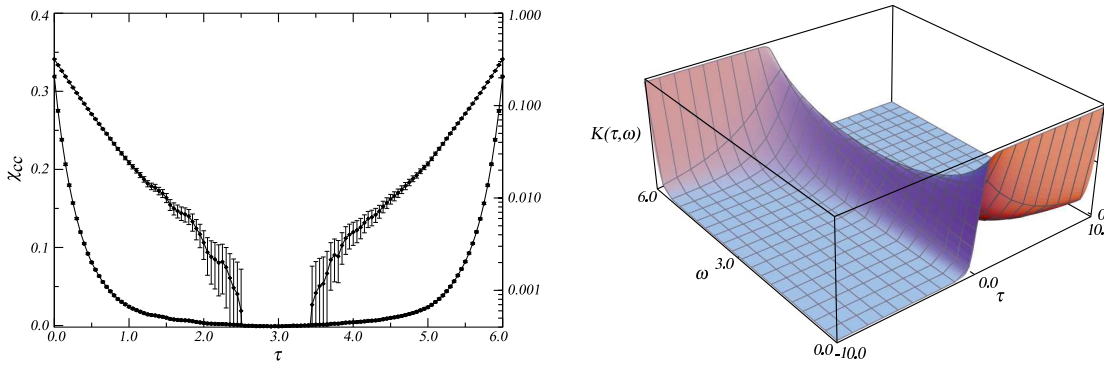

Fig. 4.2: Left: a typical bosonic (symmetric) two-point correlation function on a linear and a logarithmic scale. The gap in the logarithmic representation is due to negative values. Right: the kernel $e^{-\tau\omega}/(1+e^{-\beta\omega})$ for $\Delta\tau = 0.05$ and $\beta = 6.0$ showing the suppression of data-points with increasing ω. The manifold gets more sharp with increasing β.

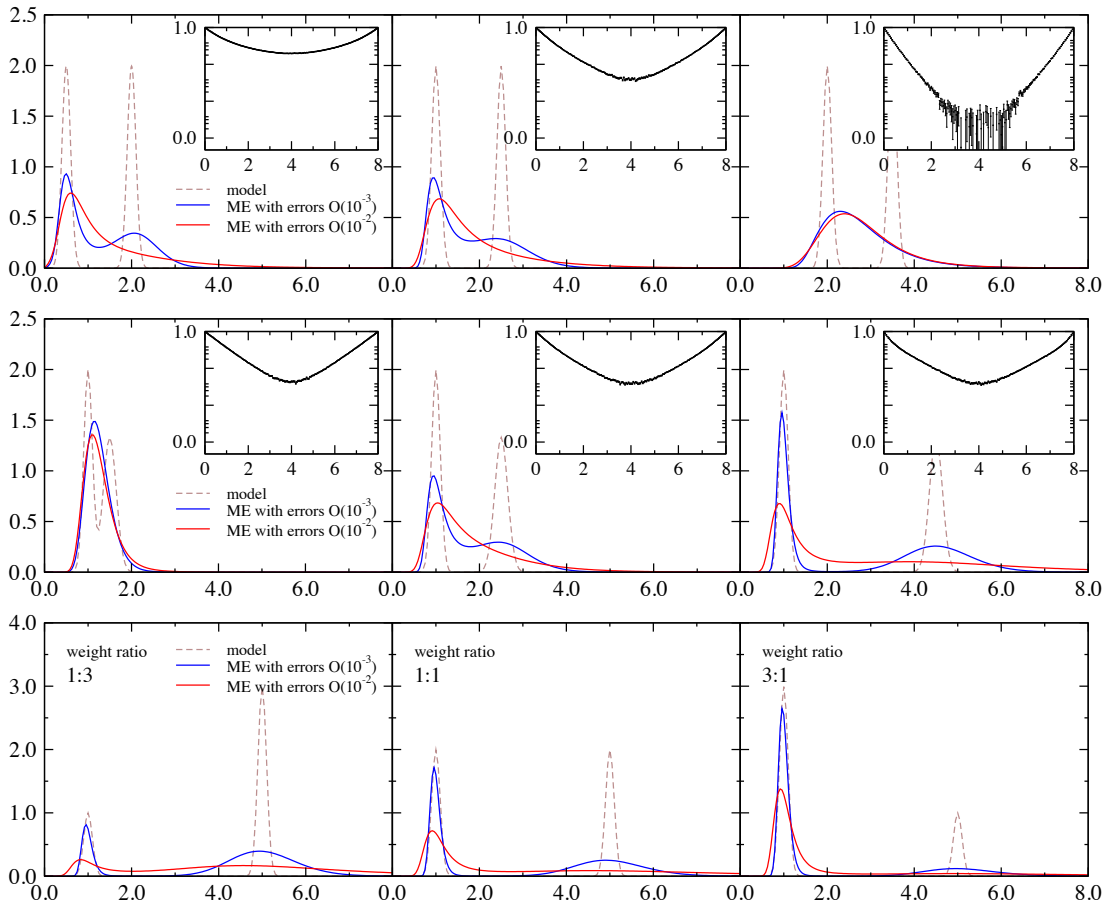

Fig. 4.3: MaxEnt results. Top: for two peaks with constant separation at increasing frequency position; Middle: for increasing separation of two differently weighted peaks; Bottom: for two peaks with different weight ratios. The insets show the Green's function with errors of $\mathcal{O}(10^{-3})$.

for analytic continuation: stochastic continuation [126, 127], the expansion into Chebychev polynomials (polynomial method) [128], or the computation of a cross-operator matrix using a variational Ansatz to determine the linear combination of kernel coefficients are other examples [129, 130, 131]. The latter might be a reasonable way to estimate gaps or a lower bound or low energy excitations in the spectral functions. Another interesting example is the Padé-approximation which is in general not suitable for noisy data, but found its appliance in the Hirsch-Fye Monte Carlo [132] using Gray-coding [133].

In this thesis we use the MaxEnt method and work with the MaxEnt-program by Danilo Neuber [134] who improved and corrected the program by von der Linden and Preuss [86, 125], which incorporates an improved evidence approximation to improve stability.

4.4.2 Additional information for the reconstruction

Additional information can be put into MaxEnt to improve the reconstruction. While the convergence of static observables can easily be tracked at runtime of the simulation, the question of the number of measurements necessary to obtain usable data for the imaginary-time-correlated Green's functions and the following Maximum Entropy process is more subtle. Sum rules and the first momenta of the Hamiltonian, which can be determined at high accuracy, additionally enhance the resolution.

Convergence and covariance-matrix

Despite the careful data analysis, the data points of the Green's function can be still correlated in imaginary time. To provide information about these correlations for the analytic continuation procedure, the covariance-matrix is computed [123]. The covariance-matrix for an observable $\mathcal{O}$

$$C_{\mathcal{O}} = \begin{pmatrix} c_{11} & c_{12} & \cdots & c_{1n} \\ c_{21} & c_{22} & \cdots & c_{2n} \\ \vdots & & \ddots & \vdots \\ c_{n1} & c_{n2} & \cdots & c_{nn} \end{pmatrix} \tag{4.60}$$

is symmetric $c_{ij} = c_{ji}$ with the variances of the observable on the diagonal $c_{ii} = \sigma^2_{\mathcal{O}}$. Given the expectation value of $\mathcal{O}$ by $\langle \mathcal{O} \rangle$ with the measurements $\mathcal{O}_i$ their correlation is given by the matrix-elements

$$c_{ij} = \mathrm{cov}(\mathcal{O}_i, \mathcal{O}_j) = \left\langle \left(\mathcal{O}_i - \langle \mathcal{O}_i \rangle\right) \left(\mathcal{O}_j - \langle \mathcal{O}_j \rangle\right) \right\rangle . \tag{4.61}$$

Taking the N measurements of the Green's function of the form

$$\overline{G}_l = \frac{1}{N}\sum_{n=1}^{N} G_l^{(n)} \ , \quad \text{and} \quad \overline{G_l G_{l'}} = \frac{1}{N}\sum_{n=1}^{N} G_l^{(n)}\, G_{l'}^{(n)} \ , \tag{4.62}$$

the corresponding covariance matrix is given by

$$\begin{aligned} C_{ll'} &= \frac{1}{N(N-1)}\sum_{n=1}^{N}\left(G_l^{(n)} - \overline{G}_l\right)\left(G_{l'}^{(n)} - \overline{G}_{l'}\right) \\ &= \frac{1}{(N-1)}\sum_{n=1}^{N}\left(\overline{G_l G_{l'}} - \overline{G}_l\overline{G}_{l'}\right) \ . \end{aligned} \tag{4.63}$$

The goodness-of-fit measure is then defined by

$$\chi^2 = \sum_{l,l'} \Delta G_l \, C_{ll'}^{-1} \, \Delta G_{l'} \ , \tag{4.64}$$

where ΔG_l is the same as in Eq. (4.57). The constraint through the covariance-matrix in the Maximum Entropy process is helpful, but has to be loosened by the definition of a lower limit for the covariance-matrix eigenvalues to omit singular values. Following the discussion by Preuss [86], a minimum of L and a suggestion of $\gtrsim 4L$ uncorrelated measurements are necessary to obtain a well defined covariance-matrix. Unfortunately the matrix is again afflicted by errors which would have to be taken into account. Preuss determined their influence to the reconstruction of the spectra by comparison of the exact errors and a fixed overall error. He concluded that accounting for the errors is more important than to know their exact values [125].

Hamiltonian moments

Similar to the constraint to fulfill sum-rules for the spectra, e.g., for purely electronic systems

$$\int_{-\infty}^{+\infty} d\omega \ A(\mathbf{k},\omega) = 1 \ , \tag{4.65}$$

or the demand for positivity, is the implementation of constraints for higher moments [135]. These can be incorporated through the default model or can be imposed as an additional constraint in the likelihood function [136]. The first moment is defined through the derivative of Eq. (4.54) with respect to τ by

$$\frac{d}{d\tau} G_\sigma(\mathbf{k},\tau_l) = \int_{-\infty}^{+\infty} d\omega \ (-\omega)\, \frac{\mathrm{e}^{-\tau_l \omega}}{1+\mathrm{e}^{-\beta\omega}} \ A(\mathbf{k},\omega) \ , \tag{4.66}$$

In Hubbard Hamiltonians the first momenta for $A(\mathbf{k},\omega)$ are given through relatively simple expressions. It can be shown [137] that the moments are given by

$$\mu_m = \int_{-\infty}^{+\infty} d\omega\ \omega^m A(\mathbf{k},\omega) = \left\langle \{[c_{k\uparrow}, \tilde{H}]_m, c_{k\uparrow}^\dagger\} \right\rangle , \tag{4.67}$$

where $\{\ ,\ \}$ denotes an anti-commutator and $[\ ,\ ]_m$ is a multiple (nested) commutator with $[a,b]_1 \equiv [a,b]$, $[a,b]_2 \equiv [[a,b],b]$, etc. and $\tilde{H}$ is the Hamiltonian in momentum space. Alternatively, the moments can be obtained via the Monte Carlo as expectation values of the form $\left\langle \frac{d}{d\tau} G(\mathbf{k},\tau_l) \right\rangle$, but they will be afflicted by similar (or more serious) errors as the Green's function. The extended Hubbard Hamiltonian from Eq. (2.7) in momentum space is given by

$$\begin{aligned} \mathrm{FT}\left(\mathrm{H_{EH}}\right) = \tilde{\mathrm{H}}_{\mathrm{EH}} &= \sum_\sigma \sum_k (-2\ t\ \cos(k) - \mu)\, c_{k\sigma}^\dagger\, c_{k\sigma} \\ &+ \frac{1}{N} \sum_{\sigma,\sigma'} \sum_{k,k',q} (\frac{U}{2}\ \delta_{\sigma,\sigma'} + V\ \cos(q))\, c_{k+q,\sigma}^\dagger\, c_{k'-q,\sigma'}^\dagger\, c_{k'\sigma'}\, c_{k\sigma} \end{aligned} \tag{4.68}$$

According to [135], the first three moments are

$$\begin{aligned} \mu_0 &= 1 \\ \mu_1 &= \varepsilon_k - \mu + \langle n \rangle \frac{U}{2} + \langle n \rangle \frac{V}{2} \cos(k) \\ \mu_2 &= (\varepsilon_k - \mu)^2 + \langle n \rangle (\varepsilon_k - \mu)\,(U + V\cos(k)) \\ &\quad + \frac{1}{2} \langle n \rangle \left(U^2 + V^2 \cos^2(k)\right) , \end{aligned} \tag{4.69}$$

with the tight-binding dispersion relation

$$\varepsilon_k = -2\ t\ (\cos(k_x) + \cos(k_y)) . \tag{4.70}$$

For two-particle correlators like charge-charge- or spin-spin-correlations only the first moment is given in simple form [86]

$$\mu_1(k) = 2\,(1 - \cos(k))\, E_{\mathrm{k}} , \tag{4.71}$$

where E_{k} denote the kinetic Energy.

All quantities taken in these expressions are exact or originate from stable MC estimators like the filling. Incorporating the n moments into the MaxEnt-reconstruction provides n additional equations for the system in Eq. (4.55), which definitely enhances the resolution. Higher moments include combinations of correlators and become rather complex. Due to their generally large errors the use of their implementation is limited.

Note that the error induced by the Trotter discretization alters the physics and that the analytically defined momenta do not necessarily correspond exactly to the simulated system. Thus, the influence of the moments in the MaxEnt process becomes exact for Trotter-scaling $\Delta\tau \to 0$ only. However, peak positions and their weights only vary slightly with increasing discretization steps.

A discussion of the moments for the extended Hubbard Holstein Hamiltonian (Eq. (2.7)) can be found in Ref. [135].

4.5 Finite size, symmetries and phase transitions

In this subsection we provide a short overview of the interpretation of the decay behavior and divergencies of correlation functions and order parameters in the context of global symmetries and their breaking. To derive the properties of a real physical system containing an almost infinite number of degrees of freedom from the insights of a small finite cluster is a delicate task. Finite-size effects have to be taken into account which can cause completely different physics on a finite system than in the infinite system.

Finite-size effects

Here, we give a few examples of effects which may occur in simulations due to finite system sizes. More details can be found in references [138, 67].

Shell effects and multiplet splitting – The allowed momenta of a small cluster form a coarse grid of points. Due to the point group symmetry of the finite lattice the noninteracting part of many microscopic models (e.g. the hopping part of the Hubbard model) then creates shells of degenerate momenta. Electron-electron interaction lifts the degeneracy of the ground state and creates a multiplet splitting which is completely a finite-size artefact. The numerically detected ground state then reflects many properties of the ground state multiplet, which means that the Fermi surface of the finite system might not be a good approximation for the thermodynamical limit, where it can appear very different.

Hidden symmetries of the Hamiltonian – It is not only possible that the infinite system shows a symmetry which the finite system does not show, but the inverse situation may also appear. For example, the ground state of the two-dimensional AF Heisenberg model has spontaneously broken symmetry ($SO(3)$ rotational symmetry is lifted). On the contrary, in the finite system, the total spin is still a good quantum number.

Broken symmetries – Short-range interactions may create order on the finite lattice and the correlation length becomes comparable to the system size, whereas this quantity

vanishes on the infinite lattice.

Finite-size gaps – Excitation gaps in the single particle spectral function or dynamic susceptibilities of a finite system are the rule rather than the exception because one is always comparing systems in which the densities differ by a finite amount and spatial correlation lengths cannot be infinite. Therefore, a gap obtained by a simulation is in general not an unambiguous criterion for insulating behavior.

Lifetime effects – Due to error afflicted correlation functions the restricted resolution in the analytic continuation process (see Sec. 4.4) does not allow definite identification of the the lifetime (peak witdh) of excitations. The identification is not only made difficult because of Maximum Entropy but also due to finite size effects which shift and squeeze excitations with varying lattice size. For this reason it is in general not possible to reliably deduce peak widths, damping rates and lifetimes from QMC or ED simulations without correct scaling analysis.

Boundary conditions – These have crucial influence on the result of the simulations, but become less important with increasing system size. QMC is rather weakly dependent on boundary conditions since it can handle rather large systems out of the box. DMRG instead builds up the system from small to large and may therefore strongly depend on the initial boundary conditions, which can lead to unwanted Weyl oscillations overlaying the results. As an example for the finite size effect in correlation functions at periodic boundary conditions we consider a spatial static correlation function $C(0, r)$ which decays to zero as the distance r goes to infinity (see Fig. 4.4). When measured on a finite one-dimensional chain of 8 sites, all r-points larger than 7 or smaller than 0 are mapped onto the range $0 \ldots 7$. Hence, the correlation function rises to maximum again when approaching the boundary, altering the decay of the correlation. For infinite correlation length this corresponds to a a polynomial function or to a hyperbolic (cosh) function otherwise. In case of a high order transition like a Kosterlitz-Thouless phase transition, the smooth change in the correlation length requires very large systems to get rid of finite size artefacts.

Finite-size scaling

Apart from these fundamental effects discussed in the preceding subsection one can expect that almost all physical quantities measured on a finite cluster exhibit some *smooth* transition as the system size is increased to the infinite lattice. The finite size artefacts may be expected to vanish systematically and can be eliminated by means of finite-size scaling.

The choice of the interpolating function (fit) to extrapolate to infinite lattice size is subtle, since one cannot be sure (even it seems unlikely) the behavior does not change

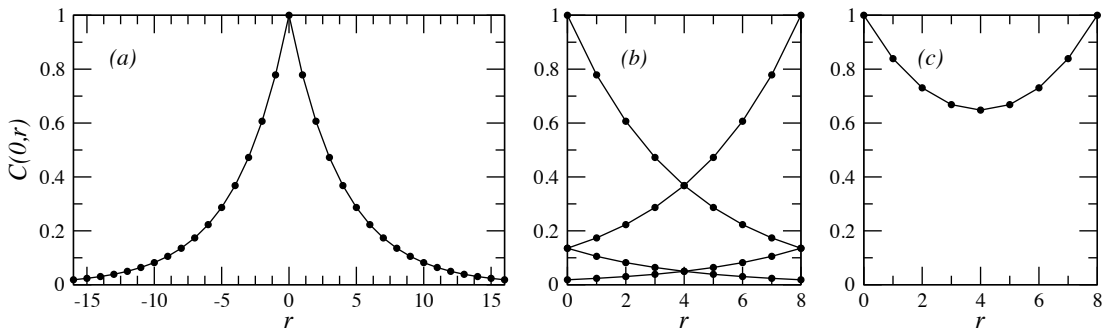

Fig. 4.4: Example of a correlation function on the (a) infinite lattice and its folding onto the (b) finite lattice with periodic boundary conditions; (c) shows the measured correlation function on a cluster with 8 sites. Lines are guides to the eye only.

any more in larger systems. But in general, a simple linear or exponential behavior yields a good approximation for the desired quantity on the infinite lattice. Fortunately, the scaling functions are known for some classes of models and can be determined by means of the renormalization group.

For finite-size scaling theory we refer to references [139, 67]. A discussion about the Trotter-time-scaling is given in App. A.1.

Cross-over, quantum- and thermodynamic phase transition

We are calculating all quantities at finite temperature – nevertheless, we are interested in the low energy excitations of the system. Is it justifiable to argue about these at finite temperature, and what temperatures are low enough to make trustworthy statements?

As several studies show [140, 141, 142], the charge disorder-order transition in the extended Hubbard model is a quantum phase transition. In the finite temperature QMC a disorder-order crossover is observed as a function of the inter-site Coulomb interaction V, and also as a function of the temperature T (inverse temperature β). Following the Mermin-Wagner theorem [53, 31], neither of them can be a true phase transition at finite temperature, due to the limited dimensionality of the ladder. While for small systems the ladder might be seen as a two-dimensional object, in the thermodynamical limit in form of an infinite long ladder, the finite dimension along the rungs plays a minor role and a phase transition is confined to zero temperature. Nonetheless, this dimension cannot be fully neglected and does influence the dynamics of the ladder. The observed transition in β is therefore identified as a finite size effect [143, 144].

In order to understand the transition in V, we quote three kinds of transitions com-

mon in the literature [145, 146]:

(i) A *quantum phase transition* (QPT) is strictly defined for $T = 0$. In general, it is a sharp transition, as a consequence of triggering the relative strength (or any non-thermal parameter) of two non-commuting operators. Neither of them needs to favor a broken symmetry – thus a QPT will not necessarily imply the formation of long range order (Goldstone mode) of any kind. In solid-state physics the QPT is the competition between potential and kinetic energy. Gaps in excitations remain robust and do not vanish in the presence of other excitations.

(ii) The competition in the *thermodynamic phase transition* (TPT) occurs between internal energy and the entropy of the system as a function of the temperature and incorporates the breaking of a symmetry. Excitation gaps are soft and can be overcome at temperatures where thermic fluctuations are larger than the gap size.

(iii) *Crossover* is the name for the change of an order parameter as a function of any parameter in finite systems and finite temperature at a dimensionality for which the Mermin-Wagner theorem [53, 31] prohibits a true phase transition. This apparent *phase transition* vanishes in the thermodynamic limit and can (but does not have to) be the aftermath of a quantum critical p

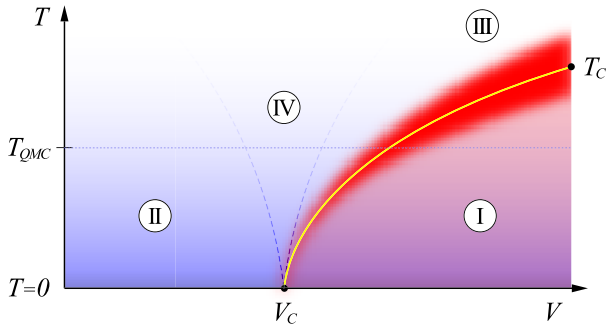

Fig. 4.5: The quantum critical point at $T = 0$ and V_c is accompanied by a thermodynamic phase transition (cross-over) from disorder region (II) to order region (I) for finite temperatures up to a critical temperature T_c. The cross-over red-shaded-region at the order-disorder phase boundary can be the environment for a true phase transition (solid line at phase boundary) leading in the limit to the quantum critical point V_c. Adapted from Ref. [145].

To distinguish between TPT and QPT in non-relativistic simulations means to clarify the situation of transition as a function of temperature and a transition any other non-thermal parameter. Though, the contrast to the classical phase transition is that the statics and dynamics of the quantum system are inextricable linked. This is because the quantum Hamiltonian at some imaginary time does not commute with the Hamiltonian

at another imaginary time.

In Fig. 4.5 a schematic phase diagram for a model-Hamiltonian which shows a QPT is given. The model in $d > 1$ dimensions has a TPT at some finite temperature T_c driven by thermal fluctuations. For $T_c(V) \neq 0$, critical fluctuations in the vicinity of the phase boundary between quantum ordered phase (I) and quantum disordered phase (II) are classical. This is due to the diverging correlation time τ_c which is proportional to the diverging correlation length in imaginary time ξ_τ

$$\tau_c \propto \xi_\tau^z \propto |t_r|^{-\nu z} \,, \tag{4.72}$$

at the transition line, with ν, z as the critical exponent, the dynamic critical exponent and the reduced temperature $t_r = |T - T_c|/T_c$, respectively.

This classical critical regime (dark gray region) becomes narrower with decreasing temperature, shrinking to zero at finite strength of coupling V at zero temperature. In this quantum critical point V_c the dynamic critical exponents can be expressed by those of a corresponding $d+1$-dimensional classical model and correlations obey power laws. The transition line separates the phase space into region (I), where long range order exists and region (II), where quantum order is dominantly broken by quantum fluctuations and region (III) which is dominated by thermal fluctuations. Between the quantum disordered and the thermally disordered regions, where both quantum and thermal fluctuations are relevant, there is an intermediate region (IV) called quantum critical regime [147, 148, 146, 145].

As it seems that a QPT can be generically mapped onto a classical counterpart, we want to note that *not all* properties of a given quantum system can be obtained from its classical counterpart! Some theories for quantum systems involve long-ranged effective interactions arising from soft modes, real-time dynamics analysis (phase coherence time) or a strong space-time anisotropy, which in general cannot be treated by simple mapping. For an instructive review on the topic of QPT we refer the reader to [145].

The schematic phase diagram for our quasi-one dimensional ladder looks similar to the one sketched in Fig. 4.5, except for the solid line marking the TPT between T_c and V_c and the point T_c itself (but with the dark gray region), since this transition would vanish in the thermodynamical limit. Obviously, the transition within this Monte Carlo study is a cross-over.

In order to estimate which finite temperature is low enough in our simulation to identify electronic (phononic) effects we compare the thermal and electronic (phononic) fluctuations. In units $\hbar = k_\mathrm{B} = 1$ we have the energy $E = T = \frac{1}{\beta}$. In other words, for e.g. $\beta = 6/t$ we should be able to resolve structures of electronic excitations of energies or frequencies down to $t/6$, where t is the hopping amplitude. Usually global structures can still be identified at much higher temperatures.

Backed with adequate computer power, any finite temperature simulation can be used for groundstate investigations of a QPT as long one knows the critical exponent z. As one utilizes space-time proportionality to scale the temperature with the system size in a ratio which conserves critical behavior for a fixed coupling, the scaling limit is not only the infinite cluster case, but the zero temperature case as well.

Decay behavior, symmetry breaking and Goldstone modes

In general, correlation functions decay with exponentially decreasing amplitude, which reflects the finite correlation length equivalent to short-range order. In the case of a term with finite interaction in the Hamiltonian, but correlations are decreasing obeying a power law, the diverging correlation length indicates a phase transition.

According to Goldstone's theorem [149, 150], spinless bosons with zero mass appear when a continuous symmetry is spontaneously broken. The Goldstone bosons appear whenever a continuous symmetry group leaves the Hamiltonian but not the vacuum (ground-state) invariant. These may be seen as additional degree of freedom compensating for the broken symmetry and guaranteeing a theory with equal number of degrees of freedom in the unbroken as well as in the broken phase. Their zero mass reflects the formal definition of the spontaneous symmetry breaking (SBB) where any broken state in the same symmetry group can be obtained with vanishing energy effort. SSB means that an order parameter m_{order} does not commute with the Hamiltonian. It is formally defined in the limit of an external field h

$$\lim_{h\to 0^+} \lim_{N\to\infty} m_{\text{order}} \neq 0 \; . \tag{4.73}$$

The number of Goldstone bosons is given by the number of broken generators of the system's symmetry group. In solid state theory these gapless excitations can be density waves – non-local excitations (local in k-space). In the classical picture of a vector-model this can be understood as twisting the local spin orientation of the spins so that they precess around the z-axis with a phase difference. This may be interpreted as an excitation of particular momentum and energy passing through the crystal like a plane wave similar to a phonon.

As a matter of fact a divergent correlation length in space is evident in time as well. In the dynamical spectra this can be seen by the appearance of a zero frequency Goldstone mode in form of a peak at a certain momentum. Only finite size scaling to the thermodynamical limit or numerical renormalization group (NRG) studies allow to determine whether the decay behavior is of exponential or algebraic kind marking short range order, or a true phase transition and long range order (LRO), respectively. A diverging correlation function (e.g. spin-spin correlation S_{ss}) at some wave vector $\bar{\mathbf{q}}$

results in vanishing energy

$$\lim_{\mathbf{q}\to\bar{\mathbf{q}}} \chi_{\mathrm{ss,cc}}(\bar{\mathbf{q}}) \to \infty \qquad \longrightarrow \qquad \lim_{\mathbf{q}\to\bar{\mathbf{q}}} E(\mathbf{q}) = 0 \,. \tag{4.74}$$

This means a divergence at some wave vector $\bar{\mathbf{q}}$ possibly indicates Goldstone bosons. Note, while a Goldstone Boson is a gapless excitation it does not rely on LRO – LRO does not necessarily imply a spontaneously broken symmetry! One distinguishes between *true* LRO and *quasi* LRO. Where true LRO implies the bijective relation of SSB and a power law decay of the correlation functions, quasi LRO does not include the spontaneous breaking of a continuous symmetry. The formal definition of LRO is given by

$$0 \neq m^2 = \lim_{r\to\infty} \lim_{N\to\infty} \left\langle s_i s_{i+r} \right\rangle \,, \tag{4.75}$$

where the s_i, s_{i+r} represent arbitrary operators separated in space by r. An overview to rigorous theorems, symmetry breaking and finite size effects in quantum many-body systems (on the lattice) is given by Koma and Tasaki in [138].

We want to point out that SSB is not defined for finite systems. Thus to conclude from a finite system to the existence of SSB in the thermodynamical limit is a rather difficult task.

5 Results

Equipped with a suitable method and numerous tricks we simulate the system – the two legged, quarter-filled ladder as a model for the sodium vanadate. Spectral functions, susceptibilities, static correlation functions and observables will be discussed below and above the charge order transition as a function of the inter-site Coulomb repulsion V.

The parameters of the extended Hubbard model specific for the sodium vanadate are fixed in the following plots. Namely, the onsite coupling repulsion $U = 8.0$ and the hopping $t_a = 1.0$, $t_b = 0.5$ perpendicular and along the ladder, respectively (see Sec. 2.8). The chemical potential μ has been adjusted such that the system is quarter-filled $\langle n \rangle = 0.5$. As explained in Sec. 4.2 due to the severe sign problem we simulate the pure extended Hubbard model without coupling to lattice degrees of freedom. If not indicated otherwise, lines between data-points are guides to the eye only.

5.1 Static quantities

In this section we compare with results from Gabriel and coworkers [151]. The simulation used an approximation to reduce the number of auxiliary fields necessary for the treatment of the inter-site coupling as described in Sec. A.3.

From the parallel tempering we obtain results for simulations with slowly changing inter-site coupling V. In Fig. 5.1 we plot the quadratic charge order parameter m_{CO} defined in Eq. (4.16) as a measure for the amount of zig-zag charge order for ladders of $N_x = 8, 16, 32$ rungs. The crossover from the disordered phase to the charge-ordered phase is smooth but sharpens with increasing system size (ladder length). Though in the thermodynamical limit $N_x \to \infty$ the shape seems to become very sharp it is still no phase transition due to the finite temperature (see Sec. 4.5)! In Fig. **??** the crossover as a function of temperature is shown. With decreasing temperature the order parameter converges for a specific coupling V. As our results are computed for $\beta = 8.0$ we expect the order parameter to be mostly converged, thus the crossover in Fig. 5.1 should not

shift with decreasing temperature much further. At high temperatures (small *beta*) the order decreases for a fixed coupling V, thus the crossover point in Fig. 5.1 shifts towards larger values of V with increasing temperature as sketched in Fig. 4.5. The dashed line in Fig. 5.1 represents the zero temperature ($\beta \to \infty$) result for an extrapolated infinitely long ladder taken from Ref. [143]. For $T = 0$ the transition of the order parameter is a true quantum phase transition as a function of the coupling V and occurs at the critical coupling $V_c = 2.1(1)$ [143].

In Fig. 5.3 and Fig. 5.4 the changes of (negative) kinetic and potential energy per site with increasing V are plotted. Both decrease with increasing V. This corresponds to the classical interpretation that the electrons in the charge ordered phase are frozen in zig-zag order where they would neither contribute the energy $\sim U$ for double occupancies nor the energy $\sim V$ in presence of nearest neighbors to the energy (compare with illustration Fig. 1.2). Their shapes show only weak finite size dependence.

The charge correlation length plotted in Fig. 5.5 increases exponentially with a V depending slope. This behavior is consistent with the 1D Ising model in a transverse field (IMTF) [151, 152], which is equivalent to the extended Hubbard Hamiltonian in Eq. (2.2) in the limit of one spinless electron per rung. For large V, the transverse field goes to zero, and $\xi_{\mathrm{IMTF}} = |\ln \tanh(\beta)|^{-1}$. This is exponential behavior with slope 2 which the data for $V = 3.0$ appear to approach. Long range order is only established in the thermo-dynamical limit. For weaker coupling $V < 2.0$, the correlation length IMTF remains finite even in the limit $\beta \to \infty$ which means disorder even at $T = 0$.

The static spin-spin Fig. 5.6 correlations exhibit antiferromagnetic order probably resulting from partial charge order where one electron is delocalized on one rung. The order appears to be short ranged not only at finite temperature but also at zero temperature investigations [142]. The effective antiferromagnetic coupling between neighboring sites becomes smaller the larger V gets. The antiferromagnetic behavior along the ladder will be discussed in more detail below.

5.2 Single-particle particle Green's function

The single-particle spectral function defined in Eq. (4.28) corresponds to the low energy band-structure of our strongly correlated model. Results are shown in several figures below: the intensity of the shading (or peak height in line-plots) reflects the probability to find an electron inserted (removed) at specific energy ω and momentum $\mathbf{k}$ into (from) the system. The following spectra consist of the momentum range from $(k_b, k_a) = (0, 0)$ to $(\pi, 0)$ and from $(0, \pi)$ to (π, π).

We follow the argumentation by Aichhorn et al [142] and compare some distinct

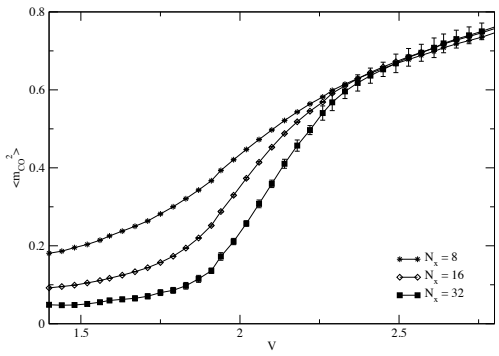

Fig. 5.1: Zig-zag order parameter versus inter-

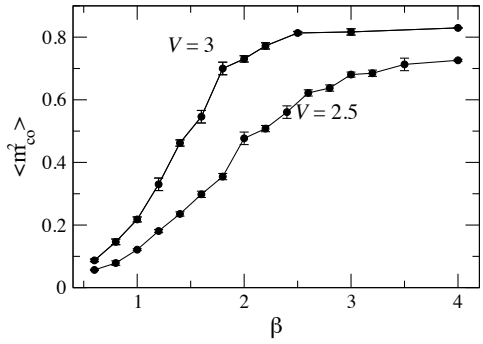

Fig. 5.2: Zig-zag order parameter versus inverse temperature for a $N_x = 32$ ladder taken

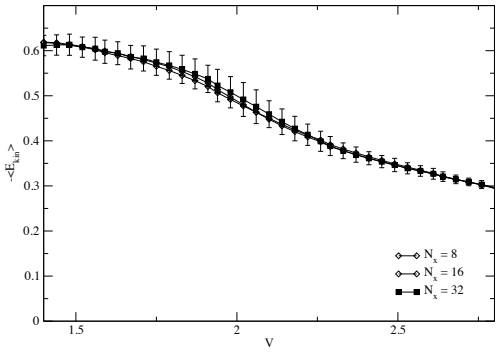

Fig. 5.3: Kinetic energy per site versus inter-site coupling for ladders of $N_x = 8, 16, 32$ rungs at $\beta = 8.0$. The visible error bars belong to the largest ladder.

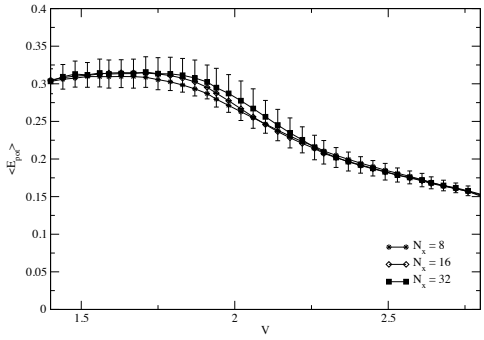

Fig. 5.4: Potential energy per site versus inter-site coupling for ladders of $N_x = 8, 16, 32$ rungs at $\beta = 8.0$. The visible error bars belong

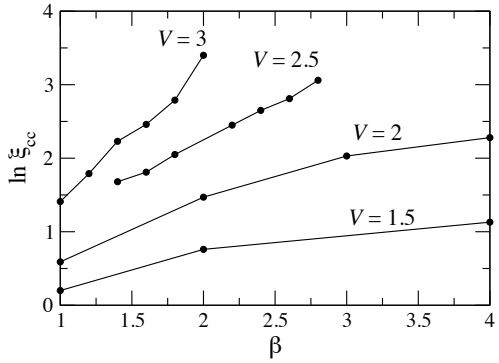

Fig. 5.5: Logarithm of the charge-correlation-length versus inverse temperature for different inter-site couplings for a $N_x = 32$ ladder. The figure is taken from Ref. [151] and gives a hint to the establishing of long range charge order at $\beta \to \infty$.

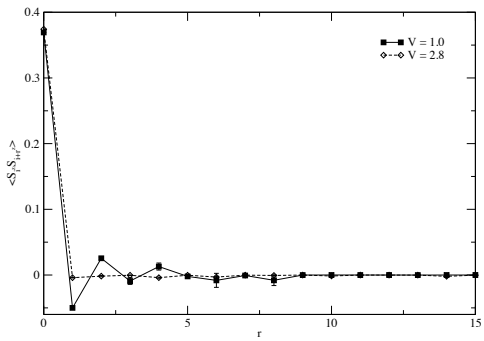

Fig. 5.6: Spin-spin correlation as a function of distance for a $N_x = 32$ ladder showing short range correlations for $V = 1.0$

features with their ED+CPT study of the quarter-filled 6×2 ladder. We also compare to the Hubbard chain (see Sec. 5.5) to show the nearly one-dimensional behavior of the ladder system.

Disordered phase

We start our investigations in the disorderd phase. We choose the inter-site coupling with $V = 1.0$ which is far off the crossover-point. Let's focus on the excitations with $k_a = 0$ (along the ladder) in Fig. 5.7 first. We have a heavy weighted lower Hubbard band and vanishing spectral weight in the upper Hubbard band. The dispersion is only slightly pronounced due to the small hopping integral along the ladder and has a period of π just like in the half-filled 1D Hubbard model. Consequently, the electrons (holes) have large effective mass.

The dispersion looks similar to half-filled one-dimensional (1D) Hubbard model with $t = 0.5$ shown in Fig. 5.20 with the big difference of a much larger gap. The small gap of the ladder $\Delta_{\mathrm{Q1D}} \approx 1.0$ where in the Hubbard chain we have $\Delta_{\mathrm{1D}} \approx 6.0$. The gap is responsible for insulating behavior since there are no excitations at the Fermi-level ($\omega = 0.0$) which would contribute to the charge-conductivity. In the extended Hubbard ladder the gap compares well to ED results by Aichhorn et al [142]. It remains finite for $V = 0$ and gets larger with increasing V. This can be seen in the charge compressibility as well. For a wide range of the chemical potential the filling stays constant. The region broadens with increasing V as plotted in Fig. 5.9. Near $k_b = 0, \pi$ there is large spectral weight and scattering from short range antiferromagnetic correlations can become most effective. Therefore the doubling of the unit cell along the ladder in b direction is an effect of antiferromagnetic order along the legs.

Aichhorn et al stress to find traces of spin-charge separation (see App. A.3) near $k_b = 0, \pi$. Due to the limited resolution of the MaxEnt reconstruction spin charge separation cannot be identified from the spectral function. The effect should be most likely seen near $k_b = 0, \pi$ where the band splits into a low energy spinon-branch and a holon-branch at slighty higher energy.

Traces of structures can be found at $k_b < \pi/2,\ \omega > 0.0$ and $k_b > \pi/2,\ \omega < 0.0$ which can look like reflections of the bands at the Fermi level. These so-called shadow bands can form in the presence of strong antiferromagnetic correlations and can be seen remnants of a magnetic superstructure that would be generated by the halving of the Brioullin zone in a long-ranged antiferromagnetic ordered state. Additional features like excitations at energies corresponding to double occupation presumably around ω=8.0-10.0 are not visible and are probably suppressed by the MaxEnt kernel.

For $k_a = \pi$ (Fig. 5.8) no spectral weight at all can be found for inverse photo-emission

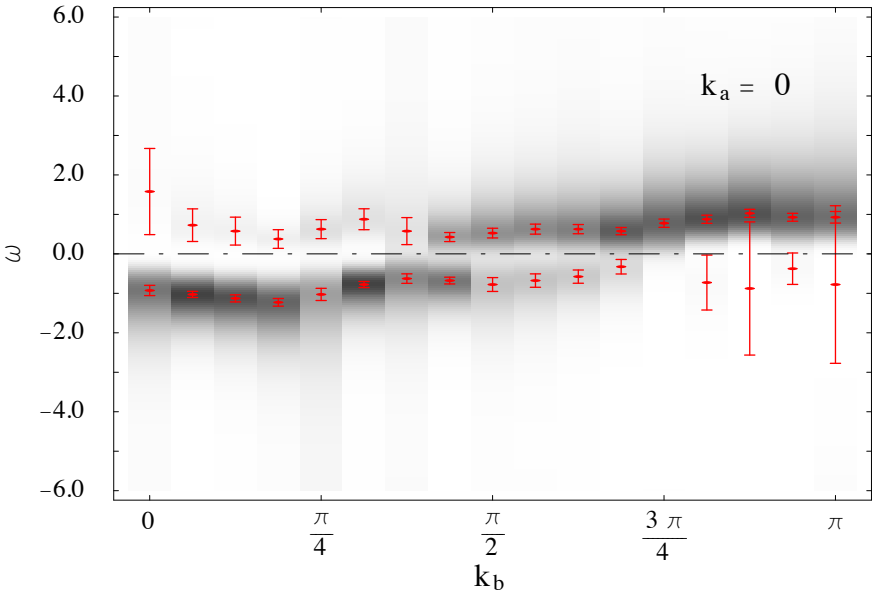

Fig. 5.7: Single-particle spectral function $A(\mathbf{k}, \omega)$ of the quarter-filled 32×2 ladder system in the disordered phase at $V = 1.0$ along the ladder with $k_a = 0$.

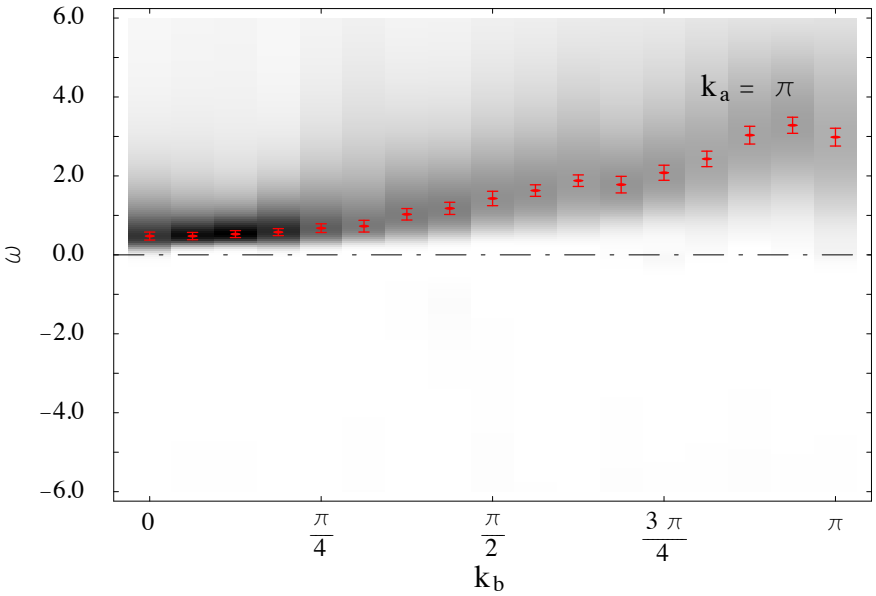

Fig. 5.8: Single-particle spectral function $A(\mathbf{k}, \omega)$ of the quarter-filled 32×2 ladder system in the disordered phase at $V = 1.0$ with $k_a = \pi$.

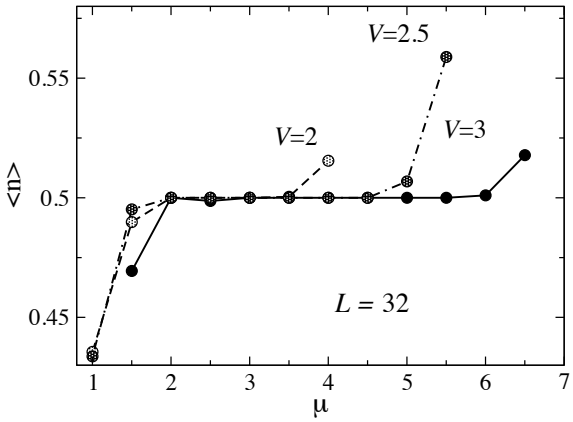

Fig. 5.9: Filling versus inter-site coupling for a $N_x = 32$ ladder reflecting the charge gap dependence for different V values.

or hole excitations below the Fermi level ($w < 0$). This implies that there can be only negligible occupation of the channel. This scenario can be understood as we know the momentum $k_a = \pi$ corresponds to an anti-bonding state within a rung which has energy $2t_a$ relative to the bonding orbital. Therefore, this state is unlikely to be populated even at finite temperature.

The primary excitations for $k_b < \pi/4$ have large spectral weight compared to the $k_a = 0$ channel. Qualitatively this can be understood as follows. If an electron with momentum $k_a = 0$ is inserted it will most probably occupy a bonding state. One of the two possible states is already occupied therefore it is necessary that the electrons have opposite spin and the electron will couple to the anti-ferromagnetic background. A particle inserted with momentum $k_a = \pi$ instead would occupy the anti-bonding orbital. Since both spin directions posses equal probability it will not be influenced by the anti-ferromagnetic background. Therefore the band with $k_a = \pi$ disperses with period 2π.

Charge-ordered phase

As we set the inter-site Coulomb repulsion to $V = 2.8$, which is deep in the charge-ordered sector, the spectral function changes drastically. The peaks become much sharper mostly because of the better statistics due to the minor sign problem in the charge-ordered phase. As predicted the gap broadenes with increasing V. In the channel $k_a = 0$ (Fig. 5.10) we have little spectral weight for $\omega > 0$ with a dispersion of periodicity 2π. Below the Fermi level most of the weight is located near $\pi/4$. The band shows only vanishing dispersion. In a semi-classical picture we can describe the situation as follows.

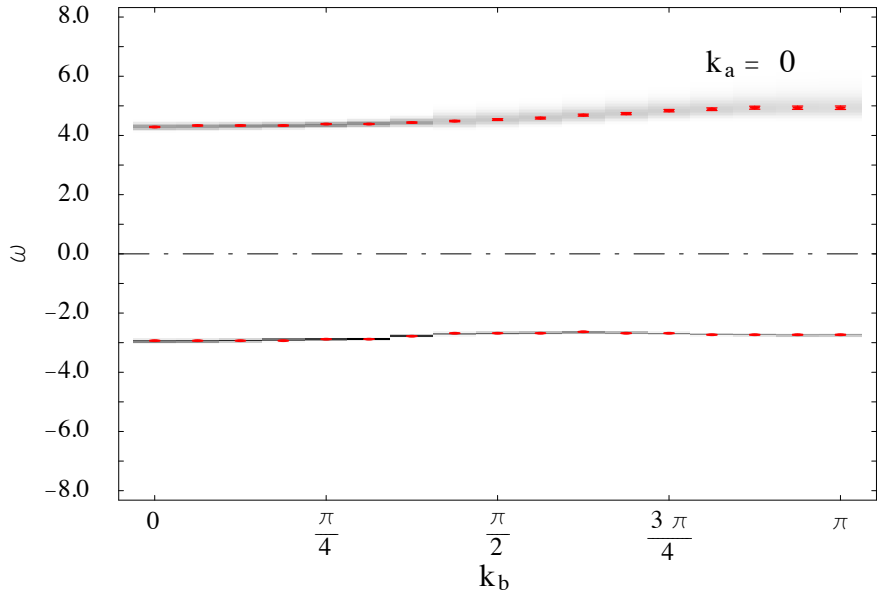

Fig. 5.10: Single-particle spectral function $A(\mathbf{k}, \omega)$ of the quarter-filled 32×2 ladder system in the charge-ordered phase at $V = 2.8$ along the ladder with $k_a = 0$.

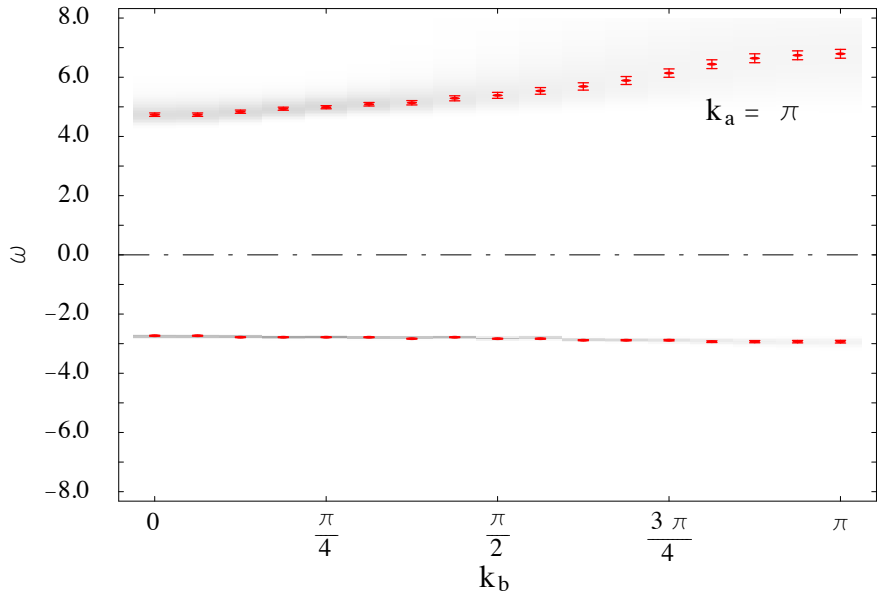

Fig. 5.11: Single-particle spectral function $A(\mathbf{k}, \omega)$ of the quarter-filled 32×2 ladder system in the charge-ordered phase at $V = 2.8$ with $k_a = \pi$).

Let's assume we have a perfectly zig-zag ordered charge pattern. If we put in an electron with specific momentum either on an occupied or empty site, this *costs* high amounts of potential energy from double occupancies and nearest neighbor repulsion even when the electron is delocalized. If we remove an electron out of the ordered pattern no potential energy has to be paid and hole and electron can delocalize at least over the nearest neighbor sites gaining kinetic energy. Thus inverse photo-emission is energetically more favorable.

Compared to the channel $k_a = 0$ the channel $k_a = \pi$ (Fig. 5.11) has only minor weight. It shows a similar dispersion as the $k_a = 0$ channel but a bit more pronounced for $\omega > 0$. With this momentum both, photo-emission and inverse photo-emission seem to posses equal probability.

5.3 Spin susceptibility

Here the spin-response to an outer perturbation at specific energy ω and momentum $\mathbf{k}$ is probed. The spin susceptibility and the charge susceptibility defined in Eq. (4.32) yield information about their contribution to the low energy excitations. We compare the results for the quarter-filled 32×2 ladder with the results of the ED study of the quarter-filled 8×2 ladder by Aichhorn et al [141].

Disordered phase

In the introduction to the sodium vanadate we have mentioned that the compound above the charge-order transition can be described by an effective antiferromagnetic $S = 1/2$ Heisenberg chain. This can be understood as the magnetic structure of the sodium vanadate consisting of a single electron per rung where the rungs form a chain of spins $S = 1/2$. Indeed for $k_a = 0$ in Fig. 5.12 we find a gapless spinwave dispersion similar to that of the antiferromagnetic $S = 1/2$ Heisenberg chain in the spin susceptibility. Doubly occupied states which usually contribute significantly to the magnetic response in Mott-Hubbard insulators, have only little influence in our case since they are very improbable ($\approx 5\%$ double occupation). The quasi-one-dimensional magnetic behavior of the ladder model has been also affirmed in Ref. [141].

The effective antiferromagnetic coupling for the $S = 1/2$ Heisenberg chain can be extracted from the spin dispersion using [153]

$$J_{\text{eff}} = \frac{2}{\pi}\omega(0, \pi/2) \approx 0.45 \; . \tag{5.1}$$

A quantitative with experimental data cannot be made since in the experiment the ordering and, correspondingly, J_{eff} is traced as a function of temperature for given other

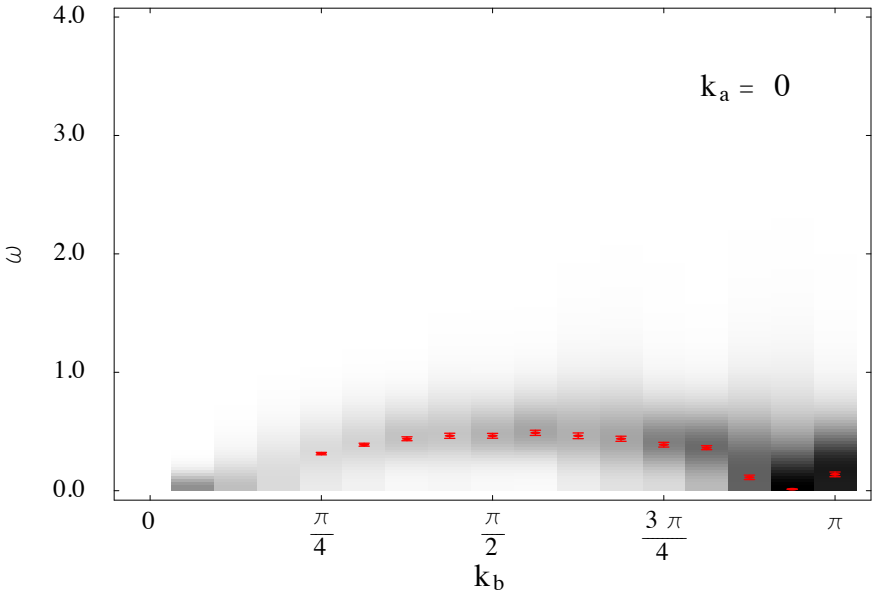

Fig. 5.12: Spin susceptibility $\chi_S(\mathbf{k}, \omega)$ of the quarter-filled 32×2 ladder system in the disordered phase at $V = 1.0$ along the ladder with $k_a = 0$.

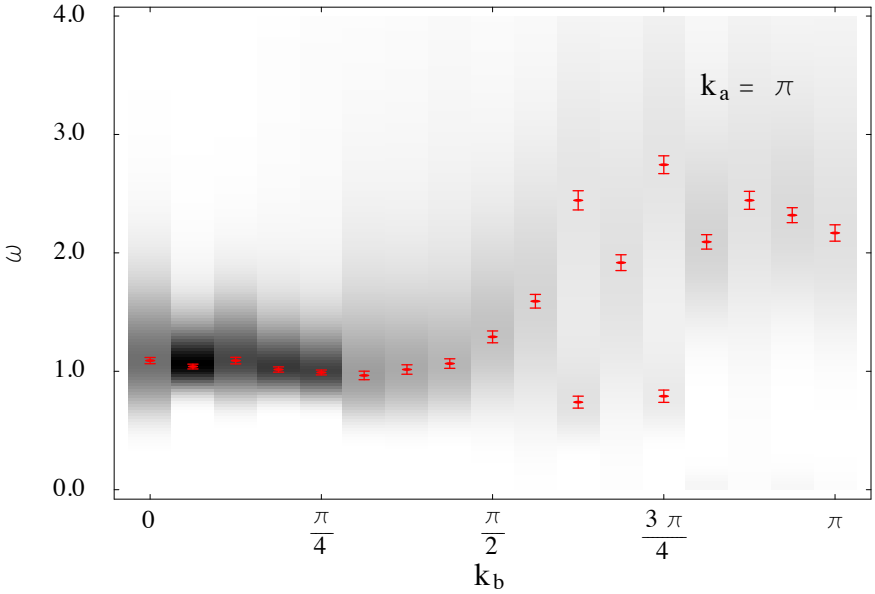

Fig. 5.13: Spin susceptibility $\chi_S(\mathbf{k}, \omega)$ of the quarter-filled 32×2 ladder system in the disordered phase at $V = 1.0$ with $k_a = \pi$).

system parameters while we investigate the ordering at a fixed temperature as a function of the extended Hubbard repulsion V.

The spin-wave picture compares well to the behavior of the spin susceptibility of the half-filled Hubbard chain with $t = 1.0$ shown in Fig. 5.21 where an effective coupling of $J_{\text{eff}} \approx \frac{4t^2}{U}$ can be derived from perturbation theory. Note that this hopping is twice as large as $t_b = 0.5$! Thus the magnetic behavior cannot be reproduced by the half-filled Hubbard chain with $t = 0.5$ but rather with a larger transfer integral $t \approx 1.0$. Though the comparison with the Hubbard chain confirms the one-dimensional behavior.

At $k_a = \pi$ (Fig. 5.13) the primary excitations can be found at higher energies $\omega \approx 1.0$. The gap in the spin spectrum is very close to the charge gap (Fig. 5.17) indicating that it is probably due to charge excitations. As Aichhorn et al [141] confirm this interplay between spin and charge excitations which is similar to the charged magnons picture introduced in Ref. [154] for interpretation of the infrared absorption spectra of NaV_2O_5.

Charge-ordered phase

In the charge-ordered phase the dispersion of both channels $k_a = 0, \pi$ in Fig. 5.14 and Fig. 5.15 are reduced to the dark shaded line near $\omega \approx 0$. Under the assumption that the shaded area is the upper limit for maximum spin excitation at $\pi/2$ then we find the effective magnetic coupling to be $J_{\text{eff}} < 0.06$ which is in agreement with perturbation results in Ref. [38] which yield $J_{\text{eff}} \approx 0.04$.

The $k_a = \pi$ channel additionally exhibits excitations of negligible weight at $\omega > 0$ indicated by their error bars for which one cannot make a reliable statement.

5.4 Charge susceptibility

For the discussion of the charge susceptibility we directly oppose the spectra of the disordered phase (Fig. 5.16 and Fig. 5.17) and the spectra of the charge-ordered phase (Fig. 5.19 and Fig. 5.19).

In both regimes the spectra exhibit a qualitatively similar dispersion which is nearly constant with minor weight in the $k_a = 0$ channel and a cosine-like dispersion in the $k_a = \pi$ channel. Since dominant weight is only in the latter one let us focus on this channel with $k_a = \pi$.

While there is an excitation gap of $\Delta\omega \approx 1.0$ in the disordered phase, we have a gapless excitation at $\mathbf{k} = (\pi, \pi)$ in the charge-ordered phase. Compared with Fig. 5.7 the charge gap $\Delta\omega$ coincides with the gap in the single-particle spectral function. This

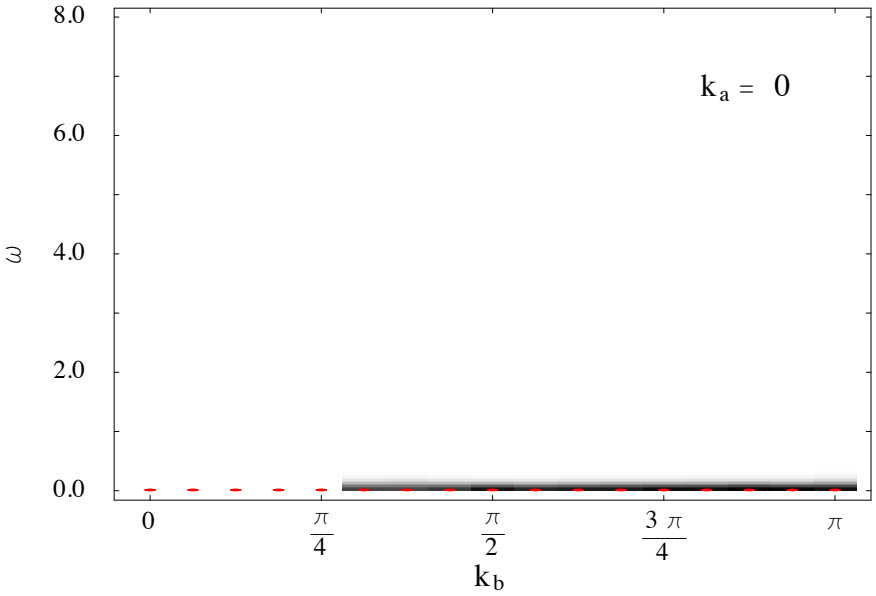

Fig. 5.14: Spin susceptibility $\chi_S(\mathbf{k}, \omega)$ of the quarter-filled 32×2 ladder system in the charge-ordered phase at $V = 1.0$ along the ladder with $k_a = 0$.

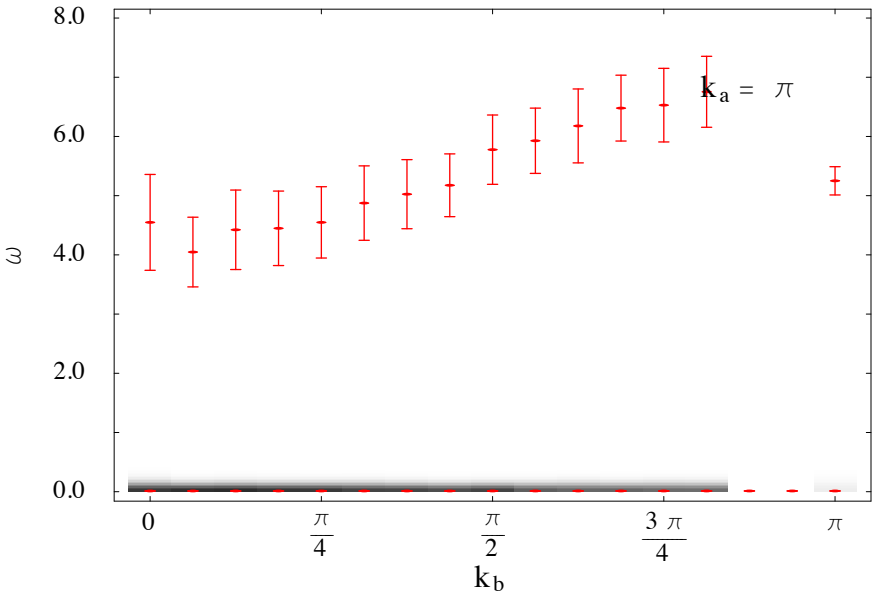

Fig. 5.15: Spin susceptibility $\chi_S(\mathbf{k}, \omega)$ of the quarter-filled 32×2 ladder system in the charge-ordered phase at $V = 1.0$ with $k_a = \pi$).

confirms that there are no electronic excitations at the Fermi-level which corresponds to the insulating behavior.

The gapless excitation at $\mathbf{k} = (\pi, \pi)$ in Fig. 5.15 is the direct effect of the zig-zag charge order since the vector (π, π) in k-space corresponds to the zig-zag pattern in real space. This peak is of $\mathcal{O}(10^3)$ higher than the other structures in the spectrum and has been cut-off at a specific intensity. This *divergence* marks the braking of the discrete translation symmetry because of the two possible zig-zag charge-patterns. The additional peak at the same vector is probably shifted in the MaxEnt reconstruction due to the dominant weight of the gappless excitation. As discussed this is probably a finite size effect which should vanish in the thermodynamic limit.

5.5 Comparison with the half-filled Hubbard chain

For the discussion of the spectra in this chapter we referred to the one-dimensional Hubbard model at half-filling. In the figures 5.20, **??** and 5.21 the single-particle spectral function for $t = 0.5$ and the spin susceptibilities for $t = 0.5$ and $t = 1.0$ are plotted for the same temperature $\beta = 8.0$ as used for the discussed spectra.

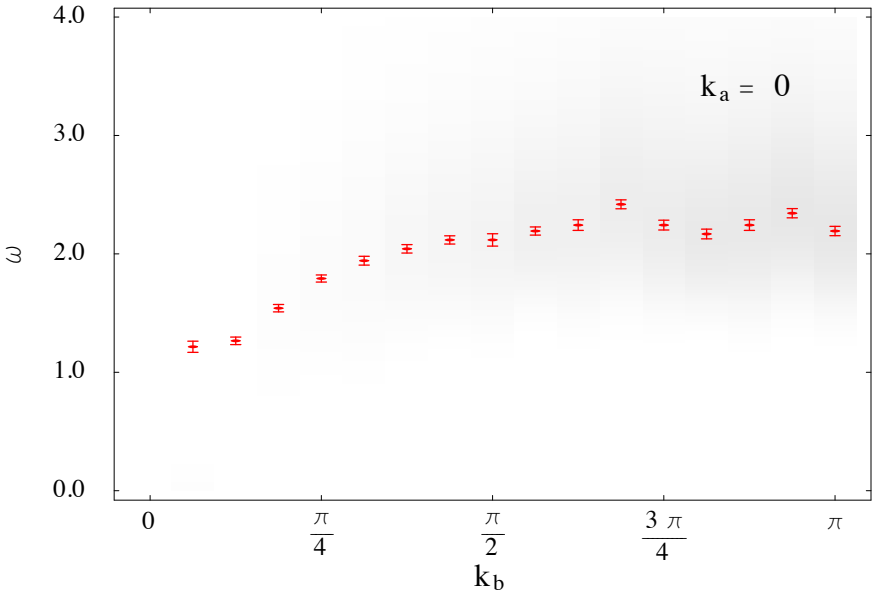

Fig. 5.16: Charge susceptibility $\chi_S(\mathbf{k},\omega)$ of the quarter-filled 32×2 ladder system in the disordered phase at $V = 1.0$ along the ladder with $k_a = 0$.

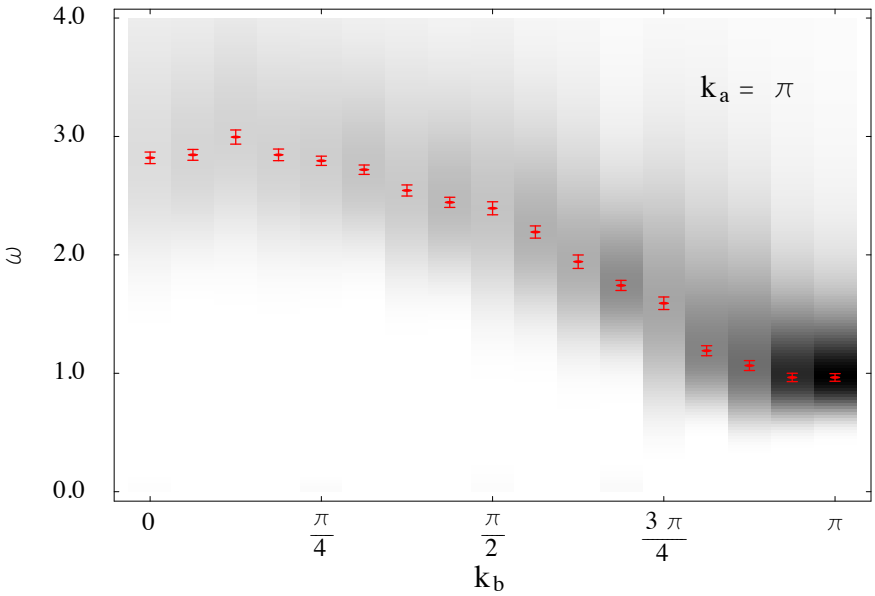

Fig. 5.17: Charge susceptibility $\chi_S(\mathbf{k},\omega)$ of the quarter-filled 32×2 ladder system in the disordered phase at $V = 1.0$ with $k_a = \pi$).

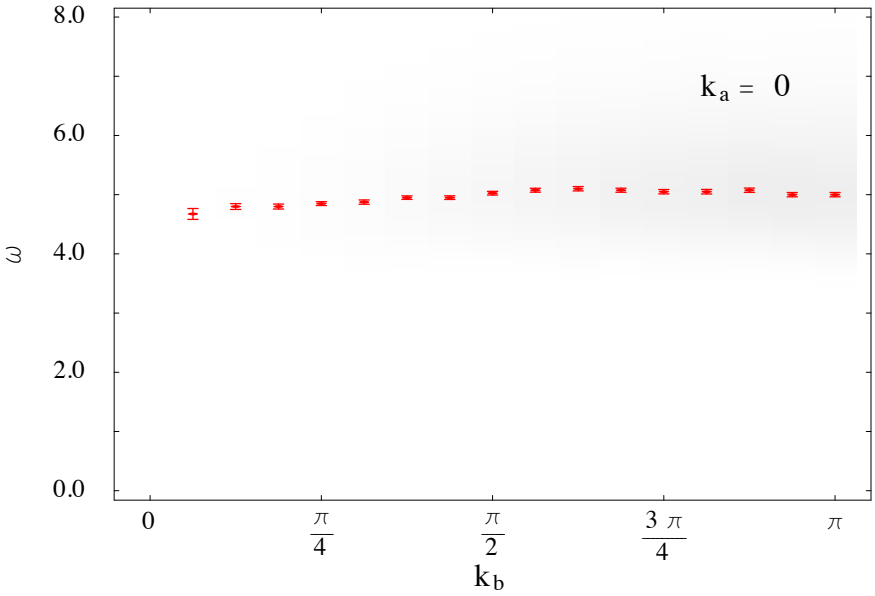

Fig. 5.18: Charge susceptibility $\chi_S(\mathbf{k}, \omega)$ of the quarter-filled 32×2 ladder system in the charge-ordered phase at $V = 1.0$ along the ladder with $k_a = 0$.

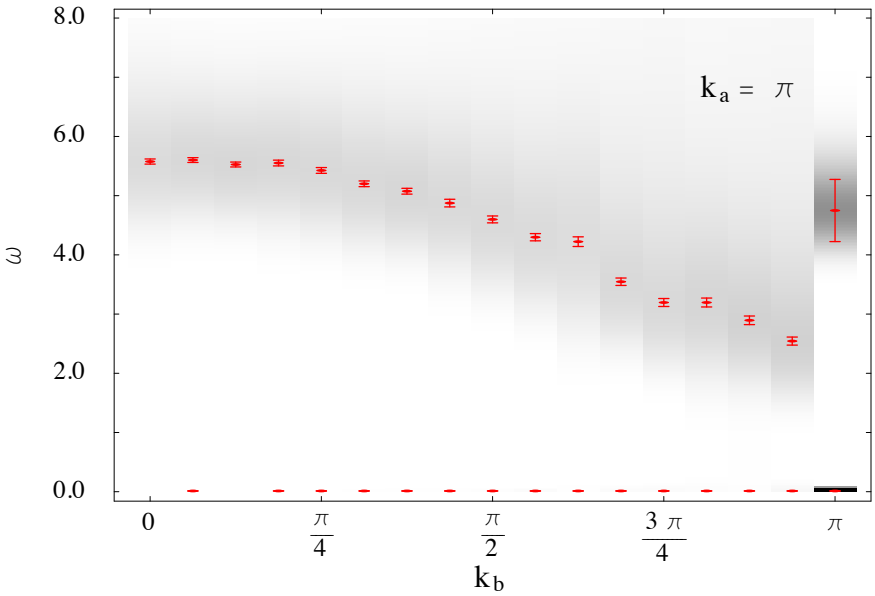

Fig. 5.19: Charge susceptibility $\chi_S(\mathbf{k}, \omega)$ of the quarter-filled 32×2 ladder system in the charge-ordered phase at $V = 1.0$ with $k_a = \pi$).

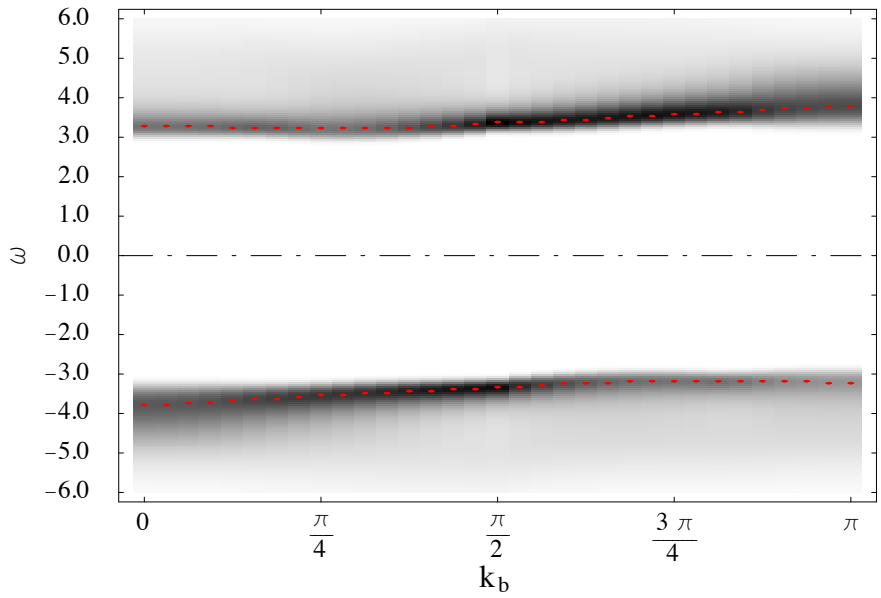

Fig. 5.20: Single-particle spectral function $A(\mathbf{k}, \omega)$ of the half-filled 64-sites Hubbard chain with $t = 0.5$

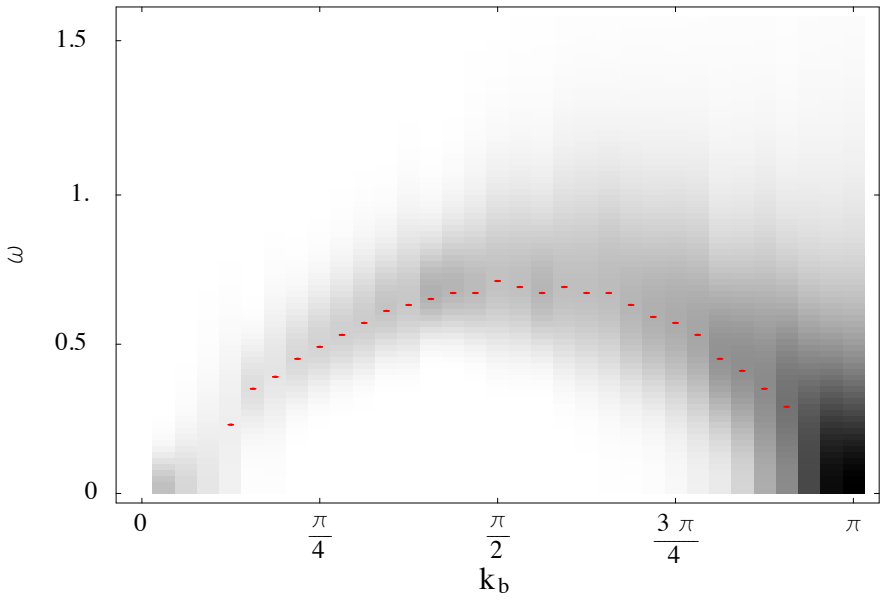

Fig. 5.21: Spin susceptibility $\chi_S(\mathbf{k}, \omega)$ of the half-filled 64-sites Hubbard chain with $t = 1.0$

6 Conclusion

The aim for this thesis was to investigate the charge-order transition of the low dimensional transition metal oxide α'-NaV_2O_5 coupled to the lattice. This challenging problem has been addressed using unbiased numerical techniques.

We gave a detailed introduction to the Determinant Quantum Monte Carlo Method for the extended Hubbard model. Several enhancements for the Monte Carlo sampling in form of global updates and Tempering techniques were described and implemented to improve the convergence of observables. We explained the numerical framework to analyze the Quantum Monte Carlo data and the analytic continuation to the real frequencies axis via the Maximum Entropy method. We also attached importance to the theoretical background necessary for the correct interpretation of the simulation results.

The coupling to the lattice has been realized via Holstein phonons acting on the charge density of the lattice sites which we implemented following the approach for spinless fermions by Hohenadler et al [62]. We extended their idea to the extended Hubbard Holstein model under Lang-Firsov transformation. This work, is to best of our knowledge, the first attempt of the Lang-Firsov transformation with a Quantum Monte Carlo study of a spinfull many-electron Hubbard Holstein model. This basis transformation in principle enables us to sample low correlated phonon configurations at the cost of using complex-kind numerics and the an additional phase factor in the hopping term.

Unfortunately the extension to the many-electron model with spin degrees of freedom brought a severe drawback: the additional phase factor in the hopping term caused a tremendous phase- or minus-sign-problem. We were therefore forced to desist from including the coupling to the lattice.

Nonetheless, we were able to compute unbiased unequal-time correlation function spectra for the extended Hubbard model representing an approximation to the quarter-filled α'-sodium vanadate. Ladder systems of the size 32×2 allowed to minimize finite size effects and to obtain an improved momentum-resolution compared to the small

systems accessible via exact diagonalization techniques. The features of the low energy charge- and spin-excitations as well as of the dispersion of the one particle spectral function were discussed for the disordered and the charge-ordered regime. Next to the dynamical spectral functions we also discussed the change of the order parameter and static observables in dependence on the inter-site Coulomb repulsion and temperature. correlations of the inter-site Coulomb repulsion

Follow-ups

A

A.1 Imaginary time discretization

The Suzuki-Trotter decomposition in detail

The decomposition used in Sec. A.1 is presented for a sum of two non-commuting operators. If the commutator of two operators A and B vanishes, we can simply decompose into the exact product

$$\mathrm{e}^{(A+B)} = \mathrm{e}^{A}\,\mathrm{e}^{B}, \qquad \text{for } [A,B]=0\,. \tag{A.1}$$

Since the kinetic and potential term in the Hamiltonian do *not* commute, we introduce the error R of the decomposition writing

$$\mathrm{e}^{-\beta(A+B)} = \mathrm{e}^{-\beta A}\,\mathrm{e}^{-\beta B} + R\,. \tag{A.2}$$

Expanding both sides in Taylor series for the first three terms yields

$$\mathrm{e}^{-\beta\,(A+B)} = 1-\beta\,(A+B)+\frac{\beta^2}{2}(A^2+B^2+2AB+[B,A])+\mathcal{O}(\beta^3) \tag{A.3}$$

$$\begin{aligned}\mathrm{e}^{-\beta A}\,\mathrm{e}^{-\beta B} &= (1-\beta A+\frac{\beta^2}{2}A^2)\cdot(1-\beta B+\frac{\beta^2}{2}B^2)\\ &= (1-\beta\,(A+B)+\frac{\beta^2}{2}(A^2+B^2+2AB)+\mathcal{O}(\beta^3)\end{aligned} \tag{A.4}$$

for left-hand side and right-hand side, respectively. Comparing these equations the error can be estimated with $\mathcal{O}(\beta^3)$. It is the product of the two operators A and B times $\beta^2/2$. Let t_A and t_B denote the order of magnitude of the operators the error can be written as

$$R \approx \frac{\beta^2}{2}\,\mathcal{O}(t_A\,t_B)\,. \tag{A.5}$$

In case of the Hubbard Hamiltonian t_A and t_B correspond to t and U. As shown by Fye [155], the expected error is proportional to $(\Delta\tau)^2$ – when using the lowest order Trotter decomposition – guaranteed under the condition that the relevant operators are simultaneously real representable (Hermitian). In order to reduce this problem an improved form is given by a symmetric decomposition

$$\mathrm{e}^{-\beta\,(A+B)} = \mathrm{e}^{-\frac{\beta}{2}A}\,\mathrm{e}^{-\beta B}\,\mathrm{e}^{-\frac{\beta}{2}A} + \frac{\beta^3}{24}\,\mathcal{O}(t_A\,t_B\,\max(t_a,t_b))\;. \tag{A.6}$$

Note that for the Hamiltonian used in this paper the asymmetric decomposition in combination with the complex phase is to be favored as shown in [156]. There exists a variety of other methods using decompositions of higher order [157] – unfortunately, they are numerical more expensive.

Whereas the product $\Delta\tau \cdot L$ defines the inverse temperature of the simulation the right choice of $\Delta\tau$ and L depends on the observables one is interested in. In general the discretization of the inverse temperature changes the physics – hence the length of time-steps should be set to values $\Delta\tau < 0.1$ for reasonable results.

Discrete time extrapolation for large systems

We follow [69] to justify the argument to use $\Delta\tau \to 0$ extrapolation results in order to obtain statements for larger systems. Let us assume the leading errors in $\Delta\tau$ are given with increasing order by $\Delta\tau^{a_1}, \Delta\tau^{a_2}, \ldots$ and the finite size errors respectively by $N^{-b_1}, N^{-b_2}, \ldots$. The expectation value ϕ of an operator for a given $\Delta\tau$ and system size N is

$$\begin{aligned}\phi(\Delta\tau, N) = \phi(0,\infty) + c_{10}\Delta\tau^{a_1} + c_{01}N^{-b_1} + c_{20}\Delta\tau^{a_2} + c_{02}N^{-b_2} \\ + c_{11}\Delta\tau^{a_1}N^{b_1} + \text{higher-order terms}\;,\end{aligned} \tag{A.7}$$

where the c_{ij} are constant. Under the condition that the fractional errors due to finite $\Delta\tau$ and N are significantly less than unity, we can accurately extrapolate to $\Delta\tau = 0$ for a system of N_1 sites. Furthermore, with this assumption we know $\phi(\Delta\tau, N_1)$, $\phi(0, N_1)$ and $\phi(\Delta\tau, N_2)$ for the larger system with N_2 sites ($N_1 < N_2$). Therefore we can obtain $\phi(0, N_2)$ safely via

$$\begin{aligned}\phi(0, N_2) = \phi(0, N_1) + [\phi(\Delta\tau, N_2) - \phi(\Delta\tau, N_1)] \\ + \mathcal{O}(\Delta\tau^{a_1}) + \text{higher-order terms}\;.\end{aligned} \tag{A.8}$$

In QMC simulations one usually has an finite Trotter error $\Delta\tau^{a_1} = \Delta\tau^2$. As described, one can use the knowledge of the $\phi(\Delta\tau = 0, N_1)$ behavior to extrapolate to systems of larger size $\phi(\Delta\tau = 0, N_2)$ at high accuracy.

Continuous-time algorithms

Since we use the Suzuki-Trotter decomposition and discretize the imaginary time axis a scaling of $\Delta\tau \to 0$ is necessary to get rid of the Trotter-error. The scaling demands several runs with different values for $\Delta\tau$. This time-consuming practice could be overcome if we could simulate in continous imaginary time. A continuous-time DQMC-method has been introduced by Rombouts and others [111] based on the decomposition of the Boltzmann-factor into a series in the powers of the interaction V

$$\begin{aligned} \mathrm{e}^{-\beta(H_0+V)} &= \mathrm{e}^{-\beta H_0} + \sum_{m=1}^{\infty} (-\beta)^m \int_0^{\beta} dt_m \dots dt_1 \\ &\quad \mathrm{e}^{-t_1 H_0} V \mathrm{e}^{-(t_2-t_1)H_0} V \dots \mathrm{e}^{-(t_m-t_{m1})H_0} V \mathrm{e}^{-(\beta-t_m)H_0} V \,. \end{aligned} \tag{A.9}$$

By extending the V-term $\mathrm{e}^{-\beta(H_0+V)} \to \mathrm{e}^{-\beta H_0+(\mu-\beta V)}$ the Hamiltonian changes only by the constant factor $-\mu/\beta$ but enables us to write

$$\begin{aligned} \mathrm{e}^{-\beta H_0+(\mu-\beta V)} &= \mathrm{e}^{-\beta H_0} + \left[\sum_{m=1}^{\infty} \mu^m \int_0^1 dt_m \dots \int_0^{t_2} dt_m \right. \\ &\quad \left. \prod_{i=1}^{m} \left(1 - \frac{\beta}{\mu} \mathrm{e}^{t_i \beta H_0} V \mathrm{e}^{t_i \beta H_0} \right) \right] \mathrm{e}^{-\beta H_0} \,. \end{aligned} \tag{A.10}$$

The integral over the factor $m \in [0, \infty)$ and all sets of intervals $0 \le t_1 \le \dots \le t_m \le 1$ is done via MC-sampling, which is done similarly to the DetQMC via decoupling of the interaction via HS-transformation. Note that in continous time one has to integrate over a large number of Poisson distributed time steps $\Delta\tau$ of varying length.

For the pure Hubbard-model the discretization-free code is approximately as fast as the code with the common ST-decomposition for the single time-step value $\Delta\tau \sim 0.05$. Fast updates are possible like in the conventional DetQMC. Both algorithms scale similarly with increasing systemsize and decreasing temperature. The different decomposition of the Hamiltonian leads to a different sign-problem behavior.

Recently, Rubtsov et al proposed a continuous time method, which is based on an expansion into perturbation series without the need for auxiliary fields [112]. This approach is especially favorable for long-range interactions and interactions non-local in time. The convergence of the series expansion relies on the finite Hilbert-space of fermionic systems.

A.2 Fermionic sundry

Commutator relations

The anti-commutator relations for fermionic creators $c^\dagger_{i\sigma}$ and annihilators $c_{i\sigma}$ on site i with spin σ are given by

$$\{c_{i\sigma}, c_{j\sigma'}\} = 0 \,, \tag{A.11}$$
$$\{c^\dagger_{i\sigma}, c^\dagger_{j\sigma'}\} = 0 \,, \tag{A.12}$$
$$\{c_{i\sigma}, c^\dagger_{j\sigma'}\} = \delta_{ij}\delta_{\sigma\sigma'} \,. \tag{A.13}$$

Spin operators

The spin operator at site i is given by

$$\sigma_i = (\sigma_x, \sigma_y, \sigma_z) = \left(\begin{pmatrix} 0 & 1 \\ 1 & 0 \end{pmatrix}, \begin{pmatrix} 0 & -i \\ i & 0 \end{pmatrix}, \begin{pmatrix} 1 & 0 \\ 0 & -1 \end{pmatrix} \right) \,, \tag{A.14}$$

where σ_x, σ_y and σ_z are the Pauli matrices so that the fermionic operators can be written as

$$\sigma_{+,i} = \sigma_{x,i} + \mathrm{i}\,\sigma_{y,i} = c^\dagger_{i\uparrow} c_{i\downarrow} \,, \tag{A.15}$$
$$\sigma_{-,i} = \sigma_{x,i} - \mathrm{i}\,\sigma_{y,i} = c^\dagger_{i\downarrow} c_{i\uparrow} \,, \tag{A.16}$$
$$\sigma_{z,i} = \frac{1}{2}\left(c^\dagger_{i\uparrow} c_{i\uparrow} - c^\dagger_{i\downarrow} c_{i\downarrow} \right) = \frac{1}{2}\left(n_{i\uparrow} - n_{i\downarrow} \right) \,. \tag{A.17}$$

Grand canonical trace of fermionic degrees of freedom

We show that the trace over fermionic degrees of freedom can be expressed in form of a determinant. A given Hamiltonian bilinear in its fermion operators can be straightforwardly diagonalized [69, 74, 72] to

$$H = \sum_\alpha a_\alpha \, c^\dagger_\alpha c_\alpha \,, \tag{A.18}$$

with the relations

$$c_\alpha = \sum_i \langle \alpha | i \rangle \, c_i \qquad \text{and} \qquad c^\dagger_\alpha = \sum_i \langle i | \alpha \rangle \, c^\dagger_i \,, \tag{A.19}$$

where the operators c_α result from a unitary transformation to the basis of N-particle states $\big|\alpha\big\rangle$ where H is diagonal. Given the diagonal form, the trace over the fermions can be written as a determinant

$$\begin{aligned}\mathrm{tr}\ \mathrm{e}^{-H} &= \mathrm{tr}\ \mathrm{e}^{-\sum_\alpha a_\alpha c_\alpha^\dagger c_\alpha} \\ &= \mathrm{tr}\ \prod_\alpha \mathrm{e}^{-a_\alpha c_\alpha^\dagger c_\alpha} = \prod_\alpha \sum_{n_\alpha=0,1} \mathrm{e}^{-a_\alpha n_\alpha} \\ &= \prod_\alpha (1+\mathrm{e}^{-a_\alpha})\ . \end{aligned} \tag{A.20}$$

We see that the evolution of the N-particle state is the superposition of the propagation of each particle independently. This holds for any linear superposition of the eigenstates of H and any product of matrices, choosing the basis where they can be represented in bilinear (orthogonal) form. Thus we can write

$$\begin{aligned}\mathrm{tr}\ \mathrm{e}^{-H} &= \mathrm{tr}\ \mathrm{e}^{-\sum_{ij} c_i^\dagger A_{ij} c_j}\ \mathrm{e}^{-\sum_{ij} c_i^\dagger B_{ij} c_j} \\ &= \mathrm{tr}\ \mathrm{e}^{-\sum_\nu \gamma_\nu n_\nu} \\ &= \prod_\nu \sum_{n_\nu=0,1} \mathrm{e}^{-\gamma_\nu c_\nu^\dagger c_\nu} \\ &= \prod_\nu \left(1+\mathrm{e}^{-\gamma_\nu}\right) \\ &= \det\left(\mathbf{1}+\mathrm{e}^{-\mathbf{A}}\mathrm{e}^{-\mathbf{B}}\right)\ . \end{aligned} \tag{A.21}$$

A.3 Hubbard-Stratonovich transformation mutations

There exist various HS-transformations and approximations, developed to minimize phase space, computation time and with the intention to reduce the influence of the fermionic sign problem. Here, we present examples for specific interaction terms with products of different orders of fermionic operators.

Orbital degeneracy

Following [83] we give a type of HS-transformation useful in the presence of orbital degeneracy. In this case the Hubbard term is written as

$$\begin{aligned}H_\mathrm{U} &= U \sum_i \sum_{\nu\le\nu'} \sum_{\sigma\le\sigma'} (1-\delta_{\nu\nu'}\delta_{\sigma\sigma'})\, n_{i\nu\sigma} n_{\nu'\sigma'} \\ &= \frac{U}{2}\sum_i (n_i - N_\mathrm{orb})^2 + \frac{U}{2}(2N_\mathrm{orb}-1)\sum_i n_i\ , \end{aligned} \tag{A.22}$$

where $\nu = 1, \ldots, N_{\mathrm{orb}}$ is an orbital index and $n_i = \sum_{\nu\sigma} n_{i\nu\sigma}$. The quadratic term can be transformed to

$$\begin{aligned} &\exp\left(-\Delta\tau\frac{U}{2}\left(n_i - N_{\mathrm{orb}}\right)^2\right) \\ &\quad = \frac{1}{4}\sum_{m_i(l)=\pm1}\sum_{s_i(l)=\pm1}\gamma_{m_i}\exp\left(\mathrm{i}\, s_i(l)\eta_{m_i}\sqrt{\Delta\tau U/2}\left(n_i - N_{\mathrm{orb}}\right)\right) + \mathcal{O}(\Delta\tau^4)\,, \end{aligned} \tag{A.23}$$

where $\gamma_m = 1 + \frac{\sqrt{6}}{3}m$, and $\eta_m = \sqrt{2\,\left(3 - \sqrt{6}m\right)}$. Although this is just an approximation, the error of $\mathcal{O}(\Delta\tau^4)$ is much smaller than the one done within the Trotter slicing. Here, we used a transformation with complex weights. This kind of approximation turns out to be useful in the case of a W-term

$$H_{\mathrm{W}} = W\sum_i K_i^2\,, \quad \text{with} \quad K_i = \sum_{\sigma\delta}\left(c^\dagger_{i\sigma}c_{i+\delta,\sigma} + c^\dagger_{i+\delta,\sigma}c_{i\sigma}\right)\,, \tag{A.24}$$

in the context of superconductivity [98].

Long range interaction

For increasing range of an intersite interaction the decoupling into additional auxiliary fields becomes intractable because of the expanding phase space which has to be explored by the simulation. An alternative is to couple the auxiliary fields not only to the local spin or charge density, but also to the bosonic fields of other sites (orbitals). For example, Negele and Orland [114, 82] generalize the HS-transformation by writing

$$\exp\left(\frac{1}{2}\mathbf{n}^T\mathbf{M}\,\mathbf{n}\right) \sim \int d\mathbf{x}\,\exp\left(-\frac{1}{2}\mathbf{x}^T\mathbf{M}^{-1}\mathbf{x} + \mathbf{x}^T\mathbf{n}\right) \tag{A.25}$$

$$\sim \int d\mathbf{y}\,\exp\left(-\frac{1}{2}\mathbf{y}^T\mathbf{M}\,\mathbf{y} + \mathbf{y}^T\mathbf{M}\,\mathbf{n}\right)\,, \tag{A.26}$$

where $\mathbf{n}^T = (n_1, n_2, \ldots)$ is a vector of electron occupation numbers in orbitals $1, 2, \ldots, N$ and the eigenvalues of $\mathbf{M}$ are positive. In Eq. (A.25) the electronic charge $\mathbf{n}$ couples to the local *bosonic* field $\mathbf{x}$, which is coupled to itself via $\mathbf{M}^{-1}$, where $\mathbf{M}^{-1}$ is long ranged but $\mathbf{M}$ is assumed to be short ranged. Thus $\mathbf{M}$ in the second integral Eq. (A.26), with $\mathbf{x} = \mathbf{M}\mathbf{y}$, may provide limited interaction range via electron-boson coupling $\mathbf{y}^T\mathbf{M}\,\mathbf{n}$ and

boson-boson coupling $\mathbf{y}^T\mathbf{M}\,\mathbf{y}$. For a general repulsive interaction $V_{ij} \geq 0$ one may write

$$\exp\left(-\Delta\tau \sum_{<ij>} V_{ij}\, n_i n_j\right) = \exp\left(\Delta\tau V_0 \sum_i n_i^2 - \Delta\tau \sum_{<ij>} V_{ij}\, n_i n_j\right) \times \exp\left(-\Delta\tau V_0 \sum_i n_i^2\right) . \qquad \text{(A.27)}$$

Here, the first exponent can be expressed with Eq. (A.25), or Eq. (A.26) with a bosonic field whose components couple to the local density and to each other. The second term has the form of an on-site repulsion, which may be interpreted as a second intermediate field coupled to the local electronic spin density only.

Inter-site Coulomb repulsion

Gabriel et al [151] rewrite the inter-site Coulomb interaction in the extended Hubbard Hamiltonian. Instead of the standard HS-transformation they write the interaction in terms of density operators instead of spin-density operators to be able to expand them into series. This way the updating time of the auxiliary fields is reduced from the need of four auxiliary fields to a single one per dimension. A severe drawback of this procedure is that a discretization error of $\mathcal{O}(\Delta\tau)$ occurs for observables. Using the relations of the density operators

$$\begin{aligned}
(n_i - n_j)^2 &= n_i^2 + n_j^2 - 2\, n_i n_j \rightarrow n_i n_j = \frac{1}{2}\left(n_i^2 + n_j^2 - (n_i - n_j)^2\right) , & \text{(A.28)}\\
n_i^2 &= (n_{i\uparrow} + n_{i\downarrow})^2 = n_{i\uparrow}^2 + n_{i\downarrow}^2 + 2\, n_{i\uparrow} n_{i\downarrow} = n_i + 2\, n_{i\uparrow} n_{i\downarrow} , & \text{(A.29)}\\
\sum_{<ij>} (n_i^2 + n_j^2) &= n_{\mathrm{nn}} \sum_i n_i^2 , & \text{(A.30)}
\end{aligned}$$

- where n_{nn} stands for the number of nearest neighbors – we write

$$H_{\mathrm{U}} + H_{\mathrm{V}} + H_\mu = \tilde{H}_{\mathrm{U}} + \tilde{H}_{\mathrm{V}} + \tilde{H}_\mu + \text{const.} , \qquad \text{(A.31)}$$

with the interaction terms and the chemical potential in the form

$$\tilde{H}_{\mathrm{U}} = -\frac{U_{\mathrm{eff}}}{2}\sum_i (n_{i\uparrow} - n_{i\downarrow})^2 \,, \tag{A.32}$$

$$\tilde{H}_{\mathrm{V}} = -\frac{V}{2}\sum_{<ij>} (n_i - n_j)^2 \,, \tag{A.33}$$

$$\tilde{H}_{\mu} = -\mu_{\mathrm{eff}}\sum_i n_i \,, \tag{A.34}$$

$$U_{\mathrm{eff}} = U + n_{\mathrm{nn}} V \,, \tag{A.35}$$

$$\mu_{\mathrm{eff}} = \mu - \frac{1}{2}(n_{\mathrm{nn}} V - U) \,, \tag{A.36}$$

by introducing the effective couplings U_{eff} and μ_{eff} containing the shares of additional arising terms of similar form. Applying the discrete Hubbard-Stratonovich transformation we obtain

$$\begin{aligned} \mathrm{e}^{\frac{1}{2}\Delta\tau V (n_i - n_j)^2} &= \frac{1}{2}\sum_{\phi_{ij}=\pm 1} \mathrm{e}^{\lambda\,\phi_{ij}(l)\,(n_i - n_j)} \,, \\ \mathrm{e}^{\frac{1}{2}\Delta\tau V (n_i - n_j)^2} &= 1 + \frac{1}{2}\Delta\tau V (n_i - n_j)^2 + \mathcal{O}(\Delta\tau^2) \,. \end{aligned} \tag{A.37}$$

On the other hand via expanding the inter-site coupling term into series we obtain for the extended Hubbard coupling

$$\begin{aligned} \frac{1}{2}\sum_{\phi_{ij}\pm 1} \mathrm{e}^{\lambda\,\phi_{ij}(l)\,(n_i - n_j)} &= \frac{1}{2}\sum_{\phi_{ij}=\pm 1} \lambda\,\phi_{ij}(l)\,(n_i - n_j) + \lambda^2\,\phi_{ij}^2(l)\,(n_i - n_j)^2 + \mathcal{O}(\Delta\tau^2) \\ &= 1 + \lambda^2 (n_i - n_j)^2 + \mathcal{O}(\Delta\tau^2) \\ &= 1 + \frac{1}{2}\Delta\tau V (n_i - n_j)^2 + \mathcal{O}(\Delta\tau^2) \,. \end{aligned} \tag{A.38}$$

The on-site Hubbard coupling is treated as usual, where the number of Ising spins in the extended Hubbard coupling has been reduced from 4 per site and dimension to a single one per site and dimension. The total computation time (including the measurements) is only reduced by a factor ≈ 0.85 due to the vanishing computational effort updating the auxiliary fields in contrast to the matrix-matrix products. In the special case of the used parameter set the extended Hubbard coupling plays the leading role in the system.

Spin-charge separation

In one-dimensional interacting fermion systems the limited number of nearest neighbors allows spin- (magnon) and charge- (exciton) excitations to spread separately in the

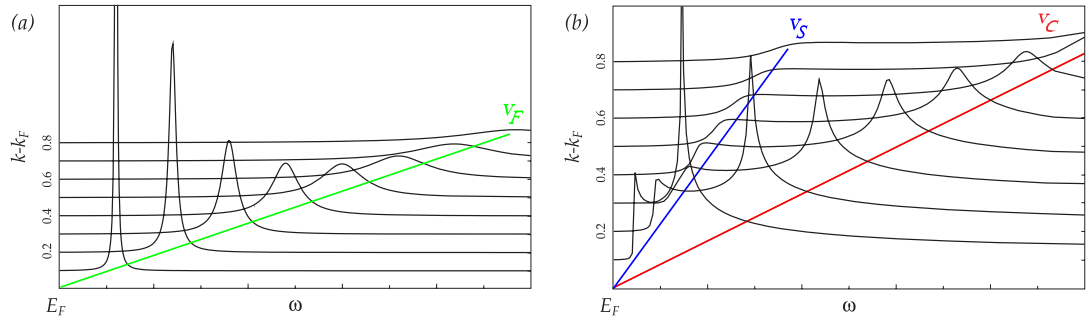

Fig. A.1: Particle excitations near the Fermi-edge in (a) a Fermi liquid for dimension $D = 2, 3$ with quasi-particle-weight $0 < Z < 1$ (b) a Luttinger liquid in one dimension with vanishing quasi-particle-weight $Z \to 0$; v_F, v_s, v_c denote the dispersion Fermi-velocity, spin- and charge-velocity, respectively.

system. This means that bands in the one particle Green's function split up indicating two different propagation velocities. In higher dimensional systems the presence of the field of the surrounding sites makes ferromatgnetic alignment very unlikely and spin and charge excitations are confined to move in conjunction.

The occurance of spin-charge separation is evident in the one-dimensional Hubbard model [158], as well as predicted for sodium vanadate ladder via spin-pseudospin model by Ohta and others [159] and indicated by the CPT-spectra of the one-particle Green's function by Aichhorn and coworkers [142]. In the QMC-spectra this effect is not visible due to the finite resolution of the Maximum Entropy process. Zacher and others overcome this problem as they directly fit to exponentials to the imaginary time displaced Green's function [160]. This method is of use only in the case one can justify to expect only two dominant excitations in the low energy spectrum. A useful indicator for spin-charge separation is a vanishing spin-gap while the charge gap stays finite.

Note, since spin-charge separation is usually brought in common with effective models like the Luttinger-liquid, the system must not nescessarily be described by them. The rising gap for any finite repulsive site coupling pushes away the low energy physics from the Fermi-edge. The primary excitations near the Fermi-edge for the Fermi-liquid and the Luttinger-liquid are sketched in Fig. A.1. In the Luttinger-liquid (dimensions $D < 2$ only) no stable quasi-particles exist. The Fermi-liquid instead (as a model for quasi free electrons) shows quasiparticle excitations with diverging lifetime. Both types have the linear dispersion relations in common. For gapped systems these dispersions are generally quadratic and the system can neither be described by Luttinger- nor Fermi-liquid-theory.

A.4 Spectral functions in experiments

In this section we want to give a brief discussion of the physical ideas of the experimental setup used to obtain spectral functions to be found in this work. Actual literature on this topic can be found in Ref. [161].

One particle Green's function

The spectrum A is the Fourier-transform of the one-particle Green's function G

$$A(\mathbf{k},\omega) = \lim_{\eta\to 0} \frac{1}{\pi} \operatorname{Im} G(\mathbf{k},\omega+\mathrm{i}\eta) \ , \tag{A.39}$$

$$G(\mathbf{r},t) = \sum_{\sigma} -\mathrm{i}\,\Theta\big\langle\{c_\sigma(\mathbf{r},t), c_\sigma^\dagger(0,0)\}\big\rangle \ . \tag{A.40}$$

It reflects the behavior of single electron (hole) excitations. Based on the photo-electric effect (discovered by Hertz, 1887) in angle-resolved photo-emission spectroscopy (ARPES) single-frequency light (e.g. in the UV-range) is sent onto a thin specimen of the material of interest and bombards out electrons. The incident phonons cause emission of electrons which are then detected in with respect to their intensity, momentum and kinetic energy ω. These information allow the direct relation to the properties of the electron in the specimen by exploiting the conservation law for energy

$$\hbar\omega = E_{\mathrm{kin}} + \phi + |E_{\mathrm{B}}| \ , \tag{A.41}$$

where the photon energy must equal the sum of kinetic energy E_{kin}, binding energy E_{B}, and work function. The latter is a specific property of the material and gives the minimum energy necessary to emit a single electron ($\hbar\omega = \phi$). This equation is valid under the assumption that the contribution of photon momenta are negligible. Similarly, the momenta of the electrons in the material are obtained from the conservation law of momentum with the measured angle the electron leaving the specimen. The measured intensity as a function of energy and momentum can be related to the electron Green's function via the so-called sudden approximation[1] so that $I(\mathbf{k},\omega) \propto A(\mathbf{k},\omega)$. Peaks in the spectrum provide information about the nature and lifetime of quasi-particle states up to a resolution of ≈ 2 meV and are broadened due to scattering processes in the specimen.

[1] In the sudden approximation for the final state negigible interaction between the photoelectron and the remaining $N-1$ electron system is assumed.

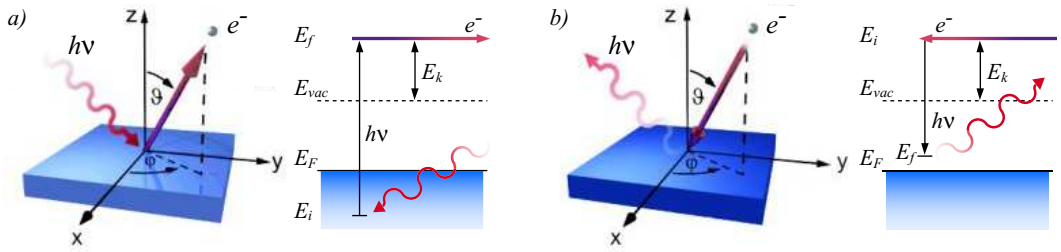

Fig. A.2: Schematic functionality of a) angle-resolved photo-emission spectroscopy (ARPES) b) angle-resolved inverse photo-emission spectroscopy (ARIPES) measurements which are associated with the spectrum of the one particle Green's function.

Charge-charge correlations

Charge density excitations

$$\chi_{\mathrm{CC}}(\mathbf{k},\omega) = \mathrm{FT}\left(C(\mathbf{r},t)\right) = \mathrm{FT}\big\langle n(\mathbf{r},t), n(0,0)\big\rangle - \big\langle n\big\rangle^2 \,, \tag{A.42}$$

are measured by electron energy loss spectroscopy (EELS). A collimated beam of monochromatic, high-energetic (170keV) electrons is shot at a thin specimen. By measuring the angle, intensity and energy of the penetrating electrons the energy-loss and their momenta are obtained. The scattering intensity is normalized via the volume-plasmon leading to the loss-function $L(\mathbf{k}, w)$ which is related to $C(\mathbf{k},\omega)$.

Spin-spin correlations

Similarly to the other two methods, spin-spin excitations

$$\chi_{\mathrm{SS}}(k,\omega) = \mathrm{FT}(S(\mathbf{r},t)) = \frac{1}{2\pi}\int_{-\infty}^{+\infty} dt \sum_k \mathrm{e}^{\mathrm{i}(\mathbf{k}r-\omega t}S(\mathbf{r},t) \,, \tag{A.43}$$

$$\text{with} \qquad S(\mathbf{r},t) = \big\langle S(\mathbf{r},t), S(0,0)\big\rangle \,,$$

are acquired by measuring the cross-section of scattered neutrons which is related via Fourier-transformation to $\big\langle S(t)S(0)\big\rangle$. A formal derivation of scattering polarized neutrons by a lattice of spins, showing the connection to the two-point correlation function is given in the appendix of Binney and others [162]. The neutrons, heavy compared to electrons and *equipped* with spin 1/2, interact with the atomic moments of the material revealing their magnetic properties. The wavelength of the impacting neutrons has to be comparable for the inter-atomic spacings of the material of interest.

Bibliography

[1] J. H. de Boer and E. J. W. Verwey. *Proc. R. Phys. Soc. London*, A 49:59, 1937.

[2] N. F. Mott and R. Peierls. *Proc. R. Phys. Soc. London*, A 49:72, 1937.

[3] E. J. W. Verwey and P. W. Haayman. *Physica*, 8:979, 1941.

[4] P. Lemmens, G. Güntherodt, and C. Gros. Magnetic light scattering in low-dimensional quantum spin systems. *Phys. Rep.*, 375:1, 2002.

[5] M. Isobe and Y. Ueda. Magnetic Susceptibility of Quasi-One-Dimensional Compound α'-NaV_2O_5. *J. Phys. Soc. Jpn.*, 65(5):1178, 1996.

[6] M. Köppen, D. Pankert, and R. Hauptmann. Interference of a first-order transition with the formation of a spin-Peierls state in α-NaV_2O_5. *Europhys. Lett.*, 57(14):8466, 1998.

[7] Y. Fagot-Revurat, M. Mehring, and R. K. Kremer. Charge-Order driven Spin-Peierls Transition in α'-NaV_2O_5. *Phys. Rev. Lett.*, 84(18):4176, 2000.

[8] A. Bernert, P. Thalmeier, and P. Fulde. Microscopic model for the structural transition and spin gap formation in α-NaV_2O_5. *Phys. Rev. B*, 66(16):165108, 2002.

[9] P. Horsch and F. Mack. A new view of the electronic structure of the spin-Peierls compund α'-NaV_2O_5. *Eur. Phys. J. B*, 5:367, 1998.

[10] J. Riera and D. Poilblanc. Coexistence of charge-density wave and spin-Peierls orders in quarter-filled quasi-one-dimensional correlated electron systems. *Phys. Rev. B*, 59:2667, 1999.

[11] A. Carpy and J. Galy. *C. R. Acad. Sci. Paris C*, 262:1055, 1966.

[12] A. Carpy and J. Galy. Affinement de la Structure Cristalline du Bronze NaV_2O_5 α'. *Acta Cryst. B*, 31:1481, 1975.

[13] T. Ohama, H. Yasuoka, and M. Isobe. Mixed valency and charge ordering in α'-NaV_2O_5. *Phys. Rev. B*, 59(5):3299, 1999.

[14] H. G. v. Schnering, Y. Grin, and M. Kaupp. *Z. f. Kristallogr.-New Cryst. Struct.*

[15] J. Riera, D. Poilblanc, and E. Dagotto. Photoemission, inverse photoemission and superconducting correlations in Hubbard and t-J ladders: role of the anisotropy between legs and rungs. *Eur. Phys. J. B*, 7:53, 1999.

[16] H. Smolinski, C. Gros, and W. Weber. α'-NaV_2O_5 as a Quarter-Filled Ladder Compund. *Phys. Rev. Lett.*, 80(23):5164, 1998.

[17] S. van Smaalen and J. Lüdecke. The valence states of vanadium in the low-temperature superstructure of NaV_2O_5. *Eur. Phys. Lett.*, 49(2):250, 2000.

[18] J. L. de Boer, A. Meetsma, J. Baas, and T. T. M. Palstra. Spin-Singlet Clusters in the Ladder Compound NaV_2O_5. *Phys. Rev. Lett.*, 84(17):3962, 1999.

[19] J. Lüdecke, A. Jobst, and S. van Smaalen. Acentric Low-Temperature Superstructure of NaV_2O_5. *Phys. Rev. Lett.*, 82(18):3633, 1999.

[20] S. van Smaalen, P. Daniels, and L. Palatinus. Orthorhombic versus monoclinic symmetry of the charge-ordered state of NaV_2O_5. *cond-mat/0108067*, 2001.

[21] K. Ohwada, Y. Fujii, N. Takesue, M. Isobe, and Y. Ueda. Devil's Staircase-Type Phase Transition in NaV_2O_5 under High Pressure. *Phys. Rev. Lett.*, 87:86402, 2001.

[22] N. M. Bogoliubov and V. E. Korepin. The Role of quasi-one-dimensional Structures in High-T_c Superconductivity. *J. Mod. Phys. B*, 3(3):427, 1988.

[23] E. Dagotto and T. M. Rice. Surprises on the Way from One- to Two-Dimensional Quantum Magnets: The Ladder Materials. *Science*, 271:618, 1996.

[24] D. Poilblanc, E. Orignac, S.R. White, and S. Capponi. Resonant magnetic mode in superconducting 2-leg ladders. *cond-mat/0402011*, 2004.

[25] M. Imada, A. Fujimori, and Y. Tokura. Metal-insulator transitions. *RMP*, 70:1039, 1998.

[26] J. Spitaler, E. Ya. Sherman, C. Ambrosch-Draxl, and H. G. Evertz. Proceedings of the summer school: DFT Beyond the Ground State. *Physica Scripta*, T109(159), 2004.

[27] J. Hubbard. Electron correlations in narrow energy bands I, II, II. *Proc. R. Phys. Soc. London*, A 276:238, A 277:237, A 281:401, 1963.

[28] E. H. Lieb and F. Y. Wu. Absence of Mott Transition in an Exact Solution of the Short-Range, One-Band Model in One Dimension. *Phys. Rev. Lett.*, 20(25):1445, 1968.

[29] M. Karbach and G. Müller. Introduction to the Bethe Ansatz I, II, III. *cond-mat/9809162, cond-mat/9809163, cond-mat/0008018*, 1998, 2000.

[30] F. Gebhard. *The Mott Metal-Insulator Transition*. Springer, Berlin Heidelberg, 1997.

[31] A. Auerbach. *Interacting Electrons and Quantum Magnetism*. Springer, New York, 1994.

[32] S. Watanabe and M. Imada. Thermodynamic Relations in Correlated Systems. *cond-mat/0412602*, 2004.

[33] J. E. Hirsch. Charge-Density-Wave to Spin-Density-Wave Transition in the Extended Hubbard model. *Phys. Rev. Lett.*, 53(24):2327, 1984.

[34] M. G. Zacher. Elektronische Anregungen des eindimensionalen Hubbard-Modells mit längerreichweitigen Wechselwirkungen. Diploma thesis, Bayerische Julius-Maximiliam-Universität Würzburg, 1996.

[35] M. Nakamura. Mechanism of CDW-SDW Transition in One Dimension. *J. Phys. Soc. Jpn.*, 68(10):3121, 1999.

[36] M. Nakamura. Tricritical behavior in the extended Hubbard chains. *Phys. Rev. B*, 61(24):16377, 2000.

[37] A. W. Sandvik, L. Balents, and D. K. Campbell. Ground State Phases of the Half-Filled One-Dimensional Extended Hubbard Model. *Phys. Rev. Lett.*, 92(23):236401, 2004.

[38] M. Vojta, A. Hübsch, and R. M. Noack. Phase diagram of the quarter-filled extended Hubbard model on a two-leg ladder. *Phys. Rev. B*, 63:045105, 2001.

[39] R. T. Clay and S. Mazumdar. Rung-singlet charge-ordering in α'-NaV_2O_5. *cond-mat/0305479*, 2003.

[40] T. Holstein. Studies of polaron motion I, II. *Ann. Phys. (N.Y.) 8:325, 8:343*, 1959.

[41] I. G. Lang and Yu. A. Firsov. Kinetic theory of semiconductors with low mobility. *Sov. Phys. JETP*, 16(5):1301, 1963.

[42] J. E. Hirsch and E. Fradkin. Phase diagram of one-dimensional electron-phonon systems. II. The molecular-crystal model. *Phys. Rev. B*, 27(7):4302, 1983.

[43] M. Hohenadler. *Numerical investigation of strongly correlated electron-phonon models*. PhD thesis, Technische Universität Graz, 2004.

[44] H. De Raedt and A. Lagendijk. Computer Simulation Study of Bipolaron Formation. *Z. Phys. B - Condensed Matter*, 65:43, 1986.

[45] J. Bonca and S. A. Trugman. Bipolarons in the extended Holstein Hubbard model. *Phys. Rev. B*, 64(9):094507, 2001.

[46] M. Acquarone, M. Cuoco, C. Noce, and A. Romano. Variational study of the extended Hubbard-Holstein model on clusters of variable site spacing. *Phys. Rev. B*, 64(3):035110, 2001.

[47] A. S. Alexandrov and N. F. Mott. *Polarons and Bipolarons*. World Scientific, 1996.

[48] E. Fradkin. *Field Theories of Condensed Matter Systems*. Frontiers in Physics, Addison-Wesley, 1998.

[49] B. L. Cerchiai and P. Schupp. Symmetries of an extended Hubbard Model. *cond-mat/9605121v1*, 1996.

[50] H. Tasaki. The Hubbard Model: Introduction and Selected Rigorous Results. *cond-mat/9512169*, 1995.

[51] E. Lieb. The Hubbard Model: Some Rigorous Results and Open Problems. *cond-mat/9311033*, 1993.

[52] D. K. Ghosh. Nonexistence of Magnetic Ordering in the One- and Two-Dimensional Hubbard Model. *Phys. Rev. Lett.*, 27(23):1584, 1971.

[53] N. D. Mermin and H. Wagner. Absence of ferromagnetism or antiferromagnetism in one-or twodimensional isotropic Heisenberg models. *Phys. Rev. Lett.*, 17(22):1133, 1966.

[54] E. H. Lieb. Two theorems on the Hubbard model. *Phys. Rev. Lett.*, 62(10):1201, 1989.

[55] T. Koma and H. Tasaki. Decay of superconducting and magnetic correlations in one and two dimensional Hubbard models. *Phys. Rev. Lett.*, 68(21):3248, 1992.

[56] T. Koma and H. Tasaki. Symmetry breaking and long range order. *Commun. Math. Phys.*, 158:191, 1993.

[57] M. Fischer, P. Lemmens, G. Els, G. Güntherodt, E. Ya. Sherman E. Morre, C. Geibel, and F. Steglich. Spin-gap behavior and charge ordering in α'-NaV_2O_5 probed by light scattering. *Phys. Rev. B*, 60(10):7284, 1999.

[58] M. V. Mostovoy and D. I. Khomskii. Charge ordering and opening of spin gap in NaV_2O_5. *Sol. St. Comm.*, 113:159, 1999.

[59] E. V. L. de Mello and J. Ranninger. Dynamical properties of small polarons. *Phys. Rev. B*, 55(22):14872, 1997.

[60] H. Fehske, J. Loos, and G. Wellein. Lattice polaron formation: Effects of non-screened electron-phonon interaction. *Phys. Rev. B*, 61(12):8016, 1999.

[61] J. M. Robin. Spectral properties of the small polaron. *Phys. Rev. B*, 56(21):13634, 1997.

[62] M. Hohenadler, H. G. Evertz, and W. von der Linden. Quantum Monte Carlo and variational approaches to the Holstein model. *Phys. Rev. B*, 69(2):24301, 2004.

[63] M. Hohenadler and W. von der Linden. Temperature- and quantum phonon effects on the Holstein-Hubbard bipolaron. *cond-mat/0409573*, 2004.

[64] M. Hohenadler, M. Aichhorn, and W. von der Linden. Spectral function of the Holstein-Hubbard bipolaron. *cond-mat/0405391*, 2004.

[65] N. Metropolis, A. W. Rosenbluth, M. N. Rosenbluth, A. H. Teller, and E. Teller. Equations of state calculations by fast computing machines. *J. Chem. Phys.*, 21:1087, 1953.

[66] M. Troyer and U. J. Wiese. Computational complexity and fundamental limitations to fermionic quantum Monte Carlo simulations. *cond-mat/0408370*, 1998.

[67] D. P. Landau and K. Binder. *A Guide to Monte Carlo Simulations in Statistical Physics*. Cambridge Univ. Press, 2000.

[68] R. P. Feynman. Atomic Theory of the lambda Transition in Helium. *Phys. Rev.*, 91(6):1291, 1953.

[69] W. von der Linden. A quantum Monte Carlo approach to many-body physics. *Phys. Rep.*, 220:53, 1992.

[70] H. G. Evertz. The Loop Algorithm. *Advances in Physics*, 52:1, 2003.

[71] J. E. Hirsch. Monte Carlo Study of the Two-dimensional Hubbard model. *Phys. Rev. Lett.*, 51(20):1900, 1983.

[72] J. E. Hirsch. Two-dimensional Hubbard model: Numerical simulation study. *Phys. Rev. B*, 31(7):4403, 1985.

[73] S. R. White, D. J. Scalapino, and R. L Sugar. Numerical study of the two-dimensional Hubbard model. *Phys. Rev. B*, 40(1):506, 1989.

[74] R. Blankenbecler, D. J. Scalapino, and R. L Sugar. Monte Carlo calculations of coupled boson-fermion systems. I. *Phys. Rev. D*, 24(8):2278, 1981.

[75] D. J. Scalapino and R. L Sugar. Monte Carlo calculations of coupled boson-fermion systems. II. *Phys. Rev. B*, 24(8):4295, 1981.

[76] Y. Nambu and G. Jona-Lasinio. Dynamical Model of Elementary Particles based on an Analogy with Superconductivity I, II. *Phys. Rev. 122(1):345, 1960, 124(1):246 1961.*

[77] D. J. Gross and A. Neveu. Dynamical symmetry breaking in asymptotically free field theories. *PRD*, 10(10):3235, 1974.

[78] M. Suzuki. *Comm. Math. Phys.*, 51:183, 1976.

[79] M. Suzuki, S. Miyashita, and A. Kuroda. Monte Carlo Simulation of Quantum Spin Systems. I. *Prog. Theor. Phys.*, 58(5):1377, 1977.

[80] H. F. Trotter. On the product of semi-groups of operators. *Proc. Amer. Math. Soc.*, 10:545, 1959.

[81] P. Valasek. *Numerische Simulation von Vielteilchensystemen.* PhD thesis, Bayerische Julius-Maximiliam-Universität Würzburg, 1996.

[82] E. Y. Loh Jr. and J. E. Gubernatis. *Stable Numerical Simulations of Models of Interacting Electrons in Condensed-Matter Physics, in Electronic Phase Transitions.* W. Hanke and Yu. V. Kopaev (Eds.), Elsevier Science Publishers B. V., New York, 1992.

[83] A. Muramatsu. *Quantum Monte Carlo Methods in Physics and Chemistry: Quantum Monte Carlo for Lattice Fermions.* M. P. Nightingale and C. J. Umrigar (Eds.), NATO Science Series Vol. :343-373, Kluwer Academic, Dordrecht, 1999.

[84] H. Endres. *Physik des Hubbard-Modells zwischen einer und zwei Dimensionen.* PhD thesis, Bayerische Julius-Maximiliam-Universität Würzburg, 1996.

[85] P. Valasek. Electron-Phonon Wechselwirkung im Hubbard-Modell: Quantum-Monte-Carlo Untersuchungen. Diploma thesis, Bayerische Julius-Maximiliam-Universität Würzburg, 1993.

[86] R. Preuss. *Dynamik von Hubbard Modellen.* PhD thesis, Bayerische Julius-Maximiliam-Universität Würzburg, 1996.

[87] M. G. Zacher. *From one to two dimensions: Numerical and analytical studies on strongly correlated electron systems.* PhD thesis, Bayerische Julius-Maximilians-Universität Würzburg, 1999.

[88] C. Dahnken. Elektronische Anregungen des Hubbard-Modells mit langreichweitiger Wechselwirkung. Diploma thesis, Bayerische Julius-Maximiliam-Universität Würzburg, 1998.

[89] J. Hubbard. Calculation of Partition Functions. *Phys. Rev.*, 3(2):77, 1959.

[90] J. E. Hirsch. Discrete Hubbard-Stratonovich transformation for fermion lattice models. *Phys. Rev. B*, 28(7):4059, 1983.

[91] J. E. Hirsch. Connection between world-line and determinantal functional-integral formulations of the Hubbard model. *Phys. Rev. B*, 34(5):3216, 1986.

[92] W. Nolting. *Grundkurs Theoretische Physik 7 - Viel-Teilchen-Theorie*. Springer, Berlin Heidelberg, 2002.

[93] A. L. Fetter and J. D. Walecka. *Quantum Theory of Many-Particle Systems*. McGraw-Hill, New York, 1971.

[94] L. Pollet, S. M. A. Rombouts, K. Van Houcke, and K. Heyde. Optimal Monte Carlo updating. *Phys. Rev. E*, 70(5):56705, 2004.

[95] D. Loison, C. L. Qin, K. D. Schotte, and X. F. Jin. Canonical local algorithms for spin systems: heat bath and Hastings methods. *Eur. Phys. J. B*, 41:395, 2004.

[96] W. H. Press, S. A. Teukolsky, W. T. Vetterling, and B. P. Flannery. *Numerical Recipes in C – 2nd edition*. Cambridge Univ. Press, 1999.

[97] D. Eckert. Phononen im Hubbard Modell. Diploma thesis, Bayerische Julius-Maximiliam-Universität Würzburg, 1997.

[98] F. F. Assaad. SU(2)-spin Invariant Auxiliary Field Quantum Monte-Carlo Alorithm for Hubbard models. *cond-mat/9806307*, 1998.

[99] E. Y. Loh Jr, J. E. Gubernatis, and R. T. Scalettar. Sign problem in the numerical simulation of many-electron systems. *Phys. Rev. B*, 41(13):9301, 1990.

[100] R. T. Scalettar, R. M. Noack, and R. R. P. Singh. Ergodicity at Large Couplings with Determinantal Monte Carlo. *Phys. Rev. B*, 44(19):10502, 1991.

[101] K. Hukushima and K. Nemoto. Exchange Monte Carlo Method and Application to Spin Glass Simulations. *J. Phys. Soc. Jpn.*, 65(6):1604, 1995.

[102] E. Marinari and G. Parisi. Simulated Tempering: a New Monte Carlo Scheme. *Eur. Phys. Lett.*, 19(6):451, 1992.

[103] M. Daghofer. Berechnung thermodynamischer Suszeptibilitä mit Exakter Diagonalisierung, 2001.

[104] W. Gropp, E. Lusk, and A. Skjellum. *Using MPI*. MIT Press, Massachusetts, 1999.

[105] A. W. Sandvik. Bond-order-wave phase and quantum phase transitions in the one-dimensional extended Hubbard model. *Phys. Rev. B*, 65(18):155113, 2002.

[106] M. Aichhorn, M. Daghofer, H. G. Evertz, and W. von der Linden. Low temperature Lanczos method for strongly correlated systems. *Phys. Rev. B*, 67(16):161103(R), 2003.

[107] A. W. Sandvik and J. Kurkijärvi. Quantum Monte Carlo simulation method for spin systems. *Phys. Rev. B*, 43(7):5950, 1991.

[108] S. B. Fahy and D. R. Hamann. Positive-projection Monte Carlo simulation: A new variational approach to strongly interacting fermion systems. *Phys. Rev. Lett.*, 65(27):3437, 1990.

[109] S. Zhang, J. Carlson, and J. E. Gubernatis. A Constrained Path Monte Carlo Method for Fermion Ground States. *Phys. Rev. Lett.*, 74(18):3652, 1995.

[110] D. J. Klein and H. M. Pickett. Nodal hypersurfaces and Anderson's random-walk simulation of the Schrödinger equation. *J. Chem. Phys.*, 64(11):4811, 1976.

[111] S. M. A. Rombouts, K. Heyde, and N. Jachowicz. Quantum Monte Carlo Method for Fermions, Free of Discretization Errors. *Phys. Rev. Lett.*, 82(21):4155, 1999.

[112] A. N. Rubtsov, V. V. Savkin, and A. I. Lichtenstein. Continuous Time Quantum Monte Carlo method for fermions. *cond-mat/0411344*, 2004.

[113] G. D. Mahan. *Many-particle physics*. Plenum Press, New York, 1981.

[114] J. W. Negele and H. Orland. *Quantum Many-Particle Physics*. Perseus Books, Massachusetts, 1998.

[115] F. F. Assaad. *Quantum Monte Carlo Methods on Lattices: The Determinantal Approach*. J. Grotendorst and A. Muramatsu (Eds.), NIC Series Vol. 10, Jülich, 2002.

[116] G. Batrouni and R. T. Scalettar. Anomalous decouplings and the fermion sign problem. *Phys. Rev. B*, 42(4):2282, 1990.

[117] G. G. Batrouni and P. de Forcrand. Fermionic sign problem: Decoupling transformation and simulation algorithm. *Phys. Rev. B*, 48(1):589, 1993.

[118] R. W. Floyd. Nondeterministic Algorithms. *Journal ACM*, 14(4):636, 1967.

[119] S. Chandrasekharan and U. J. Wiese. Meron-Cluster Solution of Fermion Sign Problems. *Phys. Rev. Lett.*, 83:3116, 1999.

[120] W. Janke. *Statistical Analysis of Simulations: Data Correlations and Error Estimation*. J. Grotendorst and A. Muramatsu (Eds.), NIC Series Vol. 10, Jülich, 2002.

[121] A. D. Sokal and L. E. Thomas. Exponential convergence to equilibrium for a class of random walk models. *J. Stat. Phys.*, 54:797, 1989.

[122] M. S. Carroll, W. Janke, and S. Kappler. Dynamical Behavior of the Multibondic and Multicanonic Algorithm In The 3D q-State Potts Model. *J. Stat. Phys.*, 90(6):1277, 1998.

[123] R. N. Silver, D. S. Sivia, and J. E. Gubernatis. Maximum-entropy method for analytical continuation of quantum Monte Carlo data. *Phys. Rev. B*, 41(4):2380, 1990.

[124] R. N. Silver, M. Jarrell, and J. E. Gubernatis. Quantum Monte Carlo simulations and maximum entropy: Dynamics from imaginary-time data. *Phys. Rev. B*, 44(12):6011, 1991.

[125] W. von der Linden, R. Preuss, and W. Hanke. Consistent Application of maximum entropy to quantum Monte Carlo data. *J. Phys. Cond. Mat.*, 8:3881, 1996.

[126] A. W. Sandvik. Stochastic method for analytic continuation of quantum Monte Carlo data. *Phys. Rev. B*, 57(17):10287, 1998.

[127] K. S. D. Beach. Identifiying the maximum entropy as a special limit of stochastic analytic continuation. *cond-mat/0403055*, 2004.

[128] R. N. Silver, H. Roeder, A. F. Voter, and J. D. Kress. Kernel Polynomial Approximations for Densities of States and Spectral Functions. *J. Comp. Phys.*, 124(1):115, 1996.

[129] C. Michael. Adjoint sources in the lattice gauge theory. *Nucl. Phys. B*, 259:58, 1984.

[130] M. Lüscher and U. Wolff. How to calculate the elastic scattering matrix in two-dimensional quantum field theories by numerical simulation. *Nucl. Phys. B*, 339:222, 1990.

[131] T. Burch, C. Gattringer, L. Ya. Glozman, R. Kleindl, C. B. Lang, and A. Schäfer. Spatially improved operators for excited hadrons on the lattice. *hep-lat/0405006*, 2004.

[132] J. E. Hirsch and R. M. Fye. Monte Carlo Method for Magnetic Impurities in Metals. *Phys. Rev. Lett.*, 56(23):2521, 1986.

[133] A. Georges, G. Kotliar, W. Krauth, and M. J. Rozenberg. Dynamical mean-field theory of strongly correlated fermion systems and the limit of infinite dimensions. *Rev. Mod. Phys.*, 68(1):34, 1996.

[134] D. R. Neuber, M. Daghofer, and W. von der Linden. Data Analysis of Quantum Monte Carlo Simulations – Proceedings of the MaxEnt04 Workshop, MPI Garching. *Proceedings of the MaxEnt04 conference*, 2004.

[135] M. Vekic and S. R. White. Gap information in the density of states for the Holstein model. *Phys. Rev. B*, 48(10):7643, 1993.

[136] S. R. White. Spectral weight function for the two-dimensional Hubbard model. *Phys. Rev. B*, 44(9):4670, 1991.

[137] A. Brooks Harris and R. V: Lange. Single-Particle Excitations in Narrow Energy Bands. *Phys. Rev.*, 157(2):295, 1967.

[138] T. Koma and H. Tasaki. Symmetry breaking and finite size effects in quantum many-body systems. *J. Stat. Phys.*, 76:745, 1994.

[139] J. L. Cardy. *Scaling and renormalization in statistical physics*. Cambridge Univ. Press, 2002.

[140] M. Vojta, R. E. Hetzel, and R. M. Noack. Charge-order transition in the extended Hubbard model on a two-leg ladder. *Phys. Rev. B*, 60(12):R8417, 1999.

[141] M. Aichhorn, M. Hohenadler, E. Ya. Sherman, J. Spitaler, C. Ambrosch-Draxl, and H. G. Evertz. Charge Ordering in quarter-filled ladder systems coupled to the lattice. *Phys. Rev. B*, 69(24):245108, 2004.

[142] M. Aichhorn, E. Ya. Sherman, and H. G. Evertz. Single-particle spectral function of quarter-filled ladder systems. *cond-mat/0409162*, 2004.

[143] B. Edegger. Charge ordering in α' NaV_2O_5, 2003.

[144] B. Edegger, H. G. Evertz, and R. M. Noack. Charge order induced by electron-lattice interaction in NaV_2O_5. *cond-mat/0505685*, 2005.

[145] M. Vojta. Quantum phase transitions. *cond-mat/0309604*, 2003.

[146] S. Sachdev. *Quantum phase transitions*. Cambridge Univ. Press, 2001.

[147] Y. Lin. *Strongly Disordered Quantum Spin Systems in Low Dimensions: Numerical Study of Spin Chains, Spin Ladders and Two-Dimensional Systems*. J. Grotendorst and A. Muramatsu (Eds.), NIC Series Vol. 12, Jülich, 2002.

[148] S. Chakravarty, B. I. Halperin, and D. R. Nelson. Two-dimensional quantum Heisenberg antiferromagnet at low temperatures. *Phys. Rev. B*, 39(4):2344, 1989.

[149] J. Goldstone. Field Theories With 'Superconductor' Solutions. *Nuovo Cim.*, 19:154, 1961.

[150] J. Goldstone, A. Salam, and S. Weinberg. Broken Symmetries. *Phys. Rev.*, 127(3):965, 1962.

[151] C. Gabriel, E. Sherman, T. C. Lang, M. Aichhorn, and H. G. Evertz. Finite Temperature investigation of quarter-filled ladder systems. *Physica B*, 359:804, 2005.

[152] E. Lieb, T. Schulz, and D. Mattis. *Ann. Phys.*, 16:407, 1961.

[153] J. des Cloizeaux and J. J. Pearson. *Phys. Rev.*, 128:2131, 1962.

[154] A. Damascelli, D. van der Marel, and M. Grüninger. . *Phys. Rev. B*, 61:2535, 2000.

[155] R. M. Fye. New results on Trotter-like approximations. *Phys. Rev. B*, 33(9):6271, 1986.

[156] F. F. Assaad, W. Hanke, and D. J. Scalapino. Temperature derivative of the superfluid density and flux quantization as criteria for superconductivity in two dimensional Hubbard models. *Phys. Rev. B*, 50(17):12835, 1994.

[157] W. von der Linden and M. Hohenadler. *Numerical Many Body Systems*. in prep., in prep.

[158] H. Benthien and F. Gebhard. Spectral Function of the One-Dimensional Hubbard Modell away from Half Filling. *Phys. Rev. Lett.*, 92(25):256401, 2004.

[159] Y. Ohta, T. Nakaegawa, and S. Ejima. Seperated Spin and Charge Excitations and their Coupling in the Spin-Pseudospin Model for Quarter-Filled Ladders. *cond-mat/0309433*, 2003.

[160] M. G. Zacher, E. Arrigoni, W. Hanke, and J. R. Schrieffer. Systematic numerical study of spin-charge separation in one dimension. *Phys. Rev. B*, 57(11):6370, 1998.

[161] T. Mulvey and B. Kazan. *Advances in Imaging and Electron Physics*. Elsevier, 1999.

[162] J. J. Binney, N. J. Dowrick, A. J. Fisher, and M. E. J. Newman. *The Theory of Critical Phenomena - An Introduction to the Renormalization Group.* Oxford Univ. Press, 1995.

Acknowledgments

I would like to gratefully acknowledge the supervision of Prof. Hans Gerd Evertz, who gave me the chance to work on this current and challenging research subject, for his time for numerous questions and motivating discussions.

Special thanks to Franz Michel, Martin Hohenadler and Markus Aichhorn for help and reference data, Danilo Neuber for his MaxEnt-program, my roommates and neighbors Maria Daghofer, Bernhard Edegger and Ingrid Reiweger for bearing my countless questions and of course to all of them for providing fruitful discussions and support. Thanks to the SysAdmins Andreas Hirczy and Christian Pfaffel-Janser for a great computing environment and support. Above all, I thank you and the department for the amiable and fun working atmosphere!

Thanks to Gernot Pfanner, my physical discourse affiliate from school days on.

I am forever indebted to my family, especially my parents, for their confidence and encouragement. I thank you for your love and the opportunity to achieve this aim.

Finally, special thanks to my darling Magdalena – for your love, for supporting me mentally as well as morally and sharing me with physics.

I am grateful to the Fund for Scientific Research (FWF), project No. P15834, for financial support.

Thanks to my good friend caffeine!